UNIVERSITY OF CALIFORNIA
RIVERSIDE

Thermo-fluid Dynamics of Flash Atomizing Sprays and Single Droplet Impacts

A Dissertation submitted in partial satisfaction
of the requirements for the degree of

Doctor of Philosophy

in

Mechanical Engineering

by

Henry H. Vu

March 2010

Dissertation Committee:
Dr. Guillermo Aguilar, chairperson
Dr. Heejung Jung
Dr. Marko Princevac

The Dissertation of Henry H. Vu is approved:

_____

_____

_____
Committee Chairperson

University of California, Riverside

ACKNOWLEDGEMENTS

Much of the enclosed content has been published or submitted for publication in the following media: Proceedings of the Institute of Liquid Atomization and Spray Systems, Proceedings of the International Congress of Liquid Atomization and Spray Systems, International Journal of Heat and Mass Transfer, Proceedings of the ASME-JSME Thermal Engineering Summer Heat Transfer Conference, Journal of Biomechanical Engineering, Atomization and Sprays, Experiments in Fluids.

Financial support for my studies was provided by: UCR College Fellowship Award, OMNIBUS Academic Senate Research Fund, Institute of Liquid Atomization and Spray Systems, Roberta Nichols Graduate Fellowship, Sandia National Labs (contract 2565-009 BEA), and the Chancellor's Dissertation Fellowship.

Most importantly, I would like to thank my advisor, Guillermo Aguilar, for his mentorship over all these years and his faith in my ability. I also must humbly acknowledge the invaluable guidance from my other committee members, Marko Princevac and Heejung Jung and those that I have collaborated with over the years: Walfre Franco, Jie Liu, Octavio García-Valladares, Richard Jepsen, Alex Brown, Feng Sun and Francisco Perez. My work would also have been much more difficult without the assistance of many undergraduate helpers: Kevin Chu, David Han, Will Macias, Joshua Yagoubian, Alex Chaney, Amelia Ramirez-Correa, Brandon Catuara, and Darren Banks. Lastly, I must acknowledge all the wonderful people I've met along the way, for making the journey so much more enriching and worthwhile. Thank you.

DEDICATION

To my family, for their encouragement and moral support.

I hope I have made you proud.

ABSTRACT OF THE DISSERTATION

Thermo-fluid Dynamics of Flash Atomizing Sprays
and Single Droplet Impacts

by

Henry H. Vu

Doctor of Philosophy, Graduate Program in Mechanical Engineering
University of California, Riverside, March 2010
Dr. Guillermo Aguilar, Chairperson

Spray atomization and droplet dynamics are research topics that have existed for many decades. Their prevalence in manufacturing, energy generation and other practical applications is undeniable, though researchers have often overlooked the importance of understanding the physics of atomization or droplet impact characteristics in the ongoing effort to improve efficiency. In this dissertation, I will address the atomization of thermodynamically unstable "flashing" sprays and the splashing mechanisms of single droplets impinging on flat, smooth surfaces. The related heat transfer phenomena for cooling applications are also addressed. These topics are motivated by efforts to improve the thermal protection provided by cryogenic spray cooling in laser dermatological procedures, increasing the throughput of the spray production of nano and micro-scale particulates used as dyes and catalysts, and in modeling of the release and dispersion of flammable or hazardous chemicals through large-scale collisions with storage containers.

Through the use of high-speed video imaging, phase Doppler interferometric measurements and numerical modeling of the two-phase flow taking place within spray nozzles, a detailed picture of the processes involved in flash atomization are attained. Results reveal that flashing fluid jets under low superheats undergo many dynamic processes leading to eventual droplet formation, including the nucleation of vapor bubbles within the nozzle interior and their subsequent expansion and explosion. At high superheats, a stable "flare flashing" regime is attained resulting in very fine atomization. These insights may lead to improved nozzle designs to better control the atomization process.

High-speed imaging of droplet impacts also reveals new insights into the mechanisms of splashing. The surrounding ambient air pressure, fluid viscosity, and fluid-surface affinity are found to profoundly influence the initiation and characteristics of splashing. A new analytical model explaining the mechanisms of crown splashing is developed along with correlations predicting the threshold of splashing.

TABLE OF CONTENTS

List of Figures

List of Tables

CHAPTER 1: Introduction

Sprays and droplets are an important subcategory of multiphase flows, rich in complexity and an integral part of many very important applications. My interest in this area initially began from my prior research in cryogen spray cooling (CSC) for laser dermatological procedures as an undergraduate with my advisor. This evolved over time to a more fundamental study of spray atomization and droplet impact dynamics and the associated heat transfer phenomena. These two topics are still motivated by CSC, though I also examined applications in flame spray pyrolysis for particulate production, the dispersion of hazardous fluids, and fire suppression. The topic of single droplet impacts stemmed from work at Sandia National Labs that examined the scenario of large-scale tank impacts of hazardous liquids. In efforts to understand the impact and dispersion phenomena of large meter-scale water slugs, it was found that theories predicting millimeter-scale droplet splashing were lacking. What follows is a brief overview of flashing sprays and single droplet splashing.

Nomenclature

A	cross section area
c_p	heat capacity
C	bubble growth constant
d	droplet diameter
$\bar{d}$	mean droplet diameter
D	nozzle diameter
D_{th}	thermal diffusivity of liquid
E	energy
g	gravity
h	enthalpy

h_{fg} latent heat of vaporization
Ja Jakob number, $(\rho_l c_p \Delta T)/\rho_v h_{fg}$
L length
m total mass (m_l+m_g)
$\dot{m}$ total mass flow rate $(\dot{m}_g + \dot{m}_l)$
p pressure
P perimeter
$\dot{q}$ heat flux per unit area
r radius
r_o smallest bubble radius capable of growth
s specific entropy
t time
T temperature
V droplet volume
We Weber number $(\rho v^2 D)/\sigma$
x_g mass fraction (vapor quality)
$\dot{x}$ flow quality
z axial coordinate

Greek letters

θ inclination angle
η efficiency
σ standard deviation
τ shear stress
ψ dimensionless coefficient
ζ available energy of mixture

Subscripts
a ambient
b bubble
d droplet
g gas or vapor
l liquid
TP two-phase

1.1 Flash Atomization

Flashing occurs when a pressurized supercritical, subcooled or saturated fluid is released to a lower pressure, resulting in expansion, violent vapor nucleation, and breakup of the

liquid phase due to thermodynamic instability. Flashing of liquid jets has been studied since the early 1960's [1]. Early works were primarily qualitative visualization studies documenting the phenomenology of the flashing process [2-4]. Later, empirical and semi-theoretical correlations were developed to predict spray properties based on initial conditions, though applicable conditions for these relations were limited [5]. Modeling work of jet breakup and droplet dispersion has also been performed for limited situations [6-8]. Recently, due to advances in spray diagnostics, some quantitative spray characteristic measurements have been performed [9-11] though currently a lack of comprehensive measurements exists and more are needed to facilitate modeling.

Interest in thermodynamic atomization persists due to applications in a variety of areas. Because of the low temperatures possible from a flashing jet, it is being actively studied in the area of cryogenic spray cooling [12-14]. The use of low boiling point liquids such as refrigerants or cryogens in spray cooling is ideally suited in applications requiring very intense cooling or low temperatures, namely in dermatologic laser therapies and high power electronics. Advancement in this area requires better control of spray characteristics, and in turn, of cooling characteristics.

Fine droplet atomization is another attractive feature of flashing sprays. In fuel injection, flashing is being explored to improve fuel atomization in internal combustion engines [15, 16], especially for diesel or direct injection applications where atomization and, thus, combustion efficiency is poor. The fine droplet atomization also has potential in other process applications such as emulsification of immiscible liquids [17] and nanoparticle

production by flame spray pyrolysis [18], though the application of flashing to the latter has not yet been explored.

Also, of great public concern is the risk of release of hazardous pressure liquefied gases (PLG's) during transportation or storage [19, 20]. In recent decades, a variety of highly destructive and deadly release scenarios have occurred (Seveso, Italy, 1976; Bhopal, India, 1984; Mexico City, 1984; Milwaukee, 2006) exposing the need for further risk assessment and safety measures. Past dispersion studies have avoided flashing atomization issues by assuming arbitrary initial release characteristics, making results questionable and of limited usefulness [20]. Scale-up of existing flashing research to the dimensions relevant to industrial releases is currently not possible due to a lack of fundamental understanding of the atomization and dispersions processes. More detailed study of the initial release processes would greatly improve the accuracy of subsequent dispersion predictions.

1.1.1 Thermodynamic Breakup Mechanisms

The basic mechanism behind thermodynamic or flashing breakup involves the transfer of energy from the expansion of vapor bubbles nucleated within the bulk liquid to the surface energy of droplets. This occurs when a pressurized supercritical, subcooled or saturated fluid is suddenly released to a lower, thermodynamically unstable pressure by way of a throttling process. Figure 1.1 illustrates this process with a P vs. T phase diagram. Obviously, if the pressure drop does not cross the liquid/vapor saturation line,

flashing will not occur. Also, the intensity of flashing is dependent upon the superheat, ΔT_{sh}, with a certain minimum threshold superheat required for flashing to occur. Peter et al. [2] identified four breakup regimes, depending on the level of superheat. These are illustrated in Figure 1.2 and represent changes in flow characteristics with increasing superheat. Type 4 or "flare flashing," represents a transition from external flashing to internal flashing in which most or all of the vaporization and liquid phase breakup takes place within the ejection orifice or nozzle. Flashing has also been found to be influenced by the nozzle diameter with larger diameters promoting more violent liquid breakup. This finding has been corroborated by many authors.

The energy exchange taking place was first conceptualized by Brown and York [1] by considering single bubble nucleation. Under adiabatic conditions, the latent heat of vaporization for bubble formation comes from the sensible heat of the bulk liquid. Equilibrium is reached when the residual liquid has cooled to the saturation temperature. A nucleated bubble is subject to three forces: the liquid pressure p_l, the vapor pressure inside the bubble p_g, and the pressure exerted by surface tension $2\sigma/r$. Bubble growth can only occur when the pressure acting outward exceeds the pressure acting inward:

$$p_g > p_l + \frac{2\sigma}{r} \tag{1.1}$$

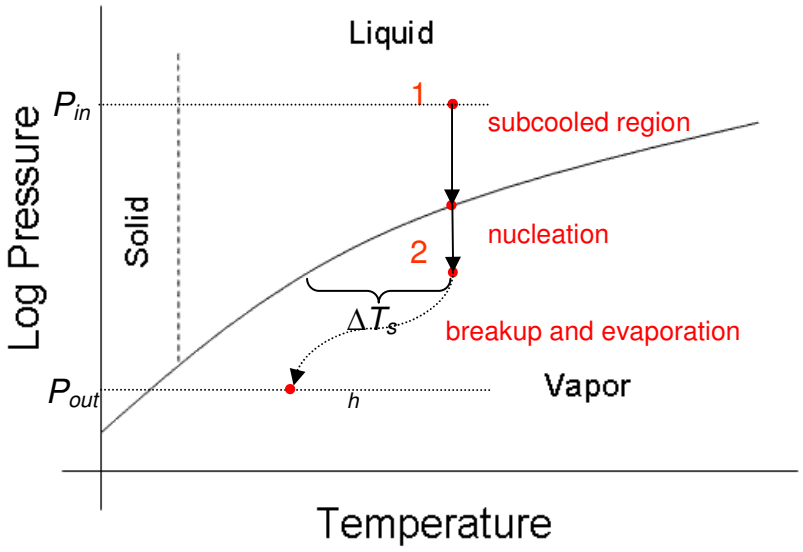

Figure 1.1: Phase diagram of the flashing process.

The smallest bubble capable of growth is, thus:

$$r_o = \frac{2\sigma}{p_g - p_l} \tag{1.2}$$

An important property for the shattering effect of the nucleated bubble is the rate of bubble growth. It is believed that bubble growth initially occurs rapidly because of the relaxation of surface tension pressure and the slow decrease in temperature of the surrounding liquid. After the bubble is approximately ten times its initial size, heat conduction becomes the limiting mode for bubble growth. Bubble radius then becomes a simple function of time:

$$r = 10r_o + Ct^{1/2} \tag{1.3}$$

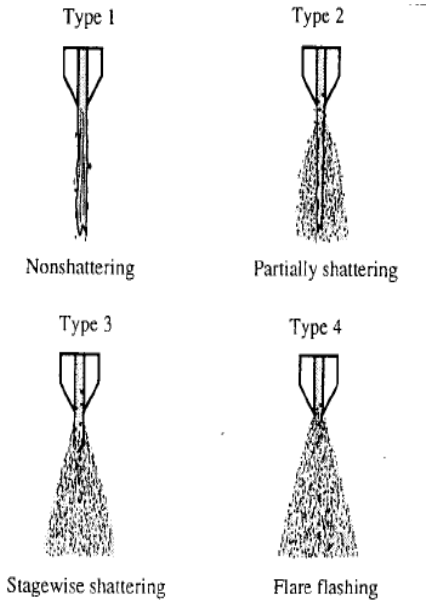

Figure 1.2: The four types of flashing breakup [2].

where C is a bubble growth rate constant. The bubble growth rate constant was developed by Forster and Zuber [21]:

$$C = \psi \left(\frac{c_p \Delta T}{h_{fg}} \right) \left(\frac{\rho_g}{\rho_l} \right) \left(\pi D_{th} \right)^{1/2} \tag{1.4}$$

where the constant ψ is introduced to account for deviation from thermodynamic equilibrium. The first term in parentheses is the weight fraction of liquid flashing. The second term is the specific volume ratio of gas to liquid. The first two terms combined is the volume increase from flashing. The last term represents the rate of heat conduction. It was found that higher *We* flows require lower C values to induce flashing. Hence, mechanical breakup mechanisms may promote flashing.

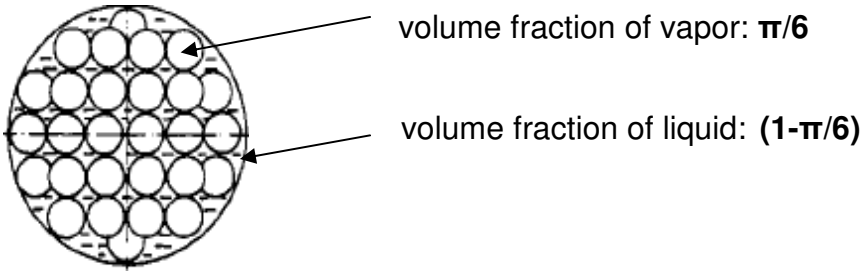

Figure 1.3: Close-packed cubic array of internal bubble growth [7].

Sher and Elata [7] expanded on this idea further to develop a correlation predicting mean droplet size. Using a bubble growth analysis by Plesset and Zwick [22], the equation of motion for bubble growth may be represented by:

$$r\frac{d^2r}{dt^2}+\frac{3}{2}\left(\frac{dr}{dt}\right)^2=\frac{1}{\rho_l}\left(p_g-p_a\right) \tag{1.5}$$

Assuming the vapor to act as an ideal gas and using a linearized Clapeyron equation to determine ΔT, Equations 1.3-1.5 may be combined to produce a relation for pressure difference and C:

$$p_g-p_a=1.8\rho_l\frac{C^2}{t} \tag{1.6}$$

Sher and Elata assumed that flashing would occur when nucleated bubbles formed a close-packed cubic array just touching each other, at which time they would burst (Figure 1.3). The fractional volumes occupied by vapor and liquid are π/6 and 1-π/6, respectively. In this way, the liquid mass of all n_d droplets may be determined.

Sher and Elata postulated that some of the available energy from the bursting bubbles would be converted into the surface energy of the resulting droplets. The energies of bubble bursting and of the generated droplet surfaces are, respectively:

$$E_b = n_b\left(1-\frac{\pi}{6}\right)\int_{r_o}^{r^*} p_b 4\pi r^2 dr \cong m\left(1-\frac{\pi}{6}\right)\frac{4}{3}\pi r^{*3}\left(p_b^* - p_a\right) \tag{1.7}$$

$$E_d = n_d \sigma \pi \bar{d}^2 \tag{1.8}$$

The efficiency, η, is then defined as the ratio of these energies:

$$\eta = \frac{E_d}{E_b} = \frac{n_d \sigma \pi \bar{d}^2}{m\left(1-\frac{\pi}{6}\right)\frac{4}{3}\pi r^{*3}\left(p_b^* - p_a\right)} \tag{1.9}$$

Along the lines of this thought process, Sher and Elata determined an expression for average droplet diameter, $\bar{d}$. This expression, however, suffers from some analytical errors in derivation (most notably in the determination of liquid mass of droplets) and the arbitrary manipulation ψ and n_b in order to fit experimental data.

Sher and Ziegerson-Katz [8] later revised this model by redefining the efficiency:

$$\eta = \frac{E_d}{\zeta_1 - \zeta_2} \tag{1.10}$$

where the denominator is the difference in available energy from the initial to final state. The availability, ζ , of a steady-state flow process is defined as:

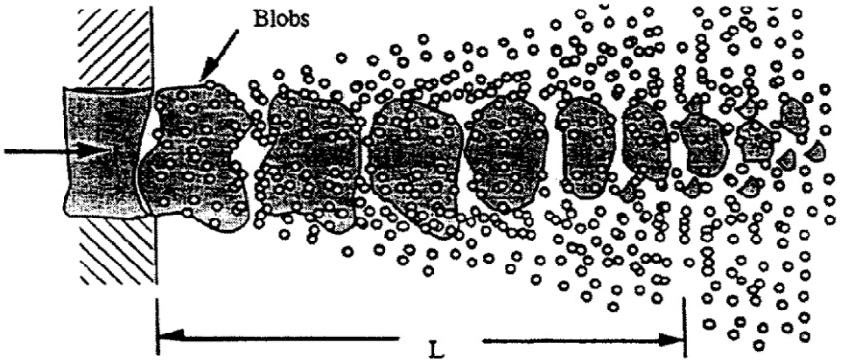

Figure 1.4: The blob model [6].

$$\zeta = \dot{m} \cdot [(h - h_o) - T_o(s - s_o)] \tag{1.11}$$

This analysis, again, suffers from the arbitrary selection of the efficiency, η. The predicted mean diameters also differed from measured data by at least an order of magnitude.

More recent efforts by Zeng and Lee [6] and Chang and Lee [23] known as "blob models" examine the flashing mechanism occurring outside the nozzle while simultaneously considering the effects of mechanical breakup. As illustrated in Figure 1.4, the liquid phase is assumed to exit the orifice as large droplets or "blobs" with diameters of the order of the orifice diameter. A single bubble is assumed to nucleate and expand within each parent droplet causing it to breakup into smaller secondary droplets. The effects of mechanical deformation of the parent droplet are also considered. By using a breakup criterion relating the bubble size to the parent droplet size, the resulting average size, number and velocity of secondary droplets could be determined. The model

was applied to a fuel injection problem and results indicated that flashing did, indeed, substantially reduce droplet sizes. However, the results were not validated with experimental data and the model assumptions appear to be valid only for the situation of slug internal flow and external flashing.

Aside, from modeling efforts, researchers have also attempted to develop empirical correlations to predict flow properties, particularly the conditions for onset of flashing and spray droplet sizes. Kitamura et al. [5] developed a criterion for the onset of flashing by correlating dimensionless *Ja* and *We* numbers:

$$\mathrm{Ja}\,\psi = 100\,\mathrm{We}^{-1/7} \tag{1.12}$$

Ja is the ratio of liquid superheat to heat of vaporization and accounts for a liquid's tendency to flash. It was found that critical *Ja* decreases with increasing *We*, but the correlation fails for high *We* and for situations in which a two-phase effluent existed at the orifice exit. Cleary et al. [24] later revised the coefficient of Equation 1.12 to account for each of the three shattering modes identified in Figure 1.2. Witlox et al. [25] also presented a review of existing flashing droplet size correlations and showed poor agreement among all of them with experimental data. They developed a new correlation predicting Sauter Mean Diameter (d_{32}) as a function of flow properties and nozzle aspect ratio (*L/D*) for subcooled releases [24, 26]:

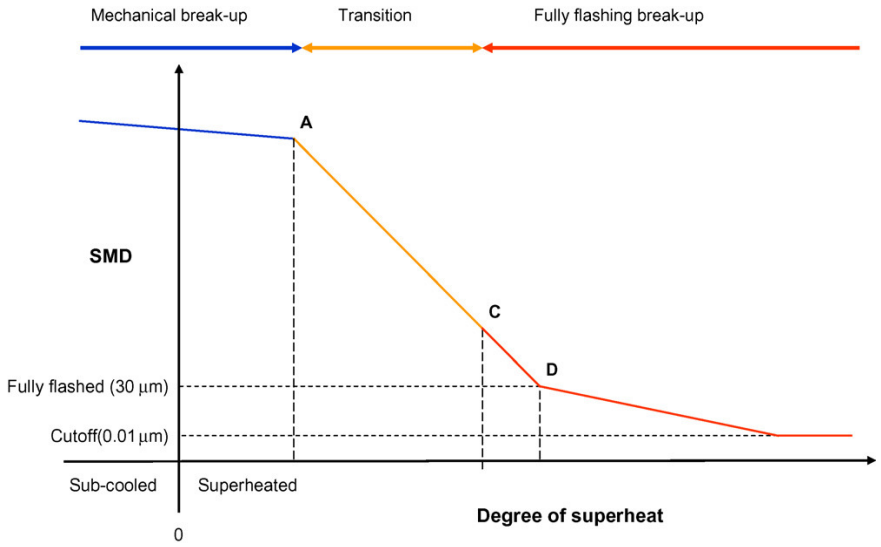

Figure 1.5: Regions of flash atomization [26].

$$\frac{d_{32}}{D} = 64.73\left(\frac{L}{D}\right)^{0.114} \mathrm{Re}_L^{-0.014}\mathrm{We}_l^{-0.533} \tag{1.13}$$

This predicted droplet sizes due to mechanical jet breakup. As shown in Figure 1.5, by including superheat, mechanical breakup will transition to flashing. Transition criteria of the form of Equation 1.12, were implemented to determine these three regions and Equation 1.13 was then reduced linearly in order to conform to a measured data point. The proposed arbitrary linear decreases in diameter are, however, they do not represent any physical processes.

The problems issues with explanation of the physical processes of flashing, and with modeling and correlating measured data likely stem from the fact that internal flow characteristics within the nozzle are not thoroughly considered. Park and Lee [4] have demonstrated the importance of internal flow characteristics on the external spray, albeit

from a strictly qualitative degree. A novel, transparent nozzle was used to visualize internal flow regimes. It is likely that a deliberate, quantitative study of the two-phase internal flow processes will lead to a vastly improved understanding of the flashing process along with better predictive capabilities. A wealth of knowledge already exists on two-phase internal flows. However, this knowledge has not yet been related to the external flow. In the following section, a review of the relevant internal flow theory is presented along with an explanation of its utility in the study of flashing liquid jets.

1.1.2 Internal Flow Theory

Internal two-phase flows involving gases and liquids are highly complex due to the deformability of both phases and the compressibility of the gas phase. Analytical work exists to describe these flows; however, some empiricism is required in order to fully solve practical problems. Below, the governing equation and other theoretical considerations are presented, followed by a qualitative description of the various flow regimes.

Because of the complexity of internal multiphase flows, analyses are normally one-dimensional in space with some averaging performed to determine the properties of each phase. Analyses will generally take two forms: homogeneous or separated flow. Homogeneous flows assume that the phases are flowing at the same velocity (i.e., there is no slip condition between phases) in order to simplify calculations, but accuracy is reduced. Separated flows consider each phase velocity independently and it is this

method that is used herein. According to Hewitt [27], the governing equations for separated gas/liquid flow are:

mass:

$$\frac{\partial}{\partial t}\left(\rho_{TP} A\right)+\frac{\partial}{\partial z}\left(\dot{m} A\right)=0 \tag{1.14}$$

momentum:

$$-\frac{\partial p}{\partial z}=\frac{\tau_W P}{A}+\dot{m}^2 \frac{d}{dz}\left[\frac{\dot{x}_g^2}{\rho_g \varepsilon_g}+\frac{\left(1-\dot{x}_g\right)^2}{\rho_l\left(1-\varepsilon_g\right)}\right]+g\rho_{TP}\sin\theta \tag{1.15}$$

energy:

$$\begin{aligned} &A\frac{\partial}{\partial t}\left[\rho_g \varepsilon_g h_g+\rho_l\left(1-\varepsilon_g\right)h_l\right]+\frac{\partial}{\partial z}\left\{\dot{m}A\left[\dot{x}_g h_g+\left(1-\dot{x}_g\right)h_l\right]\right\}=... \\ &..qP-\frac{\partial}{\partial z}\left\{\dot{m}^3\left[\frac{\dot{x}_g^3}{\rho_g^2\varepsilon_g^2}+\frac{\left(1-\dot{x}_g\right)}{\rho_l^2\left(1-\varepsilon_g\right)^2}\right]\right\}-g\dot{m}A\sin\theta-\frac{\partial}{\partial t}\left\{\dot{m}^2\left[\frac{\dot{x}_g^2}{\rho_g\varepsilon_g}+\frac{\left(1-\dot{x}_g\right)^2}{\rho_l\left(1-\varepsilon_g\right)}\right]\right\}+A\frac{\partial p}{\partial t} \end{aligned} \tag{1.16}$$

Empirical correlations are required to determine the frictional pressure gradient, $\tau_W P/A$, and void fraction, ε_g. Many correlations are available in the literature and those used for the present study are mentioned in Chapter 2.

The flow regimes present within a system will depend on the orientation of the nozzle and relative flow velocities of the phases, among other things. Figure 1.6 presents the flow patterns possible in a vertical and horizontal tube [28]. Often, transition from bubbly to annular flows will occur due to an increase in gas phase flux. Churn or intermittent

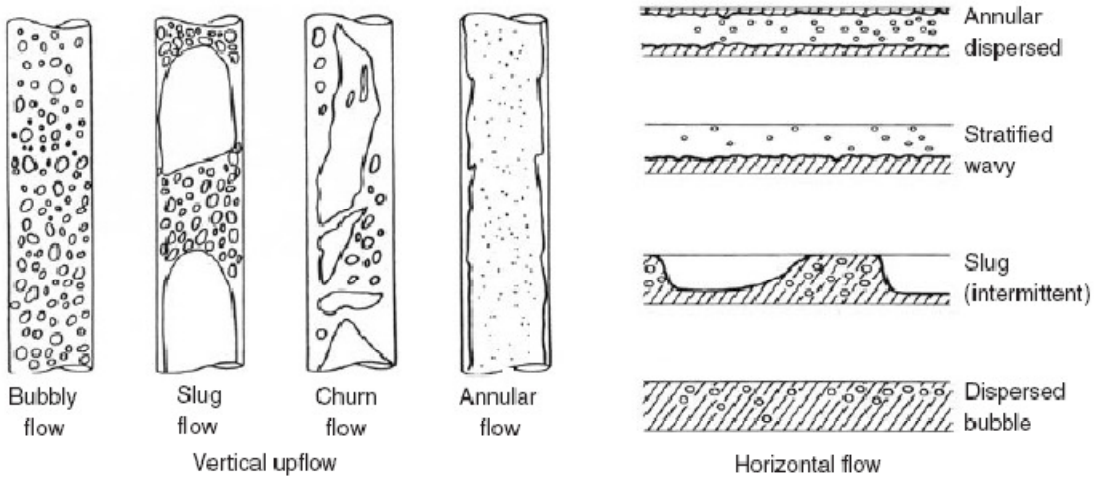

Figure 1.6: Flow regimes for vertical and horizontal flow [28].

flows arise from destabilization of the phase interfaces. One disadvantage of 1-D analyses of internal flows is that flow structure is not evident from calculated data. However, flow pattern maps have been created by several authors in order to predict flow regime from calculable flow properties. An example is provided in Figure 1.7, the well-known vertical two-phase upward flow map by Hewitt and Roberts [29]. The applicability of this and other flow maps have been shown to be limited, however, due to the fact that they do not incorporate all physical phenomena. Care must be taken in their use.

It should be evident that the flow regime, temperature and pressure of the phases, and their relative velocities will have significant impact on the resulting external spray. As mentioned previously, existing works on flash atomization have been deficient in their consideration of these internal flow phenomena. The energy conversion efficiency, η, of

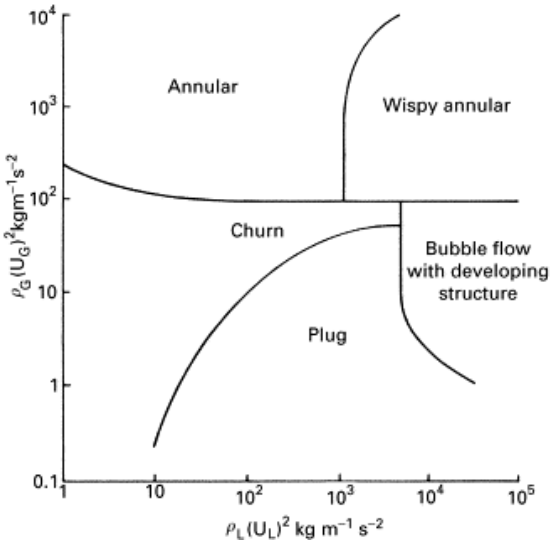

Figure 1.7. Example of a flow regime map [27].

Equation 1.9 may in fact be a function of flow regime. The relative velocity of the phases and the pressure of the gas phase may also have significant effect on the dispersion characteristics. By studying these issues along with upstream and downstream conditions, a more complete picture of the flash atomization process may be developed.

1.1.3 Direct Applications

This study will consider direct application to two topics: dermatological cryogen spray cooling and flame spray pyrolysis. In CSC, the objective is to better understand the atomization mechanisms of the spray and be able to control it to tailor cooling for

specific situations. The FSP application is an exploratory study to determine if flash atomization may be beneficial in nanoparticle production consistency and quality.

1.1.3.1 Dermatological Spray Cooling

In dermatologic laser surgeries of vascular lesions, particularly port wine stains, precooling of the epidermis by means of a refrigerant cooling spray reduces the likelihood of superficial thermal damage due to laser heating [12]. Following flashing atomization, the remaining liquid droplets impinge on the targeted skin surface, resulting in intense, short-duration cooling. This method of skin cooling has been used in conjunction with laser therapy for over a decade. However, clinical studies have demonstrated that the success rate of these treatments remains as low as 25%. Insufficient cooling, and radial non-uniformities in cooling protection [30, 31] may be significant reasons for this poor therapeutic outcome. Additionally, a novel approach to improve therapeutic outcome has recently been proposed using vacuum suction which changes the release pressure [32, 33]. Substantial work has already been performed on the optical [34-38] and spray cooling heat transfer aspects of the problem, but little attention has been given to the spray atomization mechanisms. This, coupled with the current poor fundamental understanding of flashing atomization mechanisms, in general, are the motivations for the current work.

Our group has already performed preliminary work specifically pertaining to cryogenic spray cooling in dermatology. It has been shown that modifying the diameter of the spray nozzles can have dramatic effects on the resulting spray characteristics (Figure 1.8) [39].

Larger diameter nozzles were shown to produce jet-like flows with large droplets (Figure 1.8a) while smaller diameter nozzles could produce much finer and more dispersed atomization (Figure 1.8b). No explanation was provided, however, as to mechanisms for these differences and actually appears to be contradictory to the work of others who found larger diameter nozzles to produce more explosive flashing. The following work may help to elucidate these issues.

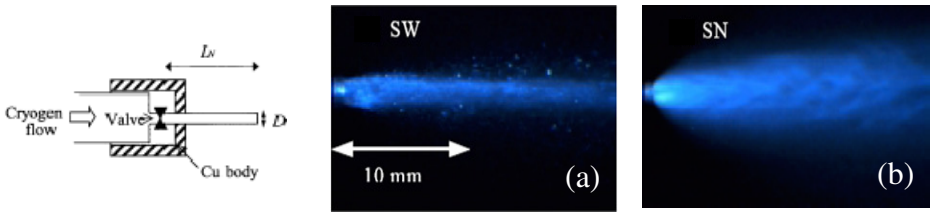

Figure 1.8. Sprays formed from (a) 1.4 mm and (b) 0.7 mm diameter nozzles [39].

1.1.3.2 Flame Spray Pyrolysis

These same principles may be applied to flame spray pyrolysis (FSP) of ceria particles for catalysis of soot from diesel engines [40]. Traditional operation of the spray burner requires atomization of a liquid precursor jet by a coaxial gas flow that also functions as the oxidant and fuel. In this way, the atomization quality of the spray is coupled with the combustion characteristics, particularly flame length. This has made control of nanoparticle characteristics difficult as they are heavily dependent on both initial droplet size and flame residence time. Existing research of FSP by others is largely empirical and focused on precursor and fuel choices, flame characteristics and other combustion aspects [41].

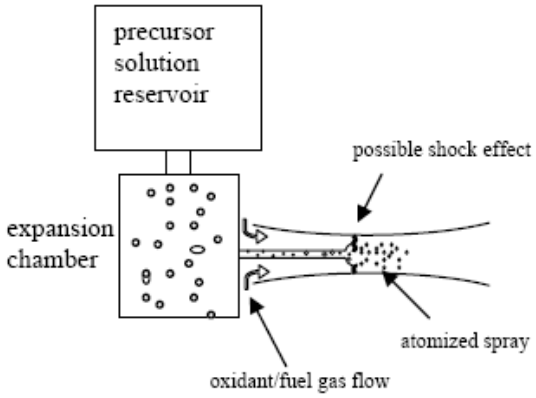

Figure 1.9: A proposed application of flashing sprays in FSP.

The flashing mode of atomization may be introduced to the existing coaxial air-blast atomizer by pressurizing and heating the precursor liquid prior to injection as conceptualized in Figure 1.9. Under appropriate conditions, this may allow for independent control of oxidant/fuel gas flow rate without affecting atomization quality. The effects of the coaxial gas flow and presence of the flame are, however, unknown and must be determined.

Desirable droplet characteristics for ceria formation are very small droplet diameters within a narrow, symmetric distribution to enable more complete combustion of the precursor and more uniform particle sizes. Existing air-blast atomizers will produce droplets in the 10 micron range with a high throughput. An alternative technique using electrosprays will produce more desirable nano-sized droplets, but have much lower throughput [42]. The incorporation of flashing phenomena to the air-blast atomizer may improve control of atomization and reduce droplet sizes while still maintaining high throughput.

1.2 Single Droplet Splashing

The splashing phenomenon that occurs after a liquid droplet impacts onto a solid or liquid surface was first studied by Worthington [43]. Although the physical mechanisms of splashing are still not completely understood, droplet impact against solid and liquid surfaces have been widely used for materials processing, ink printing, spray cooling, and irrigation. Engel [44] showed that the pressure variation inside the droplet during impact was the key factor that caused splashing. Studies of droplet impacts at velocities over 100 m/s against a rigid surface showed that splashing may be attributed to a pressure related shockwave, which is initiated due to the compression of the front part of the droplet at the beginning stage of contact against the rigid solid surface [45-52]. Then, when the momentum of the liquid droplet cannot convert into the momentum of flow along the impact surface during the impact process, splashing occurs at the location where the surface energy is the least [53, 54]. This assumption has been supported by experimental measurements, which were taken when surface roughness was increased [55-57] and when a vertical obstacle was added on the solid surface [58]. Both the surface roughness and vertical obstacles reduce the momentum of flow along the impact surface. As a result, the pressure at the front edge of the flow along the impact surface increases to facilitate splashing.

Additionally, Allen [59] applied Rayleigh-Taylor (R-T) instability theory to demonstrate that splashing was one of the products of instability formation. Recent research, however, has shown that Kelvin-Helmholtz (K-H) instability, which is caused by the shear stress between two fluids moving in parallel at a relative velocity, provides a better explanation

of splashing than R-T instability theory because it considers the exchange of momentum between the air underneath and the droplet as the latter it about to impact the solid surface [60, 61]. In this context, Xu et al. [62, 63] discovered that as the ambient pressure drops to 0.17 atm, splashing could not be observed. A more detailed description of the interaction between a water droplet and ambient gas during impact was presented by Jepsen et al. [64], who used the Schlieren photography method to observe the gas movement, which varied with the ambient pressure during a water slug impact onto a solid surface. Additionally, Yoon et al. [65] presented further evidence for K-H instability through imaging of finger formation in droplets impacting into liquid pools where fluid density differences did not exist.

Experimental methods have been applied to find the quantitative threshold of splashing during droplet impact based on *We* and *Re*. These studies have related the threshold of splashing to liquid properties, such as the surface tension and viscosity, and also to the impact surface characteristics [66-71]. K-H instability, however, has generally not been considered in splashing threshold correlations, nor has the effect of ambient pressure and impact angle been studied together systematically.

In this study, I attempt to clarify the mechanisms of single droplet splashing on smooth surfaces, particularly examining the effects of ambient air pressure and fluid viscosity and develop new, more reliable correlations predicting the onset of splashing.

References

1. Brown, R. and J.L. York, *Sprays Formed by Flashing Liquid Jets.* Aiche Journal, 1962. **8**(2): p. 149-153.
2. Peter, E.M., A. Takimoto, and Y. Hayashi, *Flashing and Shattering Phenomena of Superheated Liquid Jets.* Jsme International Journal Series B-Fluids and Thermal Engineering, 1994. **37**(2): p. 313-321.
3. Reitz, R.D., *A Photographic Study of Flash-Boiling Atomization.* Aerosol Science and Technology, 1990. **12**(3): p. 561-569.
4. Park, B.S. and S.Y. Lee, *An Experimental Investigation of the Flash Atomization Mechanism.* Atomization and Sprays, 1994. **4**(2): p. 159-179.
5. Kitamura, Y., H. Morimitsu, and T. Takahashi, *Critical Superheat for Flashing of Superheated Liquid Jets.* Industrial & Engineering Chemistry Fundamentals, 1986. **25**(2): p. 206-211.
6. Zeng, Y.B. and C.F.F. Lee, *An atomization model for flash boiling sprays.* Combustion Science and Technology, 2001. **169**: p. 45-67.
7. Sher, E. and C. Elata, *Spray Formation from Pressure Cans by Flashing.* Industrial & Engineering Chemistry Process Design and Development, 1977. **16**(2): p. 237-242.
8. Sher, E. and M. ZeigersonKatz, *Spray formation by flashing of a binary mixture: An energy balance approach.* Atomization and Sprays, 1996. **6**(4): p. 447-459.

9. Allen, J.T., *Laser-based measurements in two-phase flashing propane jets. Part one: velocity profiles.* Journal of Loss Prevention in the Process Industries, 1998. **11**(5): p. 291-297.

10. Allen, J.T., *Laser-based measurements in two-phase flashing propane jets. Part two: droplet size distribution.* Journal of Loss Prevention in the Process Industries, 1998. **11**(5): p. 299-306.

11. Knubben, G. and C.W.M. van der Geld, *Drop size distribution evolution after continuous or intermittent injection of butane or propane in a confined air flow.* Applied Thermal Engineering, 2001. **21**(7): p. 787-811.

12. Nelson, J.S., et al., *Dynamic Epidermal Cooling During Pulsed-Laser Treatment of Port-Wine Stain - a New Methodology with Preliminary Clinical-Evaluation.* Archives of Dermatology, 1995. **131**(6): p. 695-700.

13. Aguilar, G., et al., *Theoretical and experimental analysis of droplet diameter, temperature, and evaporation rate evolution in cryogenic sprays.* International Journal of Heat and Mass Transfer, 2001. **44**(17): p. 3201-3211.

14. Hsieh, S.S. and H.H. Tsai, *Thermal and flow measurements of continuous cryogenic spray cooling.* Archives of Dermatological Research, 2006. **298**(2): p. 82-95.

15. Senda, J., et al., *Characteristics of Spray Injected from Gasoline Injector.* Jsme International Journal Series B-Fluids and Thermal Engineering, 1994. **37**(4): p. 931-936.

16. Nishimura, Y., et al. *An experimental study on flash boiling spray using two-component fuel under the condition of advanced injection HCCI*. in *10th International Conference on Liquid Atomization and Spray Systems*. 2006. Kyoto, Japan.

17. Helfgen, B., M. Turk, and K. Schaber, *Hydrodynamic and aerosol modelling of the rapid expansion of supercritical solutions (RESS-process).* Journal of Supercritical Fluids, 2003. **26**(3): p. 225-242.

18. Heine, M.C. and S.E. Pratsinis, *Droplet and particle dynamics during flame spray synthesis of nanoparticles.* Industrial & Engineering Chemistry Research, 2005. **44**(16): p. 6222-6232.

19. Bowen, P.J. and L.C. Shirvill, *Combustion Hazards Posed by the Pressurized Atomization of High-Flashpoint Liquids.* Journal of Loss Prevention in the Process Industries, 1994. **7**(3): p. 233-241.

20. Johnson, D.W. and J.L. Woodward, *Release: a model with data to predict aerosol rainout in accidental releases*. 1999, New York: American Institute of Chemical Engineers. 184.

21. Forster, H.K. and N. Zuber, *Growth of a Vapor Bubble in a Superheated Liquid.* Journal of Applied Physics, 1954. **25**(4): p. 474-478.

22. Plesset, M.S. and S.A. Zwick, *The Growth of Vapor Bubbles in Superheated Liquids.* Journal of Applied Physics, 1954. **25**(4): p. 493-500.

23. Chang, D.L. and C.F.F. Lee, *Development of a simplified bubble growth model for flash boiling sprays in direct injection spark ignition engines.* Proceedings of the Combustion Institute, 2005. **30**: p. 2737-2744.

24. Cleary, V., P. Bowen, and H. Witlox, *Flashing liquid jets and two-phase droplet dispersion I. Experiments for derivation of droplet atomisation correlations.* Journal of Hazardous Materials, 2007. **142**(3): p. 786-796.

25. Witlox, H.W.M. and P.J. Bowen, *Flashing liquid jets and two-phase dispersion: A review*. 2002, Health and Safety Executive: Suffolk, UK.

26. Witlox, H., et al., *Flashing liquid jets and two-phase droplet dispersion II. Comparison and validation of droplet size and rainout formulations.* Journal of Hazardous Materials, 2007. **142**(3): p. 797-809.

27. Hewitt, G.F., *Multiphase Fluid Flow and Pressure Drop*, in *Heat exchanger design handbook*, e.-i.-c.K.J.B.e.a. Ernst U. Schlünder, Editor. 1983, Hemisphere Publishing Corp.: Washingtion. p. 2.3.1-1 to 2.3.2-33.

28. Oliemans, R.V.A. and B.F.M. Pots, *Gas-Liquid Transport in Ducts*, in *Multiphase Flow Handbook*, C.T. Crowe, Editor. 2006, CRC : Taylor & Francis: Boca Raton, FL. p. 2.1-2.40.

29. Hewitt, G.F. and D.N. Roberts, *Studies of two phase flow patterns by simultaneous x-ray and flash photography*. 1969, The United Kingdom Atomic Energy Authority.

30. Franco, W., et al., *Radial and temporal variations in surface heat transfer during cryogen spray cooling.* Physics in Medicine and Biology, 2005. **50**(2): p. 387-397.

31. Franco, W., et al., *Extent of lateral epidermal protection afforded by a cryogen spray against laser irradiation.* Lasers in Surgery and Medicine, 2007. **39**(5): p. 414-421.

32. Aguilar, G., L.O. Svaasand, and J.S. Nelson, *Effects of hypobaric pressure on human skin: Feasibility study for port wine stain laser therapy (part 1).* Lasers in Surgery and Medicine, 2005. **36**(2): p. 124-129.

33. Aguilar, G., et al., *Effects of hypobaric pressure on human skin: Implications for cryogen spray cooling (part II).* Lasers in Surgery and Medicine, 2005. **36**(2): p. 130-135.

34. Aguilar, G., et al., *Measurement of heat flux and heat transfer coefficient during continuous cryogen spray cooling for laser dermatologic surgery.* Ieee Journal of Selected Topics in Quantum Electronics, 2001. **7**(6): p. 1013-1021.

35. Aguilar, G., H. Vu, and J.S. Nelson, *Influence of angle between the nozzle and skin surface on the heat flux and overall heat extraction during cryogen spray cooling.* Physics in Medicine and Biology, 2004. **49**(10): p. N147-N153.

36. Pfefer, T.J., et al., *Bioheat transfer analysis of cryogen spray cooling during laser treatment of port wine stains.* Lasers in Surgery and Medicine, 2000. **26**(2): p. 145-157.

37. Tunnell, J.W., J.H. Torres, and B. Anvari, *Methodology for estimation of time-dependent surface heat flux due to cryogen spray cooling.* Annals of Biomedical Engineering, 2002. **30**(1): p. 19-33.

38. Verkruysse, W., et al., *Optimal cryogen spray cooling parameters for pulsed laser treatment of port wine stains.* Lasers in Surgery and Medicine, 2000. **27**(2): p. 165-170.

39. Aguilar, G., et al., *Experimental study of cryogen spray properties for application in dermatologic laser surgery.* Ieee Transactions on Biomedical Engineering, 2003. **50**(7): p. 863-869.

40. Madler, L., W.J. Stark, and S.E. Pratsinis, *Flame-made ceria nanoparticles.* Journal of Materials Research, 2002. **17**(6): p. 1356-1362.

41. Kammler, H.K., L. Madler, and S.E. Pratsinis, *Flame synthesis of nanoparticles.* Chemical Engineering & Technology, 2001. **24**(6): p. 583-596.

42. Lenggoro, I.W., et al., *Colloidal nanoparticle analysis by nanoelectrospray size spectrometry with a heated flow.* Analytica Chimica Acta, 2007. **585**: p. 193-201.

43. Worthington, A., *On the froms assumed by drops of liquids falling vertically on a horizontal plate.* Proc. R. Soc. London, 1876. **25**: p. 261-271.

44. Engel, O.G., *Waterdrop Collisions with Solid Surfaces.* Journal of Research of the National Bureau of Standards, 1955. **54**(5): p. 281-298.

45. Bowden, F.P. and J.E. Field, *Brittle Fracture of Solids by Liquid Impact by Solid Impact + by Shock.* Proceedings of the Royal Society of London Series a-Mathematical and Physical Sciences, 1964. **282**(139): p. 331-&.

46. Hobbs, P.V. and A.J. Kezweeny, *Splashing of a Water Drop.* Science, 1967. **155**(3766): p. 1112-&.

47. Hobbs, P.V. and T. Osheroff, *Splashing of Drops on Shallow Liquids.* Science, 1967. **158**(3805): p. 1184-&.

48. Levin, Z. and P.V. Hobbs, *Charge Separation Due to Splashing of Water Drops.* Bulletin of the American Meteorological Society, 1970. **51**(6): p. 577-&.

49. Levin, Z. and P.V. Hobbs, *Splashing of Water Drops on Solid and Wetted Surfaces - Hydrodynamics and Charge Separation.* Philosophical Transactions of the Royal Society of London Series a-Mathematical and Physical Sciences, 1971. **269**(1200): p. 555-&.

50. Lesser, M.B., *Analytic Solutions of Liquid-Drop Impact Problems.* Proceedings of the Royal Society of London Series a-Mathematical Physical and Engineering Sciences, 1981. **377**(1770): p. 289-308.

51. Lesser, M.B. and J.E. Field, *The Impact of Compressible Liquids.* Annual Review of Fluid Mechanics, 1983. **15**: p. 97-122.

52. Field, J.E., M.B. Lesser, and J.P. Dear, *Studies of Two-Dimensional Liquid-Wedge Impact and Their Relevance to Liquid-Drop Impact Problems.* Proceedings of the Royal Society of London Series a-Mathematical Physical and Engineering Sciences, 1985. **401**(1821): p. 225-&.

53. Harlow, F.H. and J.P. Shannon, *Splash of a Liquid Drop.* Journal of Applied Physics, 1967. **38**(10): p. 3855-&.

54. Stow, C.D. and M.G. Hadfield, *An Experimental Investigation of Fluid-Flow Resulting from the Impact of a Water Drop with an Unyielding Dry Surface.*

Proceedings of the Royal Society of London Series a-Mathematical Physical and Engineering Sciences, 1981. **373**(1755): p. 419-441.

55. Range, K. and F. Feuillebois, *Splashing of a drop on a rough surface.* High Temperature Material Processes, 1998. **2**(2): p. 287-300.

56. Range, K. and F. Feuillebois, *Influence of surface roughness on liquid drop impact.* Journal of Colloid and Interface Science, 1998. **203**(1): p. 16-30.

57. Field, J.E., *ELSI conference: invited lecture - Liquid impact: theory, experiment, applications.* Wear, 1999. **235**: p. 1-12.

58. Josserand, C., et al., *Droplet impact on a dry surface: triggering the splash with a small obstacle.* Journal of Fluid Mechanics, 2005. **524**: p. 47-56.

59. Allen, R.F., *Role of Surface-Tension in Splashing.* Journal of Colloid and Interface Science, 1975. **51**(2): p. 350-351.

60. Kim, H.Y., Z.C. Feng, and J.H. Chun, *Instability of a liquid jet emerging from a droplet upon collision with a solid surface.* Physics of Fluids, 2000. **12**(3): p. 531-541.

61. Yoon, S.S., et al., *Experimental investigation on splashing and nonlinear fingerlike instability of large water drops.* Journal of Fluids and Structures, 2007. **23**(1): p. 101-115.

62. Xu, L., W.W. Zhang, and S.R. Nagel, *Drop splashing on a dry smooth surface.* Physical Review Letters, 2005. **94**(18): p. 184505-1-4.

63. Xu, L., *Liquid drop splashing on smooth, rough, and textured surfaces.* Physical Review E, 2007. **75**(5): p. 056316-1-8.

64. Jepsen, R.A., S.S. Yoon, and B. Demosthenous, *Effects of air on splashing during a large droplet impact: Experimental and numerical investigations.* Atomization and Sprays, 2006. **16**(8): p. 981-996.

65. Yoon, S.S., et al., *Are drop-impact phenomena described by Rayleigh-Taylor or Kelvin-Helmholtz theory?* Drying Technology, 2009. **27**: p. 1-6.

66. Mundo, C., M. Sommerfeld, and C. Tropea, *Droplet-Wall Collisions - Experimental Studies of the Deformation and Breakup Process.* International Journal of Multiphase Flow, 1995. **21**(2): p. 151-173.

67. Rein, M., *Phenomena of Liquid-Drop Impact on Solid and Liquid Surfaces.* Fluid Dynamics Research, 1993. **12**(2): p. 61-93.

68. Prunet-Foch, B., et al., *Impacting emulsion drop on a steel plate: Influence of the solid substrate.* Journal of Colloid and Interface Science, 1998. **199**(2): p. 151-168.

69. Kang, B.S. and D.H. Lee, *On the dynamic behavior of a liquid droplet impacting upon an inclined heated surface.* Experiments in Fluids, 2000. **29**(4): p. 380-387.

70. Rioboo, R., C. Tropea, and M. Marengo, *Outcomes from a drop impact on solid surfaces.* Atomization and Sprays, 2001. **11**(2): p. 155-165.

71. Rioboo, R., et al., *Experimental investigation of splash and crown formation during single drop impact on wetted surfaces.* Experiments in Fluids, 2003. **35**(6): p. 648-652.

CHAPTER 2: Vapor/Liquid Phase Interaction in Flare Flashing Sprays Used in Dermatologic Cooling

In this work, a one-dimensional model of refrigerant flow in capillary tube expansion devices [1-3] is used to characterize internal flashing nozzle flow. The model is validated for this present case, and, combined with detailed external spray studies, it provides new insight into this atomization process. No known work has attempted to quantitatively characterize the internal flow conditions within the nozzle and relate them to quantitative external spray characteristics. The present study examines the case of flare flashing of a high superheat liquid in large *L/D* ratio nozzles, a situation similar to current dermatologic cooling spray systems.

Nomenclature

A	cross section area
$\vec{A}$	droplet surface area vector
c_p	heat capacity
C_D	drag coefficient
CS	control surface
CV	control volume
d	droplet diameter
D	nozzle diameter
D_{10}	arithmetic average droplet diameter
f	friction factor
F_d	drag force
g	gravity
G	vapor phase generation
h	enthalpy
h_{fg}	latent heat of vaporization
k	Gaussian distribution function

L	length
m	total mass (m_l+m_g)
$\dot{m}$	total mass flow rate $(\dot{m}_g + \dot{m}_l)$
M	mass of liquid at bursting per unit volume
p	pressure
P	perimeter
$\dot{q}$	heat flux per unit area
r	radius
R_{134a}	gas constant for R134a
s	specific entropy
t	time
T	temperature
u	internal energy
v	velocity
V	droplet volume
$\vec{V}$	droplet evaporation velocity vector
$\forall$	total droplet volume
We	Weber number $(\rho v^2 D)/\sigma$
x_g	mass fraction (vapor quality)
$\dot{x}$	flow quality
z	axial coordinate

Greek letters

α	heat transfer coefficient [$Wm^{-2}K^{-1}$]
Δz	spatial discretization step
ε_g	void fraction
ϕ	generic dependent variable
Φ	two-phase frictional multiplier
θ	inclination angle
ρ	density
σ	standard deviation
τ	shear stress
ξ	$h + v^2/2 + gz\sin\theta$

Subscripts

a	ambient
d	droplet
dis	discharge
f	fluid
g	gas or vapor
j	measurement location index within external spray
l	liquid

P PDPA measurement probe
stag stagnation
w wall

Superscripts
- arithmetical average over a *CV*: $\bar{\phi} = (\phi_i + \phi_{i+1})/2$
~ integral average over a *CV*: $\tilde{\phi} = (1/\Delta z)\int_z^{z+\Delta z} \phi dz$
+ value at previous iteration
* value at bursting
$[X]_i^{i+1} = X_{i+1} - X_i$

2. 1 Methodology

The basic setup of for the problem of study is depicted in Figure 2.1. A pressurized liquid (R134a, water or methanol) is contained within a pressure chamber at saturation conditions or above. This liquid is released to a round-orifice tube nozzle of varying dimensions and exits to, typically, the atmosphere at room conditions—though the release environment may be modified by reducing its pressure or humidity. The internal flow is studied primarily by numerical modeling, with some high speed imaging using transparent glass nozzles. The external spray is studied by imaging, phase Doppler measurement, and other diagnostic techniques available. Details of the more complicated methodologies are described below.

2.1.1 Internal Flow

2.2.1.1 Numerical Model

The highly dynamic flow within the nozzle is calculated by dividing it into control volumes (*CV*) shown schematically in Figure 2.2, where '*i*' and '*i*+1' represent the inlet and outlet mass flow cross section areas, respectively.

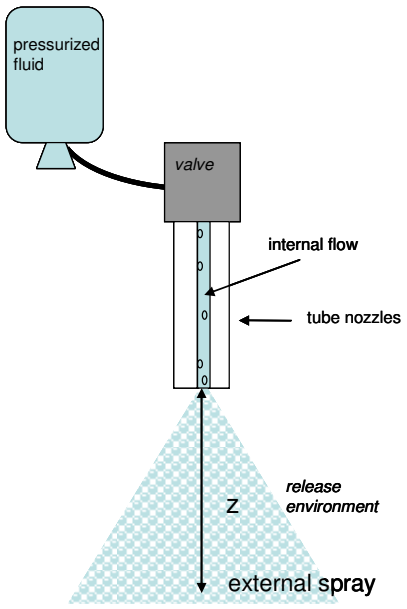

Figure 2.1: Setup of the R134a flashing spray.

Taking into account the physical characteristics of the nozzle (diameter, length, roughness, inclination angle, etc.), the governing equations (2.1-2.4) are integrated with the following assumptions: constant internal diameter, uniform surface roughness, separated flow in which the liquid and gas velocities are treated independently, negligible axial heat conduction inside the fluid, negligible radiation effects and *CV* of fixed dimensions. The general semi-integrated governing equations over the above mentioned finite *CV*, have the following form:

Continuity:

$$\left[\dot{m}\right]_{i}^{i+1}+\frac{\partial m}{\partial t}=0 \qquad (2.1)$$

Momentum:

$$\left[\dot{m}_g v_g\right]_i^{i+1} + \left[\dot{m}_l v_l\right]_i^{i+1} + \Delta z \frac{\partial \tilde{\dot{m}}}{\partial t} = -[p]_i^{i+1} A - \tilde{\tau}_w P \Delta z - mg\sin\theta \tag{2.2}$$

Energy:

$$\left[\dot{m}_l \xi_l + \dot{m}_g \xi_g\right]_i^{i+1} + \frac{\partial\left(\bar{\dot{m}}_l \bar{\xi}_l + \bar{\dot{m}}_g \bar{\xi}_g\right)}{\partial t} - A\Delta z \frac{\partial \tilde{p}}{\partial t} = \tilde{q}_w P \Delta z \tag{2.3}$$

where $\xi = h + v^2/2 + gz\sin\theta$.

Entropy:

$$\left[\dot{m}_l s_l + \dot{m}_g s_g\right]_i^{i+1} + \frac{\partial\left(\bar{\dot{m}}_l \bar{s}_l + \bar{\dot{m}}_g \bar{s}_g\right)}{\partial t} - \frac{\tilde{\dot{q}}_w P \Delta z}{\bar{T}_w} \geq 0 \tag{2.4}$$

The entropy equation has been added in order to determine the conditions for which choking will occur at the exit.

The evaluation of the shear stresses are carried out by means of a friction factor f and a two-phase multiplier Φ which are included in the following expression for wall shear stress: $\tau_w = \Phi(f/4)(\dot{m}^2/2\rho A^2)$.. The heat transfer through the nozzle wall and the fluid temperature are related by the convective heat transfer coefficient α, which is defined as: $\alpha = \dot{q}_w/(T_w - T_f)$.

Boundary conditions are specified at the inlet and outlet sections of the nozzle (Figure 2.2) and along the tube wall (wall surface roughness and heat flux or temperature

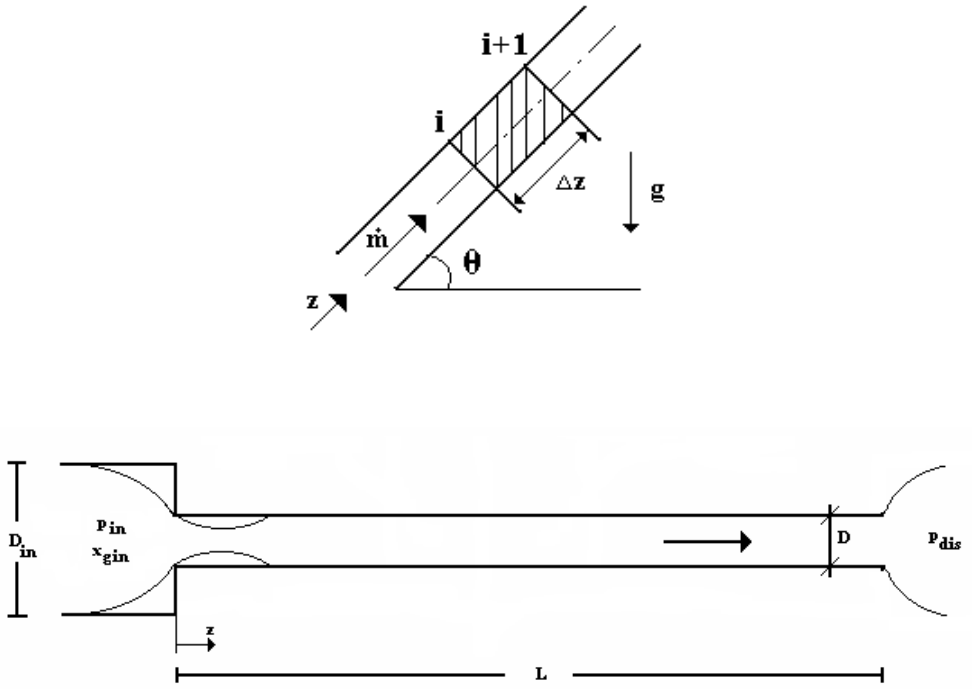

Figure 2.2: Schematic diagram of a *CV* and nozzle.

distribution). At the *inlet section* the fluid may be saturated, subcooled, or supercritical, so the appropriate inlet pressure (p_{in}) and vapor mass fraction (x_{gin}) should be determined from existing literature. The *outlet* or *discharge section* pressure (p_{dis}) is dependent on the surrounding environmental conditions of the application of interest.

As explained before, the void fraction (ε_g) and wall frictional effects must be computed from empirical correlation. The choice of correlations depends on the application and flow conditions. The following have been selected for the DSC application: ε_g is computed by a semi-empirical equation proposed by Rouhani and Axelsson [4] for a drift flux model that considers the effects of the mass velocity, surface tension and buoyancy.

The friction factor (f) is evaluated from the expressions proposed by Churchill [5] with a correction factor (Φ) according to Friedel [6]. These correlations have been widely used in refrigeration system studies in the past.

The convective heat transfer coefficient (α) is evaluated using the Shah correlation [7] and natural convection between the nozzle tube and the ambient is considered using the correlation developed by Churchill and Chu [8].

The simulation computes the mass flow rate of each phase at any location within the nozzle together with the flow variables (pressure, temperature, mass fraction, velocity, etc.).

Because of the high gradients in flow variables present at the end of the nozzle, a non-uniform grid concentrated at the outlet section is generated as described in García-Valladares [9]. Mesh-independent solutions are obtained with each computational domain consisting of 300 *CV*s. For each *CV*, a set of algebraic equations is obtained by the discretization of the governing equations (2.1-2.4). The discretized equations are coupled using a fully-implicit, step-by-step method in the flow direction. From the known values at the inlet section and the wall boundary conditions, the variable values at the outlet of each *CV* are iteratively obtained from the discretized equations. This solution (outlet values) is the inlet condition for the next *CV*. A strict convergence condition, $\left(1-\left|\left(\phi_{i+1}^{+}-\phi_i\right)/\left(\phi_{i+1}-\phi_i\right)\right|\right)<10^{-7}$, must be verified in each *CV* for passing to the next time step.

The numerical global algorithm is as follows: the inlet mass flow rate is iteratively estimated by means of a numerical Newton-Raphson algorithm to obtain critical or choked flow conditions. Critical flux conditions are reached when Equation 2.4 is not verified in the last *CV*, since entropy reaches its maximum value at the location of choking. To check critical conditions the criterion $dp/dz \rightarrow \infty$ is sometimes reported in the literature. For the cases presented here both criteria are equivalent.

After critical conditions are evaluated, the critical pressure and external release pressure are compared. If the critical pressure is greater, the flow is critical and all calculated flow parameters remain valid. Otherwise, the flow is non-critical and the mass flow rate that offers an outlet pressure equal to the release pressure is evaluated by means of another Newton-Raphson algorithm.

2.2.1.2 Numerical Model Validation

To justify the model assumptions and empirical correlations used, the model must be validated. This is typically done by comparing measurable quantities of temperature and pressure along the nozzle axis and at the exit with those computed by the model. Because the model was developed for capillary tubes of very large *L/D* ratios, this validation becomes especially important for low ratio nozzles where wall effects may not be as significant and where metastable phenomena may be prevalent. Overall mass flow rates may also be measured by weighing the storage container before and after a specified duration of release.

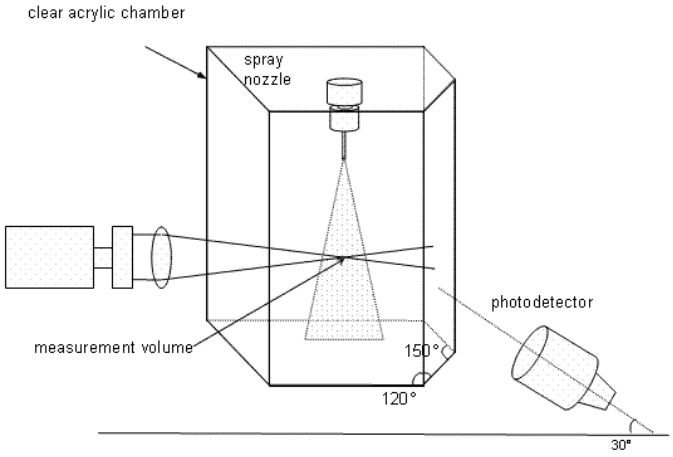

Figure 2.3: PDPA schematic with acrylic chamber.

2.1.2 External Flow

2.1.2.1 Phase Doppler Particle Analyzer

External spray droplet characteristics are determined using a Phase Doppler Particle Analyzer (PDPA; TSI Incorporated, Shoreview, MN) to measure the velocities and diameters of spherical droplets. A 300 mW Argon-Ion laser is used producing beams of wavelength 488 nm and 514.5 nm enabling velocity measurements in two axes. This study only considers axial velocities with respect to the nozzle, so only the 514.5 nm light beams are used. Because of the high density of the spray near the nozzle exit, the likelihood for beam extinction or the detection of multiple particles simultaneously in the measurement volume increases. Since the PDPA is essentially a single particle counter, these effects lead to a lower validated data rate. However, a lowered data rate does not

necessarily impact the accuracy of the validated data since the rejected data is not biased toward a particular velocity or diameter range [10, 11]. To compensate for the lowered data rate, more measurement runs are performed. Yildiz et al. [12] and Allen and Bettis [13] have verified the ability to use laser Doppler techniques in the harsh optical environments of flashing sprays. More details on PDPA operation can be found elsewhere [10, 11, 14].

In order to reduce the influence of condensable ambient air humidity on the measured spray characteristics or to control the release pressures, the spray system may be contained within a custom-made clear acrylic chamber shown in Figure 2.3. Chamber walls are 12.7 mm (0.5 in) thick and oriented to be perpendicular to the transmitting and receiving probes to minimize refractive effects.

2.1.2.2 Gas Phase Velocity Measurement

In order to determine the gas phase velocity of the external flow (distinct from the liquid droplet velocities measured by PDPA), a Pitot-type technique is employed using a diaphragm-based pressure transducer (PX302-200GV, Omega Engineering, Stamford, CT). A short length of narrow tubing is attached to the end of the transducer in order to localize the area of measurement to the central axis of the spray and extend it away from the large transducer body. The opening of the tube is inserted into the spray axis perpendicular to the flow to measure the stagnation pressure, p_{stag}. Steady-state pressure measurements are used to determine the velocity of the gas flow from Equations 2.5-2.6:

$$p_{meas} = p_{stag} - p_{static} = \rho_g \frac{v^2}{2} \tag{2.5}$$

$$v = \sqrt{2\frac{p_{stag} - p_{static}}{\rho_g}} \tag{2.6}$$

Because the transducer measures gage pressure, the static pressure, p_{static}, is the pressure within the spray that is above ambient. By orienting the pressure transducer perpendicular to the flow direction, p_{static} can be measured. The density of the gas phase, ρ_g, is dependent on temperature and mass fraction of fluid vapor. These values are computed from measurable quantities and will be described later. Based on the accuracy of the pressure transducer, estimated errors in calculated velocities are expected to be within ±35 m/s. For a measured velocity range of nearly 0 to 300 m/s, this represents a sizable error so results should be interpreted accordingly.

Because the gas phase pressure measurements are taken within a two-phase flow, the influence of the discontinuous liquid phase must be determined. The pressure induced by droplet impingement on the pressure transducer diaphragm may be determined by simple momentum conservation:

$$p_d = \frac{F_d}{A_P} = \frac{\dot{m}_d v_d}{A_P} \tag{2.7}$$

where A_p is the area of the PDPA measurement probe (point of intersecting laser beams, ~$5x10^{-8}$ m^2). In order to obtain the mass flow rate, the number of droplets passing through the probe must be determined. This is complicated by the fact that the number of valid droplet signals detected by the system does not necessarily represent the true number of droplets since undetected or invalidated droplets may exist. Others have considered this issue and developed statistical arguments to account for them. It is beyond the scope of this proposal to describe them, so the reader is referred to an existing work [15]. The pressure, p_d, may then be computed and subtracted from p_{meas} to determine the gas phase velocity.

2.2 Results and Discussion

The following results are applicable to the case of DSC. The fluid of interest is R134a with nozzle dimensions of D = 0.5 mm and lengths of 20, 40, and 80 mm. This work demonstrates the capability of the internal flow model and the utility of the external measurements.

2.2.1 Model Validation

Results for the numerical model validation are given in Table 2.1. For this study, because the fluid and nozzle dimensions are similar to those of previous studies, only the exit temperature and overall mass flow rates are measured. The three analyzed cases present choked (critical) flow. The mass flow rate and exit temperatures calculated for all of them

are within reasonable errors to experimental values. The other predicted flow variables of interest are taken to be accurate.

2.2.2 Internal Flow

Figure 2.4 presents internal nozzle flow data for variables of interest. Figure 2.4a indicates that both pressure and temperature are reduced continuously along the length of the tube nozzle. Lengthening the nozzle offers more wall surface area and higher frictional resistance so the pressure is reduced further. Temperature reductions are due to the latent heat of vaporization and expansion of the gas phase. Hence, exit values of pressure and temperature for longer nozzles are lower due to the increased wall effects.

Table 2.1: Model Validation

	Experimental data		**Numerical model**			
Nozzle Length [mm]	*Mass flow [g/s]*	*Outlet Temp. [K]*	*Mass flow [g/s]*	*error [g/s]*	*Outlet Temp. [K]*	*error [K]*
20	1.25	271.3	1.32	0.07	271.83	0.53
40	1.12	267.7	1.13	0.01	267.74	0.04
80	0.90	262.25	0.91	0.01	262.99	0.74

Figure 2.4b shows that liquid velocity increases gradually along the length of the nozzle though slightly lower liquid exit velocities are apparent for longer nozzles. This corroborates the reduced mass flow rates shown earlier in Table 2.1 and is likely due to the greater frictional resistance. Higher gas phase velocities are observed, however, for

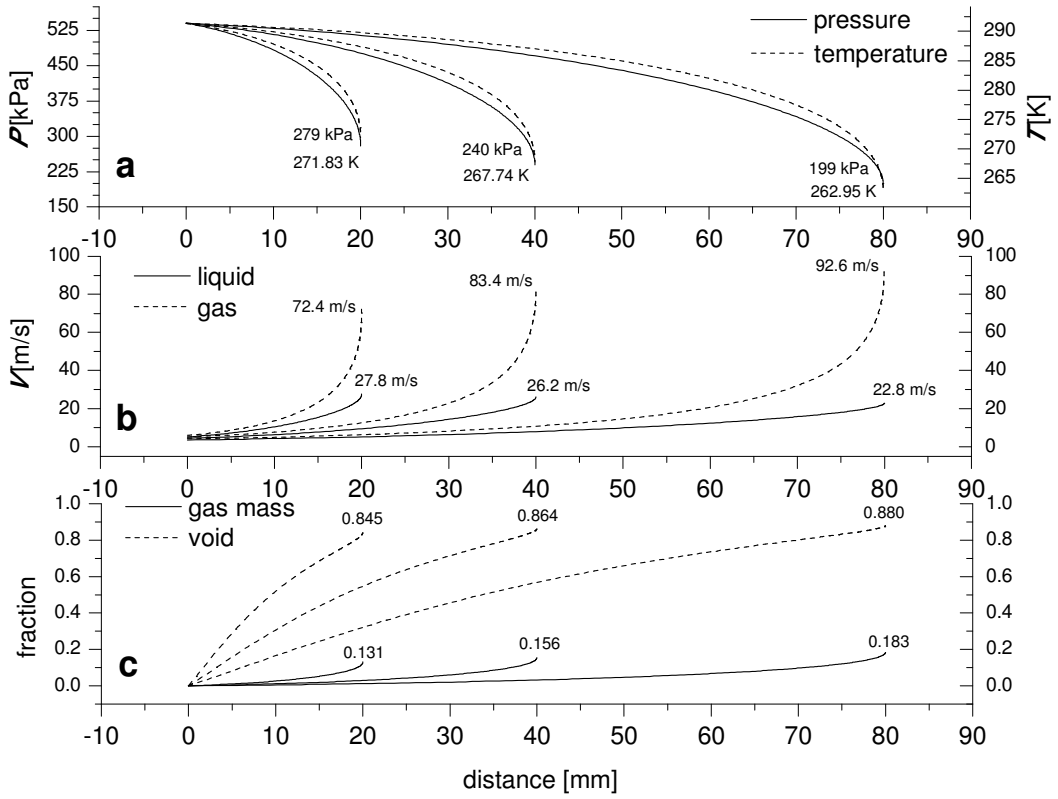

Figure 2.4: Model results for internal nozzle (a) pressure and temperature, (b) velocity and (c) void fraction and mass fraction of gas.

the longer nozzles. Longer nozzles, therefore, have larger exit velocity differentials between phases.

Figure 2.4c shows both mass (x_g) and void (ε_g) fractions of the gas phase. Again, the liquid evaporates due to the pressure drop as it progresses through the nozzle. Longer length nozzles produce a slight increase in the outlet vapor quality (mass fraction) and void fraction (volume fraction of vapor).

2.2.3 External Flow

Centerline spray characteristics of the external flow are given in Figure 2.5. Remarkably, the droplet velocities of Figure 2.5a continue to display an increase in magnitude away from the nozzle for a significant distance before decreasing again. This observation has also been made by Yildiz et al. [12] for similar sprays. The magnitude of acceleration of the spray in the near field of the nozzle appears to be larger for longer length nozzles, since they have lower exit velocities, yet achieve approximately the same maximum velocities. This may be due to the higher velocity differentials between the liquid and gas phases, as pointed out earlier. Once maximum velocities have been reached, droplet deceleration occurs at approximately the same rate for all nozzle lengths for $z > 25$ mm.

Measured arithmetic average droplet diameters (D_{10}) of Figure 2.5b appear to be unstable within the range of 1-30 mm from the nozzle exit. Detectable droplet sizes appear to achieve maximum at 5 mm followed by an abrupt decrease. A slight increase occurs over the range of 15-30 mm, after which a consistent gradual decline ensues. The fluctuation

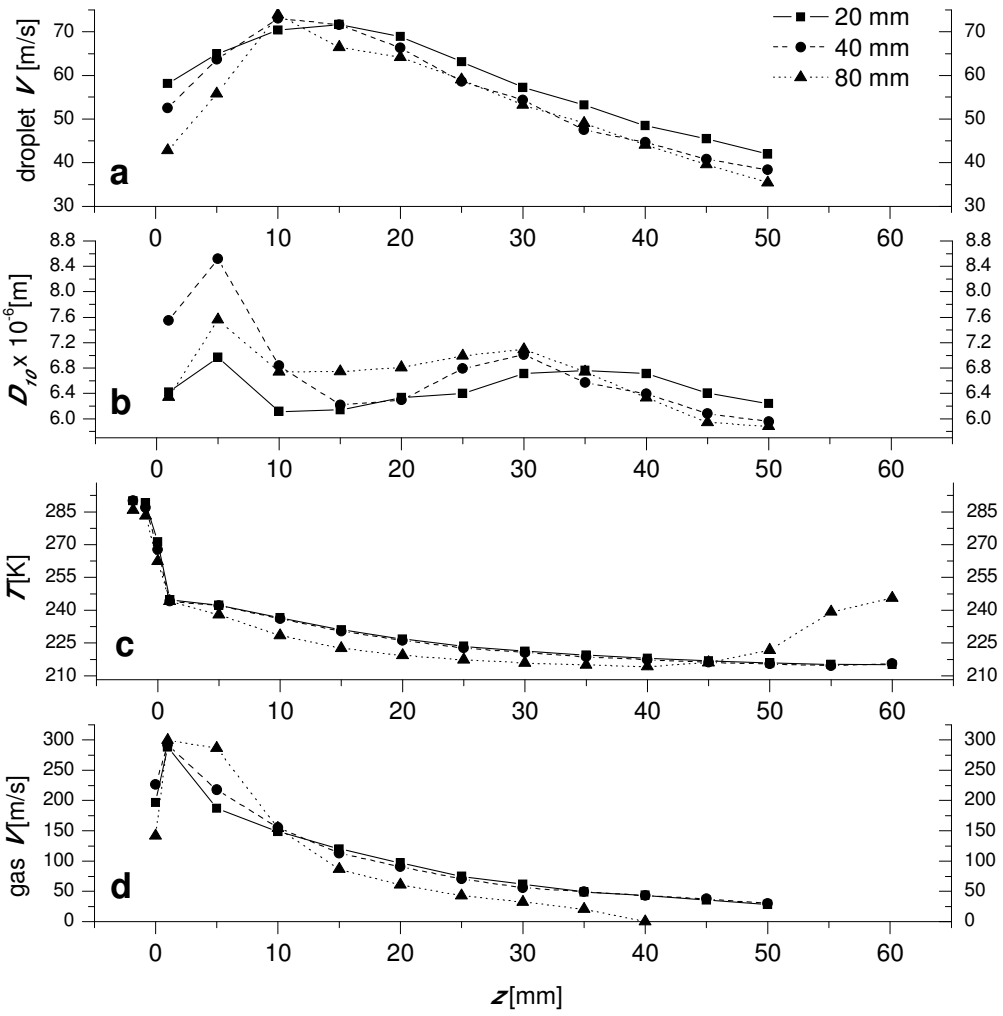

Figure 2.5: Experimental results for spray characteristics: (a) droplet velocity, (b) arithmetic average droplet diameter, (c) spray temperature (d) gas velocity.

in droplet sizes at $z < 30$ mm may be due to the low validation rate and low number of samples so D_{10} values may have large errors within this range [16], as mentioned before.

Spray temperatures are provided for all nozzle lengths in Figure 2.5c. Some measurements are taken at 1 and 2 mm *within* the nozzle by insertion of the miniature thermocouple bead into the nozzle to demonstrate the abrupt temperature change near the nozzle exit. Temperatures decrease rapidly to approximately boiling temperature (~-26 °C) as the liquid flash boils upon exiting the nozzle. Spray temperatures continue to decrease beyond the boiling point, albeit at a much slower rate. This phenomenon was observed by Aguilar et al. [17] for R134a sprays and may be attributed to the low surface tension and latent heat of vaporization of the liquid (both about 1 order of magnitude lower than water), making continuous evaporation and cooling of the droplets possible. Temperatures for the 40 mm nozzle are very slightly lower than for 20 mm. Temperatures for the 80 mm nozzle are more significantly lower between the range of 1-40 mm. This could possibly be attributed to smaller or fewer droplets exiting the nozzle, which would reduce in temperature more easily. The increase in temperature occurring beyond 40 mm may be due to the complete evaporation of a significant number of droplets.

From spray pressure measurements, gas phase velocities are computed using Equation 2.6 and given in Figure 2.5d. Gas velocities accelerate to nearly 300 m/s for all nozzles before gradually decelerating, but remain higher than droplet velocities within about 20 mm from the nozzle exit. Afterwards, both phases are about the same. Gas velocities

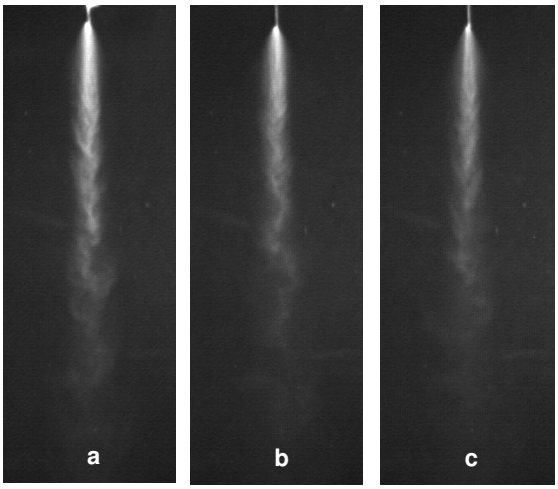

Figure 2.6. Flash lamp photography images of the spray formed from a (a) 20 mm, (b) 40 mm, and (c) 80 mm nozzle.

remain higher for the longer length nozzles up until about 10 mm, after which a more rapid deceleration occurs.

Flash lamp photography images of the spray in Figure 2.6 indicate visually the effect of nozzle length on the spray characteristics. With identical lighting conditions, there is a slight reduction in the intensity of the reflected flash light with increasing nozzle length. This may be due to the reduced flux of liquid at the nozzle exit, meaning fewer or smaller spray droplets. Spray penetration is also reduced indicating, again, that spray droplets will evaporate more quickly for longer length nozzles. Aside, from these observations, there appears to be little difference among the nozzle lengths. For all three cases, spray cone expansion seems to be very high within the first few mm from the nozzle, after which a more gradual expansion ensues.

2.3 Vapor/Liquid Phase Interaction

A new treatment of the external spray is proposed, based on the exit flow parameters predicted by the internal flow model which provide all necessary boundary conditions at $z = 0$. This treatment addresses a dispersion aspect of flash atomization and explains the measured *increase in spray droplet velocity away from the nozzle*.

Because of the large void fraction and difference in velocities between the liquid and gas phases, the external flow is treated as a continuous gas phase, with dispersed liquid droplets. The velocities of the droplets are greatly influenced by the surrounding continuous phase because of their small mass. Due to drag forces, the droplets are, therefore, accelerated by the faster flowing gas phase. To determine the droplet drag force, the pressure and density of the surrounding gas must be known. It is necessary, therefore, to know the evaporation rate of the liquid and track the expansion of the spray cone. Using the measured experimental data, the effective spray droplet drag coefficient (C_D) is then determined at each location and is compared to data in existing literature from similar problems. Because of the similarity in exit flow parameters and measured spray characteristics among the nozzles, treatment assumptions and expressions are the same for all nozzle lengths considered in this study.

Theoretically, the evaporation rate of the liquid can be determined by tracking the change in droplet size distribution along the spray axis. Droplet sizes will reduce as liquid evaporates from the droplet surfaces. The PDPA, however, cannot measure accurately near the nozzle exit where the spray is very dense. Referring again to the droplet size

measurements in Figure 2.5b, there is not a trend of decreasing droplet size until after z = 30-40 mm. Since further away from the nozzle the PDPA measurements are reliable, the droplet sizes nearer to the nozzle can be determined by starting with the size measurement far from the nozzle, and back-calculating the droplet evaporation necessary for the measured temperature changes (Figure 2.5c) through an energy and mass balance. The droplet diameter histograms measured at z = 50 mm for the 20 and 40 mm nozzles and at z = 40mm for the 80 mm nozzle are fitted to a Gaussian distribution:

$$\boldsymbol{k}(\boldsymbol{d}) = \frac{1}{\sigma\sqrt{2\pi}} \exp\left(\frac{-\left(\boldsymbol{d} - \bar{\boldsymbol{d}}\right)^2}{2\sigma^2} \right) \tag{2.8}$$

where σ is the standard deviation of the distribution and $\bar{\boldsymbol{d}}$ is the mean value of diameter. The calculation is started at z = 40mm for the 80 mm nozzle because that is the location of lowest temperature. Standard deviation is assumed to remain constant for each position.

The use of droplet size distributions is an improvement on a previous work by the authors [18] in which only a single representative droplet was used to account for the entire spray liquid volume. The latter over-predicted droplet sizes at the nozzle exit and overall droplet evaporation due to the much lower surface area to volume ratio of a single representative droplet in comparison to a droplet population.

The total distribution of droplet sizes, collectively, is taken to be the system of interest. The loss of internal energy of the population is equal to the latent heat of vaporization of the liquid. Heating of the droplets from the environment is assumed to be negligibly

small in comparison, so it is ignored. The rate of evaporation is determined through a mass balance. The *Reynolds Transport Theorem* is used to determine the energy and mass balances of the droplet population:

$$-\frac{\partial}{\partial t}\int_{CV} u\rho d\forall = \int_{CS} h_{fg}\rho\vec{v}\cdot d\vec{A} \tag{2.9}$$

$$-\frac{\partial}{\partial t}\int_{CV} \rho d\forall = \int_{CS} \rho\vec{v}\cdot d\vec{A} \tag{2.10}$$

where h_{fg} is latent heat of vaporization. Liquid density is assumed to be constant and kinetic and potential energies are neglected in the energy equation. The reference internal energy is taken to be zero at z = 40-50 mm at the location of the start of the calculation, and internal energy change is calculated as $\Delta u = \Delta h = C\Delta T$, where C is the heat capacity of the liquid. Since fluid properties are taken to be constant, the volume and surface integrals of Equations 2.9-2.10 can be easily integrated:

$$-\frac{\partial}{\partial t} u\rho\forall = h_{fg}\rho vA \tag{2.11}$$

$$-\frac{\partial}{\partial t}\rho\forall = \rho vA \tag{2.12}$$

These equations are then combined and used to form a simple relation between the total droplet population volumes between two points:

$$\forall_j \left(\frac{\boldsymbol{u}_j - 2\boldsymbol{u}_{j-1} + \boldsymbol{h}_{fg}}{\boldsymbol{h}_{fg} - \boldsymbol{u}_{j-1}} \right) = \forall_{j-1} \tag{2.13}$$

where the time derivative is determined by simple differencing between two measurement points. To determine the total droplet volume, $\forall$, the following expression is used assuming all droplets are spheres:

$$\forall = \int_0^{\boldsymbol{d}_{\max}} \frac{4}{3}\pi \left(\frac{\boldsymbol{d}}{2} \right)^2 \frac{1}{\sigma\sqrt{2\pi}} \exp\left(\frac{-\left(\boldsymbol{d} - \bar{\boldsymbol{d}}\right)}{2\sigma^2} \right) d\boldsymbol{d} \tag{2.14}$$

This equation is integrated from zero to the maximum expected diameter using the trapezoidal rule.

The resulting droplet distributions for the 40 mm nozzle are plotted in Figure 2.7 (distributions for the other two nozzles are similar so they are not shown). Note that these curves show a slight shift to the left with increasing *z*, indicating a gradual evaporation.

Next, vapor generation is determined by the difference in total droplet mass between measurement points multiplied by the total number of droplets existing at the nozzle exit:

$$G_j = \left[\rho_l \left(\forall_{j-1} - \forall_j \right) \right] \left[\frac{\left(1 - \varepsilon_g\right)\left(\pi \frac{D^2}{4}\right)}{\int_0^{d_{\max}} 4\pi \left(\frac{d_o}{2} \right)^2 \frac{1}{\sigma\sqrt{2\pi}} \exp\left(\frac{-\left(d_o - \bar{d}_o\right)}{2\sigma^2} \right) dd_o} \right] \tag{2.15}$$

The first bracketed term represents the change in droplet mass due to evaporation while the second term is the theoretical number of droplets existing at the nozzle exit. The

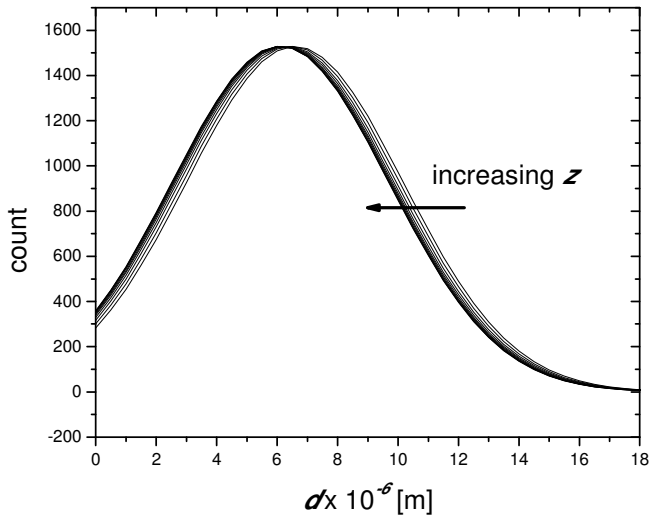

Figure 2.7: Results of energy and mass balance on droplet diameter distribution.

second term is estimated by the number of droplets necessary to occupy the liquid *area* at the exit. Equation 2.15 can be used as a source term for vapor generation in spray modeling. For the present conditions, however, the effects of evaporation and vapor generation on gas phase densities are found to be very small since the majority of phase change appears to take place within the nozzle.

Once the vapor generation has been calculated, the gas phase density and pressure evolution may be determined. First, the spray cone width as a function of z is measured from the high-speed flash lamp images of the spray. The measurement points are then fitted to a second-order exponential function to reduce measurement error as shown in Figure 2.8a. Again, spray cone widths were similar for all three nozzle lengths so only the result for the 40 mm nozzle is shown.

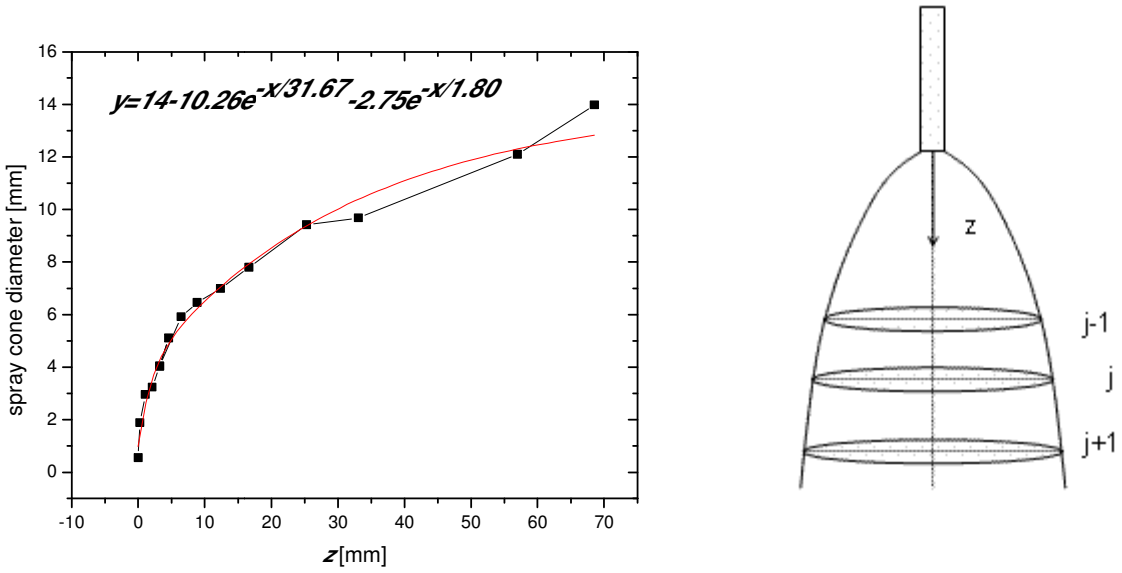

a **b**

Figure 2.8: (a) Spray cone diameter for 40 mm length nozzle and (b) 2-D slices of spray cone perpendicular to z at each measurement.

Next, the gas phase pressures are solved by using a two-dimensional approach, considering slices of the spray cone at the measurement points, j (Figure 2.8b). The gas properties are assumed to be uniform within each slice. The total mass of refrigerant gas at any point, M_{134a}, is determined by the sum of the mass of gas at the nozzle exit and the gas generated by evaporation, G. The ideal gas law with compressibility factor is then used to compute the partial pressure of the refrigerant gas:

$$p_{134a,j} = Z_{134a,j} \frac{M_{134a,j} R_{134a} T_j}{A_{g,j} L_j} \tag{2.16}$$

where Z is the compressibility factor at saturation conditions, A_g is total area of gas phase and L_j is the distance between j and j-1. A_g is determined by first calculating the area of the liquid and subtracting this from the total spray area determined from Figure 2.8a.

$$A_{g,j} = A_{total,j} - A_{l,j} = A_{total,j} - \left(A_{l,j-1} - \frac{G_j}{\rho_l L_j} \right) \tag{2.17}$$

After exiting the nozzle, the calculated vapor pressure of the refrigerant appears to be below atmospheric pressure for all locations except for z=1mm, meaning the spray expands at a much faster rate than the rate of evaporation of liquid. The total gas pressure is, however, assumed to remain at least at atmospheric to avoid a vacuum condition. The remaining partial pressure necessary to reach atmospheric is assumed to come from dry air through entrainment. This allows for the calculation of total gas phase density, ρ_g, according to:

$$\rho_{g,j} = \frac{p_{134a,j}}{R_{134a} T_j} + \left(\frac{101000 - p_{134a,j}}{R_{air} T_j} \right) \tag{2.18}$$

After calculating the gas phase density, the drag coefficients relating the liquid and vapor phase velocities can be determined. Unlike for droplet sizes, only *mean* droplet velocities need be considered because velocities are about the same for all droplet sizes, as verified by the diameter-velocity correlations determined from the PDPA measurements and shown in Figure 2.9.

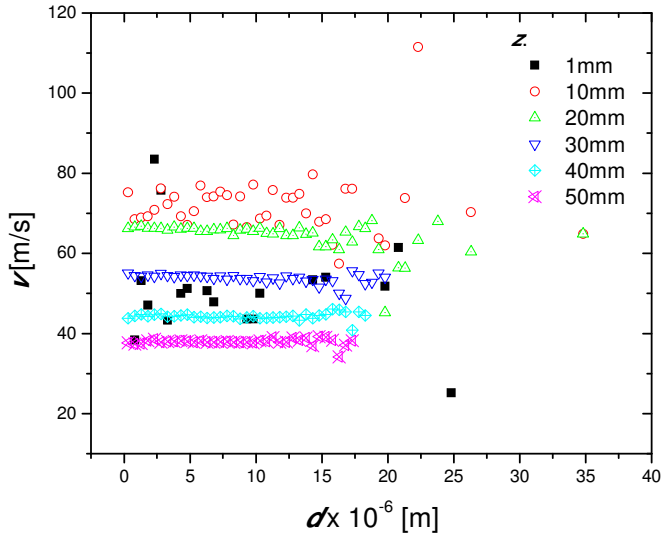

Figure 2.9: Graph of droplet velocity versus diameter for the 40 mm length nozzle.

Using droplet velocity data, a drag force may be computed at each j location using Newton's Second Law.

$$\boldsymbol{F_D} = \left(\rho_{l,j}\,\frac{4}{3}\pi \boldsymbol{r}_j^3\right)\left(\frac{\boldsymbol{v}_j - \boldsymbol{v}_{j-1}}{\boldsymbol{t}_j}\right) \tag{2.19}$$

where t_j is the time of flight of the droplet between j and j-1.

Drag force, however, can also be represented by the constitutive relation: $\boldsymbol{F_D} = 0.5\left(\boldsymbol{v_g} - \boldsymbol{v_l}\right)^2 \rho \boldsymbol{C_D A}$ where the term in parentheses is the *relative* velocity between the surrounding gas and droplet. This relation can be used to determine the drag coefficient between the liquid and gas phases:

$$C_D = \frac{2F_D}{\rho_g A\left(v_g - v_l\right)^2} \tag{2.20}$$

Computed drag coefficients for all nozzles are plotted together versus droplet *Re* in Figure 2.10. The results exhibit an approximately linear relationship between C_D and *Re* so a least squares regression fit was performed and given below:

$$\boldsymbol{C_D} = \frac{200}{\mathrm{Re}^{1.6}} \qquad (0.1<Re<2000) \tag{2.21}$$

Some scatter is apparent in the higher *Re* range, from 20-2000, where droplets are very near the nozzle exit and velocity measurement errors are likely to be more significant. Within this *Re* range, the droplets may also be in a transition region where flow turbulence is a factor along with possible shockwave effects. The widely used Stokes and Kliachko drag relations [19] and Rudinger [20] relation are also shown for comparison. There is clear deviation from these relations, though the slope is nearly identical to Rudinger who obtained his expression using shock tube experiments. The Stokes relation also appears to approximate the current data well in the higher *Re* range but not in the low. The similarity in slope of Equation 2.21 with the Rudinger correlation may be due to the fact that both were obtained under high accelerations. Flow perturbations are known to greatly influence drag coefficients and produce deviations from "classical" steady-state correlations. Also, droplet evaporation, which would clearly change liquid/gas interaction, may play a role.

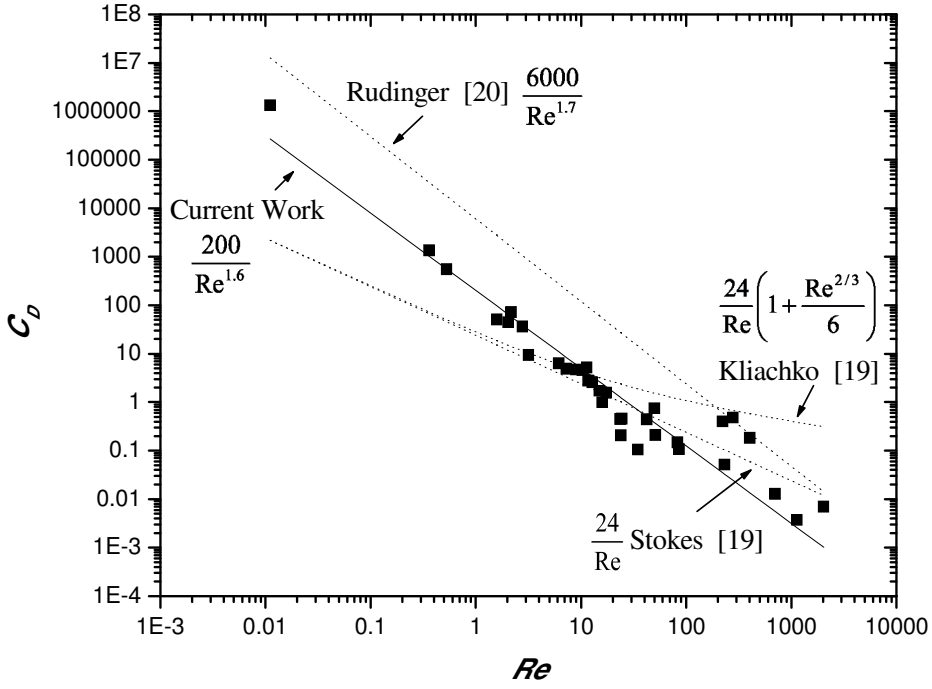

Figure 2.10. Flashing spray droplet drag coefficients and comparison to existing work. *Re* limits are $50 < Re < 300$ for the Rudinger correlation and $0.1 < Re < 2000$ for the Current Work.

2.4 Conclusions

This work represents the first known effort quantifying internal nozzle flow parameters and its significance to the external spray characteristics of a flashing spray. It was found that for the conditions of high superheat and larger *L/D* ratio nozzles found in current dermatologic spray cooling devices, critical flow conditions are reached in which a choking condition develops at the nozzle exit. Increasing nozzle lengths had the effect of reducing liquid exit velocity and total mass flow rate while increasing the vaporization of

the liquid phase and the gas phase velocity. External spray measurements, however, generally exhibited little difference among the nozzle lengths. This indicates that the differences in internal flow, namely the increased vaporization occurring in the longer nozzles, are not significant to the development of the resulting external flow. With nozzles of smaller aspect ratios, however, noticeable differences in external flow may occur and have indeed been observed by other researchers referenced earlier in the paper.

Spray droplet diameters were found to be unreliable within about 30 mm from the nozzle exit, but a technique was developed in which theoretical Gaussian droplet diameter distributions could be determined near the nozzle through mass and energy balances. Both liquid and gas phases were found to accelerate for some distance away from the nozzle. Some new relations were also developed describing the interaction of the two phases and assumes that the droplets are suspended within the continuous gas phase and accelerated by its expansion. A new empirical correlation for C_D was developed for droplets under the higher acceleratory fields of flashing sprays. The results of this work may assist future modeling efforts of flashing spray formation and dispersion for dermatologic cooling and other applications.

References

1. Johnson, D.W. and J.L. Woodward, *Release: a model with data to predict aerosol rainout in accidental releases*. 1999, New York: American Institute of Chemical Engineers. 184.
2. Yildiz, D., et al. *Evolution of the spray characteristics in superheated liquid jet atomization in function of initial flow conditions*. in *10th International Conference on Liquid Atomization and Spray Systems*. 2006. Kyoto, Japan.
3. Forster, H.K. and N. Zuber, *Growth of a Vapor Bubble in a Superheated Liquid.* Journal of Applied Physics, 1954. **25**(4): p. 474-478.
4. Rouhani, S.Z. and E. Axelsson, *Calculation of Void Volume Fraction in Subcooled and Quality Boiling Regions.* International Journal of Heat and Mass Transfer, 1970. **13**(2): p. 383-393.
5. Churchill, S.W., *Friction-Factor Equation Spans All Fluid-Flow Regimes.* Chemical Engineering, 1977. **84**(24): p. 91-92.
6. Friedel, L. *Improved friction pressure drop correlation for horizontal and vertical two-phase pipe flow*. in *European Two-Phase Flow Group Meeting*. 1979. Ispra, Italy.
7. Shah, M.M., *Chart correlation for saturated boiling heat transfer: equations and further study.* ASHRAE Transactions, 1982. **88**: p. 185-196.
8. Churchill, S.W. and H.H.S. Chu, *Correlating Equations for Laminar and Turbulent Free Convection from a Vertical Plate.* International Journal of Heat and Mass Transfer, 1975. **18**(11): p. 1323-1329.

9. García-Valladares, O., D.C. Perez-Segarra, and A. Oliva, *Numerical simulation of capillary tube expansion devices behaviour with pure and mixed refrigerants considering metastable region. Part I: mathematical formulation and numerical model.* Applied Thermal Engineering, 2002. **22**(2): p. 173-182.

10. Bachalo, W.D., *Experimental Methods in Multiphase Flows.* International Journal of Multiphase Flow, 1994. **20**: p. 261-295.

11. Bachalo, W.D., *The Phase Doppler Method - Analysis, Performance Evaluations, and Applications.* Particle & Particle Systems Characterization, 1994. **11**(1): p. 73-83.

12. Yildiz, D., J. van Beeck, and M.L. Riethmuller, *Feasibility exploration of laser-based techniques for characterization of a flashing jet.* Particle & Particle Systems Characterization, 2004. **21**(5): p. 390-402.

13. Allen, J.T. and R.J. Bettis. *Valid data abstraction from LDA measurements in two-phase propane releases*. in *Proceedings of the Seventh International Conference on Laser Anemometry- Advances and Applications*. 1997. Karlsruhe, Germany.

14. Bachalo, W.D., *Laser Doppler Velocimetry Primer.* 1985, National Aeronautics and Space Administration.

15. Roisman, I.V. and C. Tropea, *Flux measurements in sprays using phase Doppler techniques.* Atomization and Sprays, 2001. **11**(6): p. 667-699.

16. Tate, R.W. *Some problems associated with the accurate representation of droplet size distributions*. in *Proceedings of the Second International Conference on Liquid Atomization and Spray*. 1982.

17. Aguilar, G., et al., *Theoretical and experimental analysis of droplet diameter, temperature, and evaporation rate evolution in cryogenic sprays.* International Journal of Heat and Mass Transfer, 2001. **44**(17): p. 3201-3211.

18. Vu, H., O. García-Valladares, and G. Aguilar. *Insights Into Flashing Spray Characteristics Using a Capillary Tube Expansion Model*. in *20th Annual ILASS-Americas Conference*. 2007. Chicago, IL.

19. Fuchs, N.A., *The mechanics of aerosols*. Rev. and Enl. ed. 1964, New York, NY: Macmillan. 408.

20. Rudinger, G., *Effective Drag Coefficient for Gas-Particle Flow in Shock Tubes.* Journal of Basic Engineering, 1970. **92**(1): p. 165-172.

CHAPTER 3: Influence of a Coaxial Gas Flow on a Flashing Liquid Jet

Flashing may also be applied to flame spray pyrolysis (FSP) of ceria particles for catalysis of soot from diesel engines [1]. Traditional operation of the spray burner requires atomization of a liquid precursor jet by a coaxial gas flow that also functions as the oxidant and fuel. In this way, the atomization quality of the spray is coupled with the combustion characteristics, particularly flame length. This has made control of nanoparticle characteristics difficult as they are heavily dependent on both initial droplet size and flame residence time. Existing research of FSP by others is largely empirical and focused on precursor and fuel choices, flame characteristics and other combustion aspects [2].

The flashing mode of atomization may be introduced to the existing coaxial air-blast atomizer by pressurizing and heating the precursor liquid prior to injection. Under appropriate conditions, this may allow for independent control of oxidant/fuel gas flow rate without affecting atomization quality. The effects of the coaxial gas flow and presence of the flame are, however, unknown and must be deter-mined.

Desirable droplet characteristics for ceria formation are very small droplet diameters within a narrow, symmetric distribution to enable more complete combustion of the precursor and more uniform particle sizes. Existing air-blast atomizers will produce droplets in the 10 micron range with a high throughput. An alternative technique using electrosprays will produce more desirable nanosized droplets, but have much lower

throughput [3]. The incorporation of flashing phenomena to the air-blast atomizer may improve control of atomization and reduce droplet sizes while still maintaining high throughput, allowing for future scale-up of particle production.

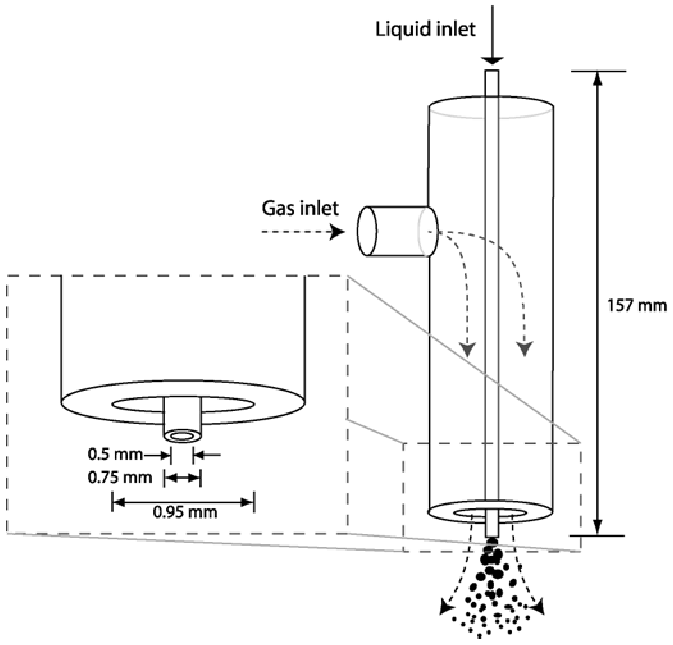

Figure 3.1: Spray burner geometry.

3.1 Materials and Methods

As depicted in Figure 3.1, a coaxial spray burner currently used in nanoparticle production is also used for this study. For safety reasons, water and helium are used as substitutes for the methanol precursor and hydrogen co-flow. Prior to its delivery to the spray burner, water is kept at saturation in a sealed, stainless steel storage cylinder and heated to initial storage temperatures (T_{st}) of 120-180 °C in 10°C increments using a band

Table 3.1: PDPA Settings.

PDPA hardware characteristics	
signal processor	FSA 3500
photo detector	PDM 1000
laser	Argon ion
Bragg cell frequency	40 MHz
wavelength	514.5, 488 nm
focal length of transmitting probe	250 mm
focal length of receiving probe	300 mm
laser power	150 mW
slit aperture	25 um
off-axis angle	30 degrees
diameter range	0.59-212.28 um
velocity range	0-235.53 m/s
beam waist	95.13 um
Run settings	
PMT	450 V
signal to noise ratio	med
coincidence mode	coincident
burst threshold	30 mV
band pass filter	5-40 MHz
down mix frequency	35 MHz
refractive index of particle	1.33
Intensity validation	
number of diameter bins	250
slope upper intensity curve	0.180 mV/um/um
lower to upper intensity curve ratio	0.1
upper intensity curve intercept	50.00 mV
lower intensity curve intercept	0.00 mV

heater. A type-K thermocouple, placed inside the cylinder, is attached to a feedback controller used to control the band heater power. Because this is a preliminary study, He co-flow is kept fixed at a flow rate of either 0 or 15 ml/min using a gas flow controller to observe the effects of a coaxial flow.

Because of the difficulty in measuring the total water flow rates for each given initial temperature, they are computed using an existing two-phase semi-empirical numerical model [4-6]. The one-dimensional model assumes separated flow, in which the liquid and gas velocities are treated independently. The model computes the internal flow properties along the inner tube of the spray burner by iteratively varying flow rate to satisfy the mass, momentum, energy, and entropy conservation equations. The model requires knowledge of void fraction and friction factor, determined from correlations by Rouhani and Axelsson [7], and Churchill [8] and Friedel [9], respectively. For the current study, the model is used to compute the total flow rate of water, and the liquid and gas phase velocities at the exit of the inner tube. This model has been validated and used by our group previously [10] and has been described in several publications noted above. The reader is referred to these for further details.

To characterize the external break up properties of the emerging jet, both high-speed video imaging and PDPA measurements are used. We use a high-speed Phantom camera (Vision Research Inc., Wayne, NJ) set at 13000 fps along with a Nikkor lens with +6 magnification lenses. The imaged area is backlit by a halogen lamp with diffuser. The PDPA system (TSI Inc., Shoreview, MN) is set to measure at the center of the external

flow, 15 mm from the spray burner tip. A minimum of 10000 validated signals are taken for each initial water temperature. PDPA settings are given in Table 3.1.

3.2 Results and Discussion

Table 3.2 provides the mass flow rates of water as well as exit void fraction and phase velocities computed by the numerical model. It is clear that increasing the initial storage temperature of the water can increase its flow rate significantly for a fixed nozzle geometry. This is an important consideration when weighing atomization quality versus FSP production rate.

Table 3.2: Precursor mass flow rate and tube exit flow parameters computed by numerical simulation.

T_{st} [°C]	mass flow rate [kg/h]	void fraction	liquid velocity [m/s]	gas velocity [m/s]
120	0.7672	0.88	9.12	78.60
130	0.8759	0.89	10.89	133.10
140	1.031	0.89	13.10	207.55
150	1.3027	0.90	16.72	302.04
160	1.6209	0.89	20.67	308.87
170	1.9825	0.89	25.01	302.57
180	2.3982	0.89	29.96	307.84

The high-speed video imaging reveals different modes of jet break up not previously observed in flashing studies. Figure 3.2 depicts a breakup sequence for water initially at 120 °C. Initially, the water emerges as an unbroken jet. Occasionally, however, a nucleated bubble within the jet will burst at some point downstream of the tube exit. This

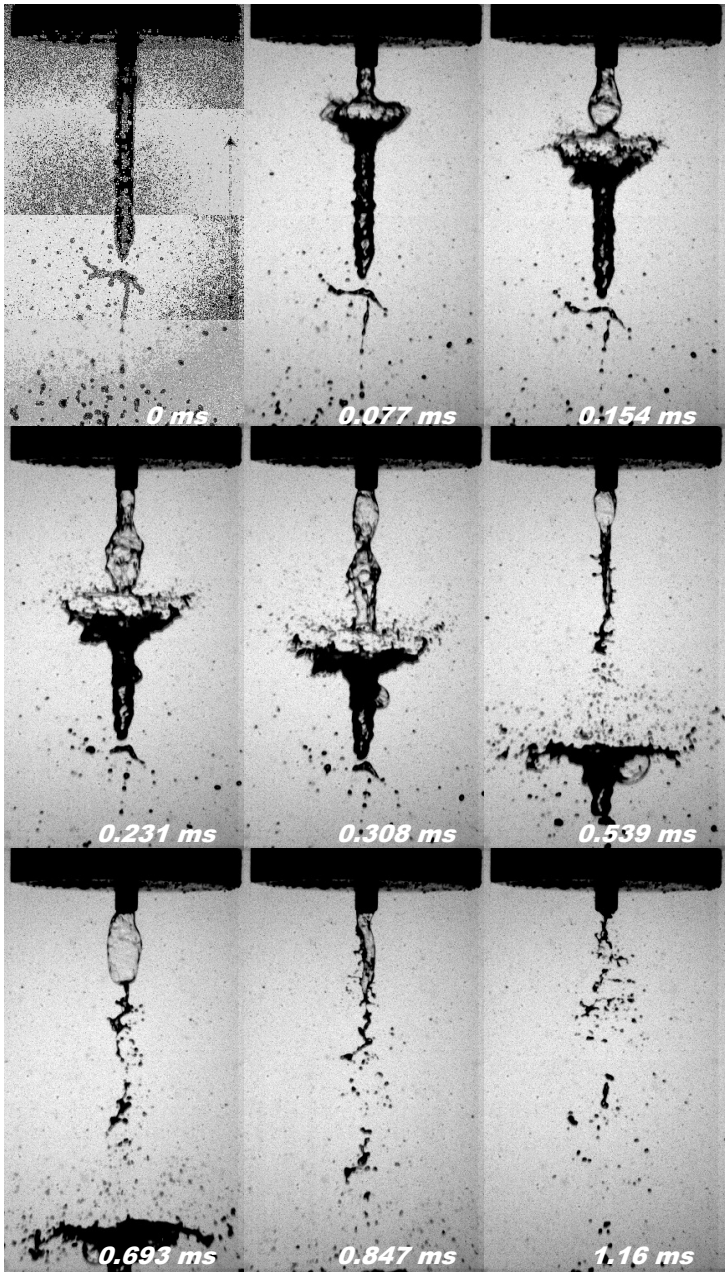

Figure 3.2: Flashing jet break up of water initially at 120 °C showing a main explosion followed by a wavy wake disintegration of the succeeding jet

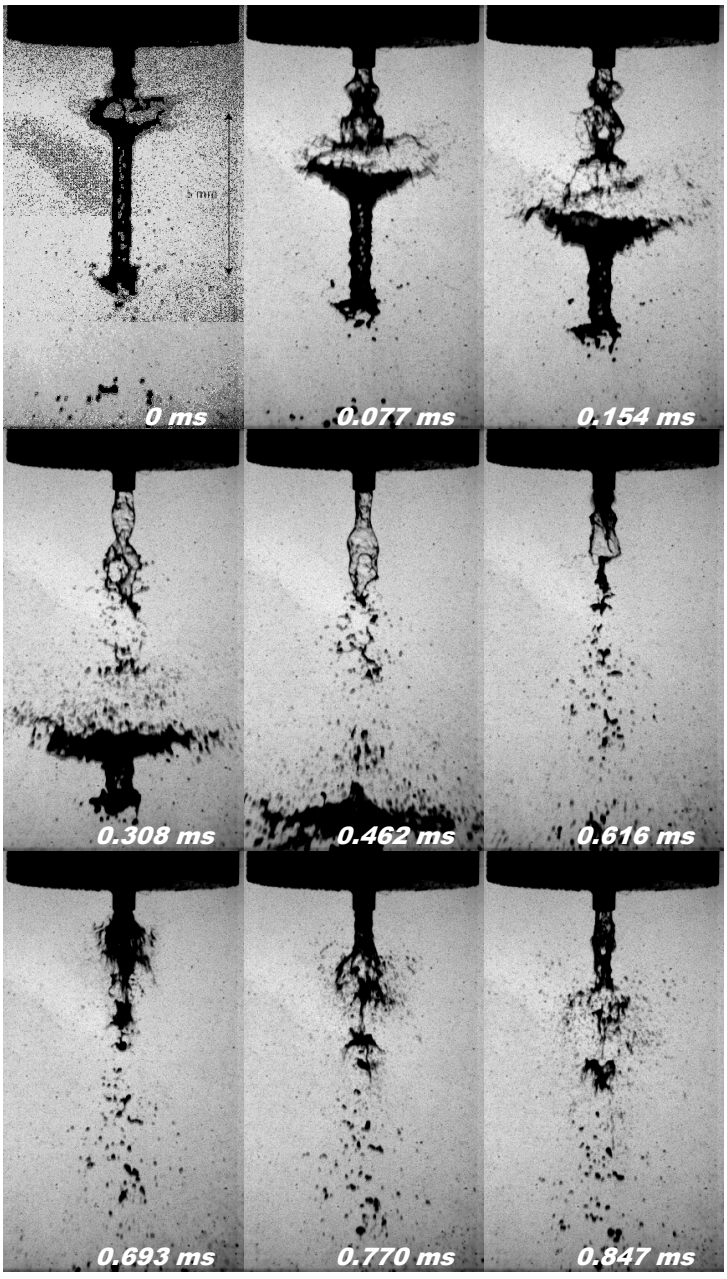

Figure 3.3: Flashing jet break up of water initially at 140 °C showing a main explosion followed by a partial wavy wake disintegration of the succeeding jet and secondary explosion.

causes the liquid to explode and disintegrate radially, while the jet below the expansion remains an intact slug. Occasionally, other bubbles appear to nucleate and expand within this slug, though further bulk disintegration by expansion is not observed within the field of view. Further breakup of the slug likely occurs by aerodynamic forces further downstream. Above the point of main explosion, a wake is created which greatly affects the succeeding flow. A wave with characteristic wavelength and amplitude grows and persists for typically two to three cycles. As each cycle collapses, it will disintegrate into droplets with the same axial velocity as the unbroken jet. Unlike droplets formed by the main explosion, they have nearly zero radial velocity. In some instances, following the break up sequence, an extended period may exist in which only water vapor emerges from the tube.

As the water temperature is increased, the frequency of the break up sequences increases. Several main explosions may occur in succession, preventing the formation of wave break up. At 140 °C (Figure 3.3), a transition is observed in which the main explosion may be followed by a smaller explosion of lower intensity that occurs within the wake.

Increasing the temperature to 150 °C (Figure 3.4) results in nearly continuous break up, such that an unbroken jet rarely exists. Primary and secondary explosions occur with high frequency and intensity. Additionally, “flare flashing” may occur, as identified by Peter et al., in which a finely atomized spray exits at the tube exit. The unbroken slug identified for 120 °C no longer exits. Increasing the temperatures beyond 150 °C causes the flare

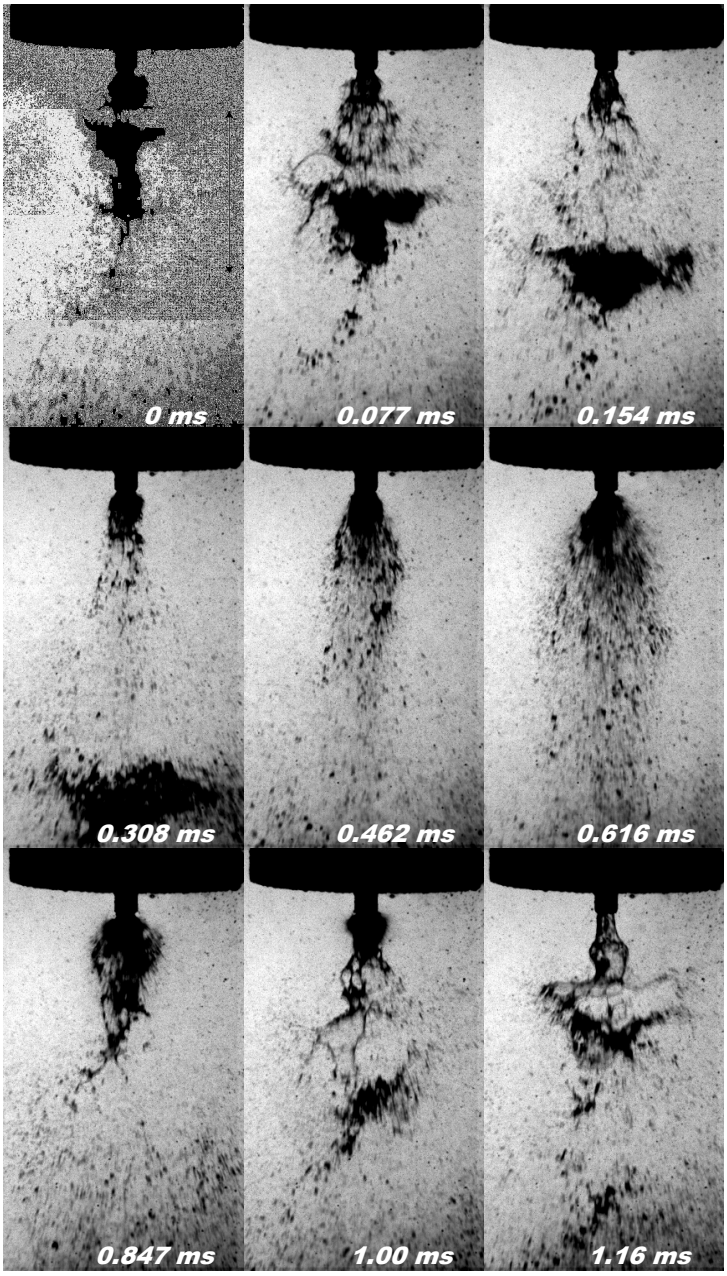

Figure 3.4: Flashing jet break up of water initially at 150 °C showing intermittent external explosions with flare flashing.

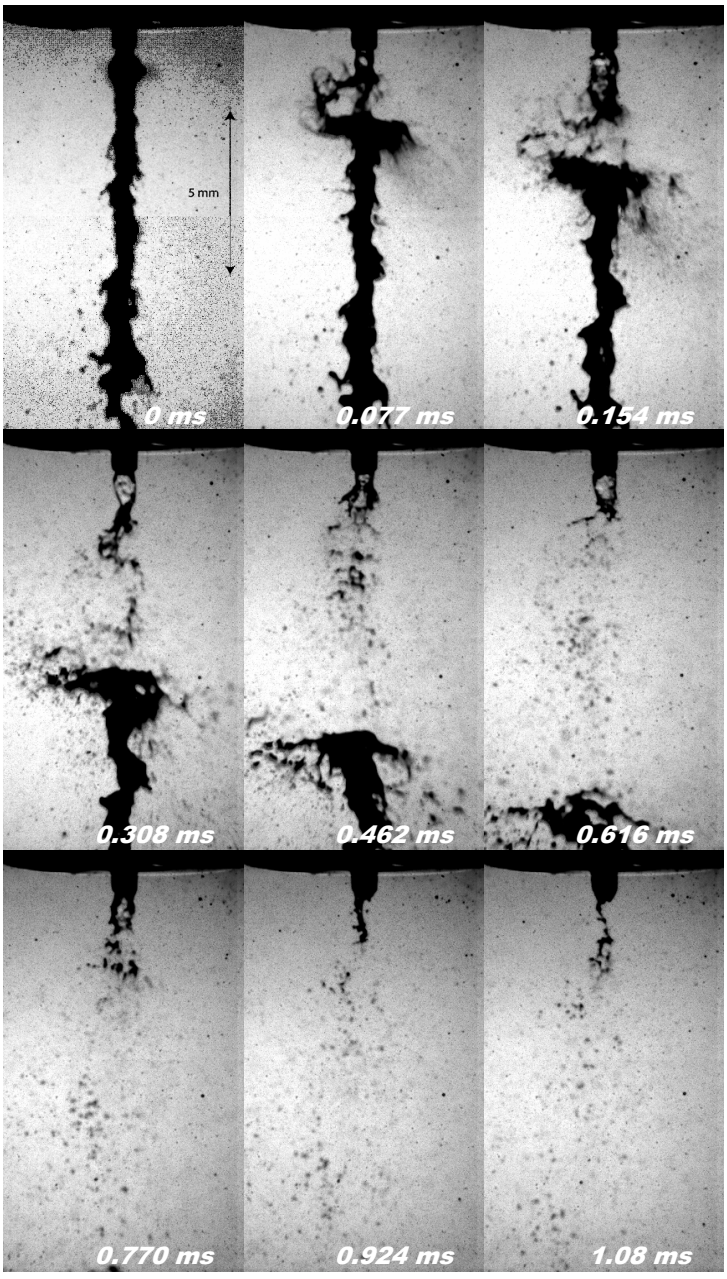

Figure 3.5: Flashing jet break up of water initially at 120 °C showing a main explosion followed by a wavy wake disintegration of the succeeding jet

flashing break up mode to occur continuously but with pulsating intensity. By 170-180 °C, stable flare flashing is achieved. These latter scenarios are not shown for brevity.

Figure 3.5 illustrates the effect of the addition of coaxial He gas on a 120 °C water jet. Strong wind shear is evident on the unbroken jet, resulting in some first-wind induced breakup. Primary explosions occur as without the coaxial flow, but with resulting droplets being accelerated by the gas flow. The succeeding wake is now strongly subjected to wind shear and breaks up more finely than before. The effects are analogous for higher temperatures. However, after initiation of flare flashing at 150-160 °C, the coaxial flow appears to have little effect aside from acceleration the droplet velocities. These latter scenarios are, again, not shown for brevity.

Quantitative droplet characteristics are provided by PDPA measurements. Velocity histograms and diameter vs. velocity plots are provided in Figures 3.6 and 3.7 for flash only and flash and coaxial flow, respectively. A bimodal distribution of velocity is observable in flash only at 120 and 140 °C. This may be attributed to the explosive and wavy modes of break up observed in the imaging. The higher velocity mode may represent the explosive break up due to the acceleration from explosion. As temperatures increase and the flow transitions to more uniform breakup characteristics, the bimodality disappears. Diameter distributions show that droplet sizes de-crease significantly with increasing temperature. Droplets also shift to higher velocities and the overall velocity distribution widens. With the coaxial He flow, the velocity histograms show bimodality throughout the temperature range of the study. The higher velocity mode may be

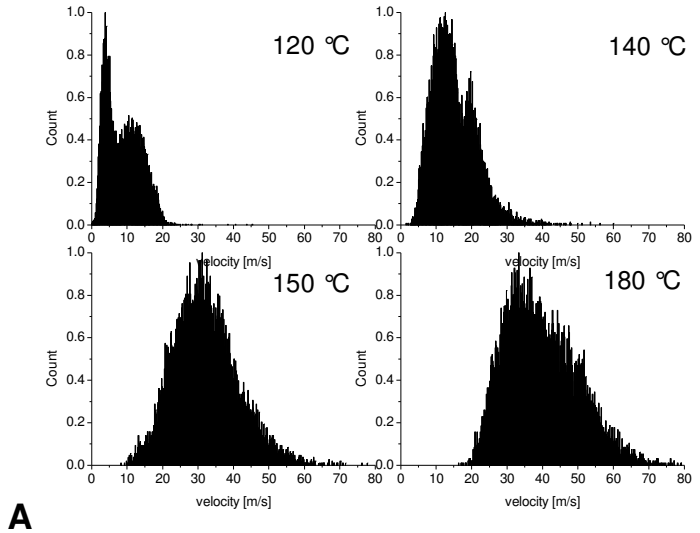

A

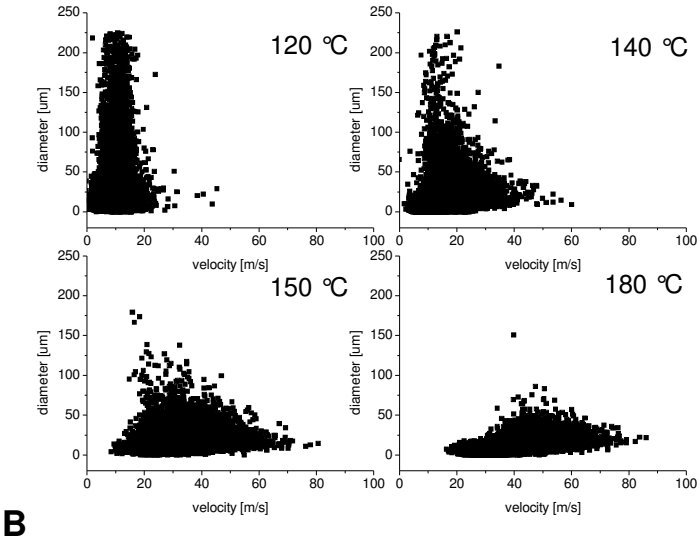

B

Figure 3.6: PDPA measured (**A**) velocity histograms and (**B**) diameter vs. velocity distributions without coaxial gas flow.

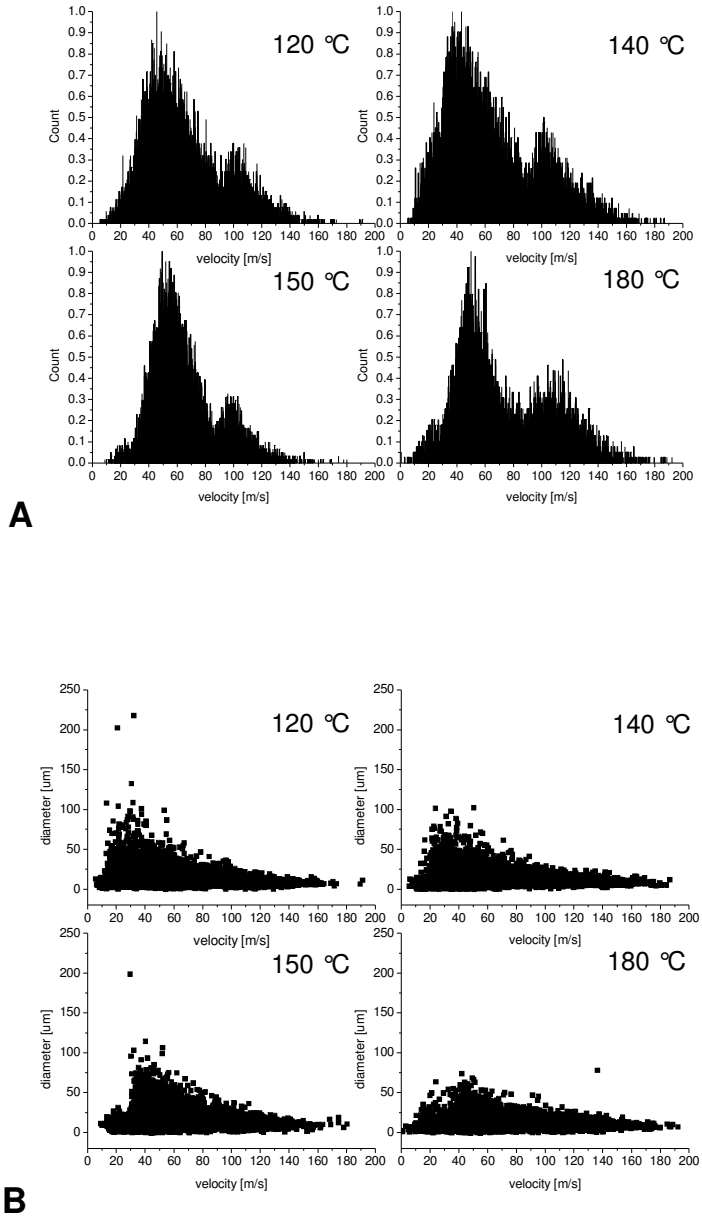

Figure 3.7: PDPA measured (**A**) velocity histograms and (**B**) diameter vs. velocity distributions with coaxial gas flow.

attributed to acceleration from the coaxial flow. The velocity appears to shift to higher values with increasing temperature, though relative distribution remains fairly constant. Diameter vs. velocity plots also show a wide spread in velocity with little change in distribution.

D_{10} and D_{32} averages and mean velocities are shown in Figure 3.8. Interestingly, the average droplet sizes achievable at low superheat with coaxial flow are nearly the same as that for high superheat. There is also a trend of increasing droplet size within the temperature range of 140-160 °C. Since the coaxial gas flow rate is kept constant as the liquid flow rate increases, atomization by wind shearing becomes less important as superheat increases. Therefore, droplet sizes tend to revert back to those without coaxial flow. This trend may be demonstrated by plotting momentum flux ratio vs. T_{st} as shown in Figure 3.9.

3.3 Conclusions

Flash atomization was introduced into an existing spray burner used for flame spray pyrolysis to observe the atomization phenomena and influence of a coaxial gas flow. Different modes of flashing breakup (primary and secondary explosive and wavy) were identified that have not previously been observed. Through numerical modeling, the mass flow rate was found to increase significantly with increasing initial temperature. The addition of a coaxial flow tends to destabilize the liquid jet by wind shear and accelerate the formed droplets. Droplet sizes decreased significantly with coaxial flow for lower

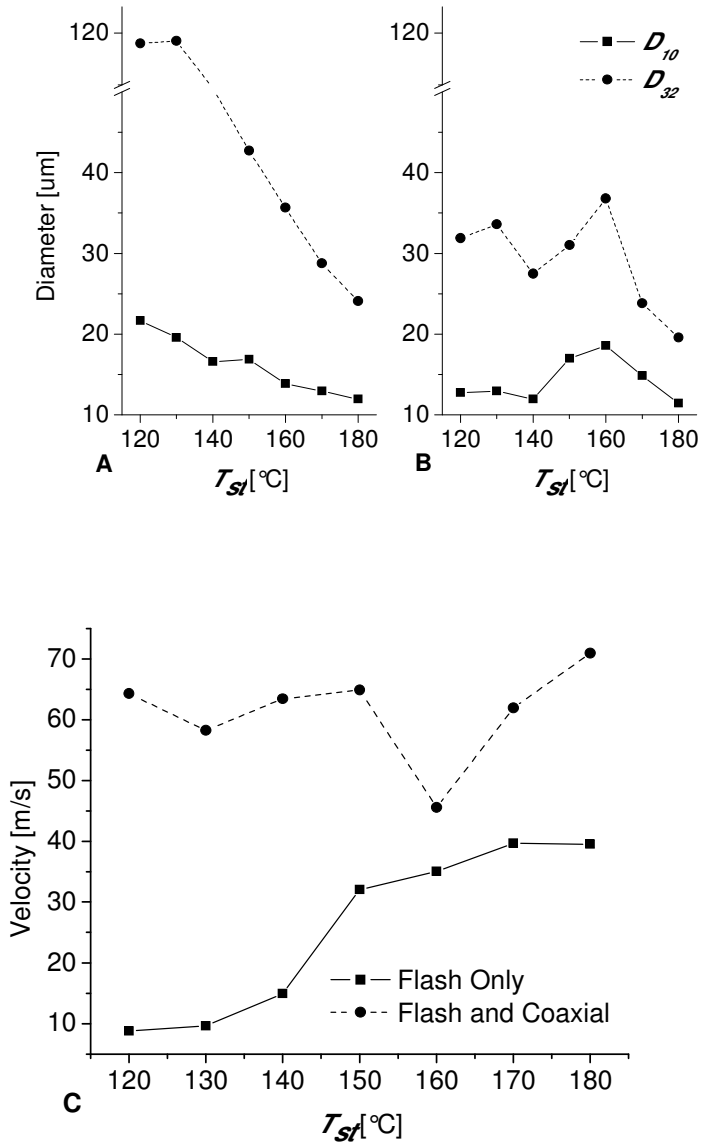

Figure 3.8. PDPA measured (**A**) average diameter without coaxial flow, (**B**) average diameter with coaxial flow, and (**C**) average velocity.

superheats. However, as super heat increased, droplet sizes reverted back to flash-only values due to the decreasing momentum flux ratio between the gas and liquid streams. Bimodal distributions were observed in PDPA measurements and were attributed to multimodal flashing breakup and acceleration due to the coaxial gas flow. Future studies are needed to modify the mass flow rate of the liquid precursor by changing the inner tube diameter and determine if higher momentum flux ratios will further decrease droplet sizes for high superheat cases.

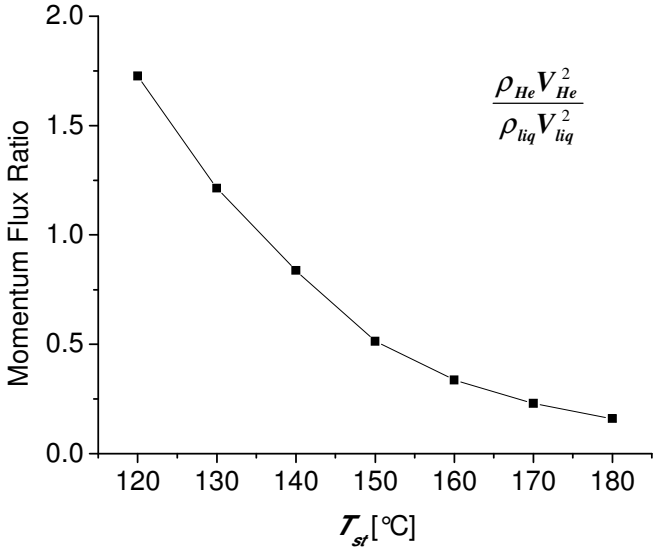

Figure 3.9. Momentum flux ratio of coaxial gas to liquid vs. initial liquid storage temperature.

References

1. Madler, L., W.J. Stark, and S.E. Pratsinis, *Flame-made ceria nanoparticles.* Journal of Materials Research, 2002. **17**(6): p. 1356-1362.
2. Kammler, H.K., L. Madler, and S.E. Pratsinis, *Flame synthesis of nanoparticles.* Chemical Engineering & Technology, 2001. **24**(6): p. 583-596.
3. Lenggoro, I.W., et al., *Colloidal nanoparticle analysis by nanoelectrospray size spectrometry with a heated flow.* Analytica Chimica Acta, 2007. **585**: p. 193-201.
4. Escanes, F., C.D. Perez-Segarra, and A. Oliva, *Numerical-Simulation of Capillary-Tube Expansion Devices.* International Journal of Refrigeration-Revue Internationale Du Froid, 1995. **18**(2): p. 113-122.
5. García-Valladares, O., D.C. Perez-Segarra, and A. Oliva, *Numerical simulation of capillary tube expansion devices behaviour with pure and mixed refrigerants considering metastable region. Part I: mathematical formulation and numerical model.* Applied Thermal Engineering, 2002. **22**(2): p. 173-182.
6. García-Valladares, O., *Review of numerical simulation of capillary tube using refrigerant mixtures.* Applied Thermal Engineering, 2004. **24**(7): p. 949-966.
7. Rouhani, S.Z. and E. Axelsson, *Calculation of Void Volume Fraction in Subcooled and Quality Boiling Regions.* International Journal of Heat and Mass Transfer, 1970. **13**(2): p. 383-393.
8. Churchill, S.W., *Friction-Factor Equation Spans All Fluid-Flow Regimes.* Chemical Engineering, 1977. **84**(24): p. 91-92.

9. Friedel, L. *Improved friction pressure drop correlation for horizontal and vertical two-phase pipe flow*. in *European Two-Phase Flow Group Meeting*. 1979. Ispra, Italy.

10. Vu, H., O. García-Valladares, and G. Aguilar, *Vapor/Liquid Phase Interaction in Flare Flashing Sprays Used in Dermatologic Cooling*. International Journal of Heat and Mass Transfer, 2008. **51**: p. 5721-5731.

CHAPTER 4: High-Speed Internal Nozzle Flow Visualization of Flashing Jets

In Chapter 3, new flashing atomization modes were discovered that were previously unknown. Through combined high-speed video imaging and phase Doppler optical measurements of droplet characteristics, it was found that at lower superheats and large *L/D* aspect ratios, jet breakup may occur by way of discrete bubble explosions with ballooning and disintegration. These modes were believed to arise due to internal slug flow within the nozzle from bubble merging. Characteristic frequencies in explosive bubble breakup were observed and increased with increasing initial liquid superheat, although the reasons for this are still unknown. With sufficient superheat, flashing moves into a regime of flaring in which an annular flow is believed to be established and fine atomization is ob-served immediately at the nozzle exit.

This study expands on existing knowledge of flashing breakup mechanisms by employing high-speed video imaging of the internal flow and time-dependent flow phenomena, and corroborates explanations of the new breakup modes found previously.

4.1 Materials and Methods

Internal flow is visualized using transparent glass tubes with internal diameters of 0.6 and 1.2 mm and corresponding lengths of 80 and 270 mm. Water is used as the working fluid

and flashing is induced by heating and pressurization within a stainless steel cylinder at saturation conditions to temperatures ranging from 105-180 ˚C. A schematic of the experimental setup is given in Figure 4.1. The cylinder is heated using a band heater, controlled by feedback from a thermocouple in direct contact with the water. The water is introduced to the glass tubes through a ¼" ball valve to minimize flow disturbances which is then attached to the nozzle using a custom-made adaptor. The nozzle is pressed against the adaptor using a retaining arm and sealed with a high temperature o-ring. Imaging is performed using a Phantom v7.1 camera at 25000 fps and is backlit with a high-intensity tungsten lamp. Because of the limited field of view of the camera, flow through the entire nozzle could be captured by scanning the camera along the nozzle length using an electronic translational stage. However, nucleation generally only occurs very near the nozzle exit, so the camera is kept in this position. Additional ¼" fittings are used as necessary to adjust the nozzle orientation with respect to gravity while keeping the storage cylinder fixed. Because the end plate of the retaining arm affected the resulting spray characteristics external spray characteristics are imaged separately using stainless steel tube nozzles of 0.51 and 1.2 mm ID and 80 and 130 mm lengths, respectively.

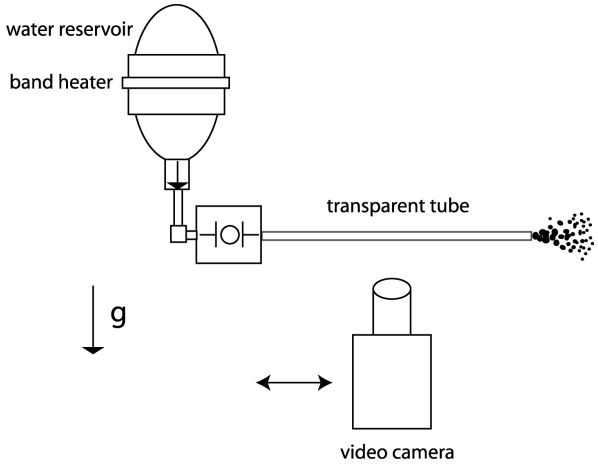

Figure 4.1: Experimental setup for internal flow visualization.

4.2 Results

Several flow regimes are observable within the experimental parameters tested and are depicted in Figure 4.2. Bubbly flow occurs when bubbles form and predominantly reach an equilibrium diameter less than the nozzle width. This transitions to slug flow when the bubbles expand to the nozzle width and continue expansion by lengthening and merging with other bubbles. Slugs may become unstable when the trailing gas-liquid interface trips and becomes unstable, leading to a chaotic mixing of phases that spreads throughout the slug. Often, however, bubble nucleation sites do not become active and phase change only occurs very near the nozzle exit where pressure has undoubtedly dropped significantly. This phenomenon is denoted here as tip evaporation.

Figure 4.2: Flow regimes observed in the present study: (a) bubbly, (b) slug, (c) churn, and (d) tip evaporation.

Figure 4.3 is a regime map of the dominant regimes observed for each tested condition. When more than one regime is prevalent for a given condition, both regimes are noted. Due to leakage from the nozzle entrance junction, tests could not be performed above 180 ˚C for the 0.6 mm nozzle and above 160 ˚C for the 1.2 mm nozzle. The locations of nucleation sites may change sporadically, but generally reside near the nozzle exit. With the 0.6 mm nozzle, significant superheat, with respect to atmospheric conditions, is required to initiate nucleation. This is likely due to a wall confinement effect that resists bubble growth. As the nozzle rotates to point vertically upward, the frequency of slug formation decreases at 90˚ and is virtually eliminated at 180˚. In fact, at 180˚ the internal

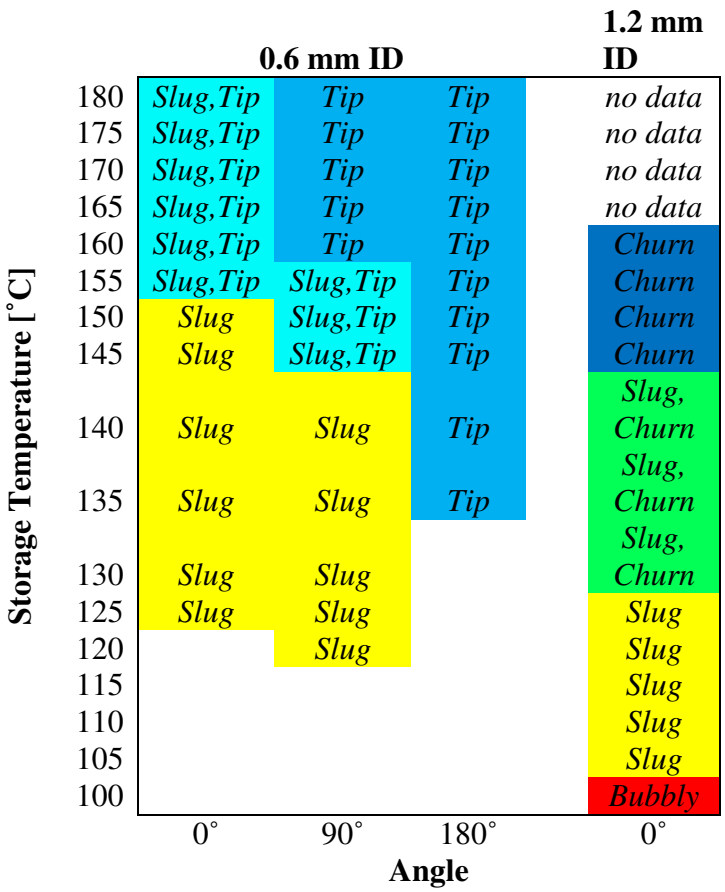

Figure 4.3: Flow regime map for tested conditions. Angles are in respect to gravity. Regimes indicated are the most dominant for the given conditions.

flow only exhibits tip evaporation. Buoyancy, therefore, likely affects nucleation site activation. With the larger 1.2 mm nozzle, nucleation occurs at a much lower temperature with the bubbly flow regime. This transitions to slug flow, and as flow velocities continue to increase with increasing temperature and pressure, the slugs destabilize to churn flow.

The external breakup phenomena with stainless steel nozzles can generally be correlated to the observed internal flow. Generally, flashing jet break up occurs when some of the liquid phase boils to gas and expands violently, causing the surrounding liquid to break

up into droplets. For long nozzles with high *L/D* ratios, as is the case for this study, the boiling initiates within the nozzle and the external break up characteristics depend on the internal flow regime and the remaining energy of expansion of the gas upon exiting. For the vertically downward facing nozzles, complex breakup mechanisms were observed as described by Vu et al. [13]. Figure 4.4 shows a breakup sequence in which a slug breeches the nozzle exit with the balloon formation and collapse that ensues. This sequence would appear to occur with slugs that have nucleated further upstream and have lost most of their expansion energy within the nozzle. With slugs that nucleate near the nozzle tip, the expansion energy causes an explosive breakup and fine atomization termed "flaring", as shown in Figure 4.5a. This flaring is intermittent and separated by periods of unbroken jet. As tip evaporation manifests at higher temperatures, flaring becomes steady. With the nozzle at 90˚, the frequency of nucleation and slug formation decreases significantly. As tip evaporation emerges, the external flow transitions to a steady spray. With the nozzle at 180˚, a steady breakup process occurs in which bubble nucleation and explosion appear to occur externally just beyond the nozzle exit (Figure 4.5b). With increasing temperature, this transitions to a flaring breakup (Figure 4.5c). The larger 1.2 mm nozzle at 0˚ and low superheat exhibits complex breakup phenomena very similar to that for the 0.6 mm nozzle. The onset of churn flow causes a very violent break up resulting in a dense spray which may also be qualitatively called flaring (Figure 4.5d).

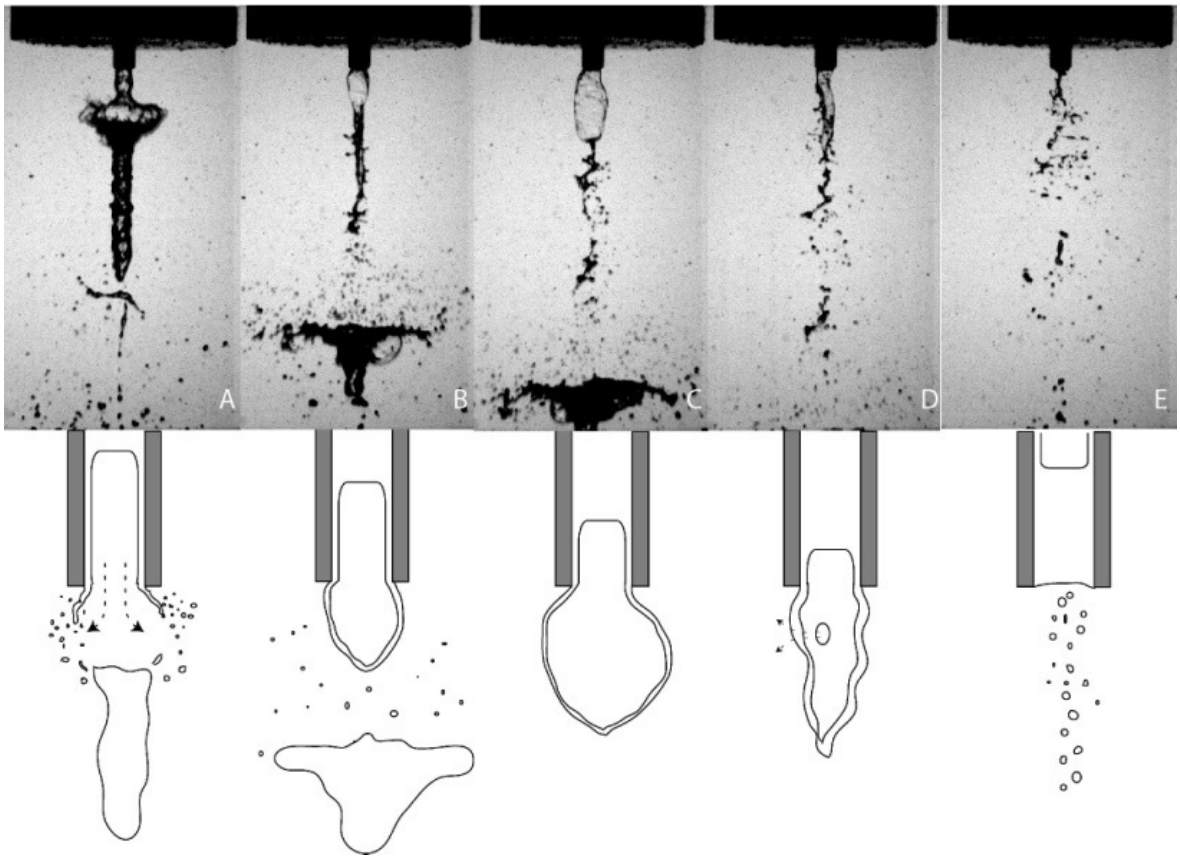

Figure 4.4: Breakup modes for highly expanded slugs with accompanying illustrative diagrams.

4.3 Conclusions

This paper characterizes, through high-speed video imaging, the internal flow characteristics of flashing of initially saturated water within straight tube glass nozzles in order to explain external breakup modes. Complicated breakup modes are observed for downward facing nozzles because of the irregularity of nucleation sites and varying degrees of expansion of gas slugs within the nozzle. Bubble nucleation begins at a much lower temperature for the larger diameter nozzle and also displays churn flow patterns at

higher temperatures. Gravity, when acting in the same direction as flow velocity seems to promote nucleation site activation. Horizontally and vertically upward facing nozzles exhibited far fewer nucleation events. Tip evaporation was the predominant internal regime for the latter cases, producing a generally stable external breakup.

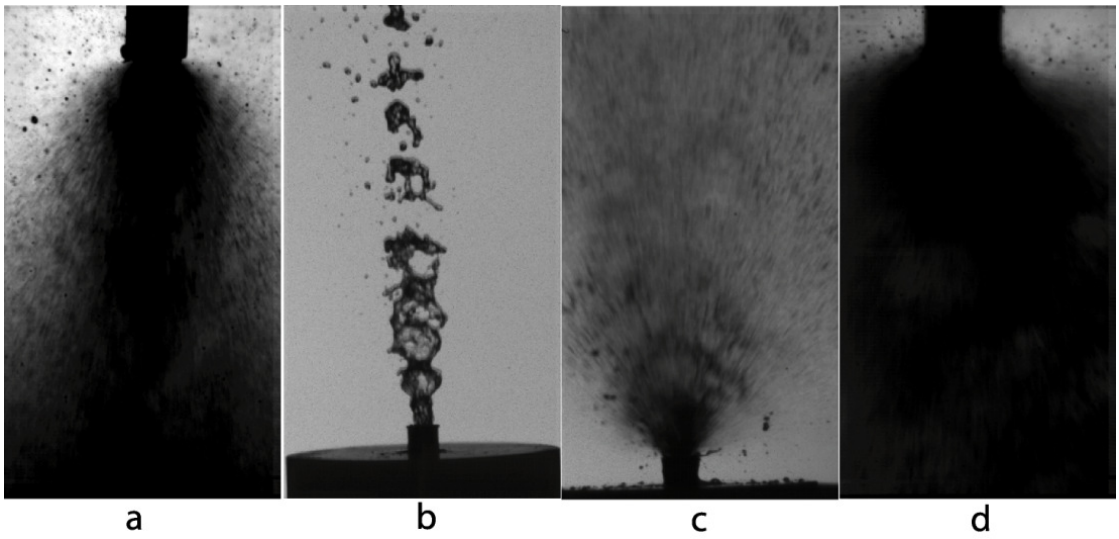

Figure 4.5: Examples of other external breakup modes: (a) flaring from a 0.5 mm ID nozzle at 0˚, (b) steady breakup from tip evaporation in a 0.5 mm ID nozzle at 180˚ and (c) transition to flaring, (d) very dense flaring spray resulting from churn flow in a 1.2 mm ID nozzle at 0˚.

References

1. Brown, R. and J.L. York, *Sprays Formed by Flashing Liquid Jets.* Aiche Journal, 1962. **8**(2): p. 149-153.
2. Peter, E.M., A. Takimoto, and Y. Hayashi, *Flashing and Shattering Phenomena of Superheated Liquid Jets.* Jsme International Journal Series B-Fluids and Thermal Engineering, 1994. **37**(2): p. 313-321.
3. Reitz, R.D., *A Photographic Study of Flash-Boiling Atomization.* Aerosol Science and Technology, 1990. **12**(3): p. 561-569.
4. Park, B.S. and S.Y. Lee, *An Experimental Investigation of the Flash Atomization Mechanism.* Atomization and Sprays, 1994. **4**(2): p. 159-179.
5. Kitamura, Y., H. Morimitsu, and T. Takahashi, *Critical Superheat for Flashing of Superheated Liquid Jets.* Industrial & Engineering Chemistry Fundamentals, 1986. **25**(2): p. 206-211.
6. Sher, E. and C. Elata, *Spray Formation from Pressure Cans by Flashing.* Industrial & Engineering Chemistry Process Design and Development, 1977. **16**(2): p. 237-242.
7. Sher, E. and M. ZeigersonKatz, *Spray formation by flashing of a binary mixture: An energy balance approach.* Atomization and Sprays, 1996. **6**(4): p. 447-459.
8. Zeng, Y.B. and C.F.F. Lee, *An atomization model for flash boiling sprays.* Combustion Science and Technology, 2001. **169**: p. 45-67.

9. Allen, J.T., *Laser-based measurements in two-phase flashing propane jets. Part one: velocity profiles.* Journal of Loss Prevention in the Process Industries, 1998. **11**(5): p. 291-297.

10. Allen, J.T., *Laser-based measurements in two-phase flashing propane jets. Part two: droplet size distribution.* Journal of Loss Prevention in the Process Industries, 1998. **11**(5): p. 299-306.

11. Knubben, G. and C.W.M. van der Geld, *Drop size distribution evolution after continuous or intermittent injection of butane or propane in a confined air flow.* Applied Thermal Engineering, 2001. **21**(7): p. 787-811.

12. Vu, H., O. García-Valladares, and G. Aguilar, *Vapor/Liquid Phase Interaction in Flare Flashing Sprays Used in Dermatologic Cooling.* International Journal of Heat and Mass Transfer, 2008. **51**: p. 5721-5731.

13. Vu, H., et al. *Influence of a coaxial gas flow on a flashing liquid jet: implications for flame spray synthesis of nanoparticles*. in *21st Annual Conference on Liquid Atomization and Spray Systems*. 2008. Orlando, FL.

14. Nelson, J.S., et al., *Dynamic Epidermal Cooling During Pulsed-Laser Treatment of Port-Wine Stain - a New Methodology with Preliminary Clinical-Evaluation.* Archives of Dermatology, 1995. **131**(6): p. 695-700.

15. Aguilar, G., et al., *Theoretical and experimental analysis of droplet diameter, temperature, and evaporation rate evolution in cryogenic sprays.* International Journal of Heat and Mass Transfer, 2001. **44**(17): p. 3201-3211.

16. Hsieh, S.S. and H.H. Tsai, *Thermal and flow measurements of continuous cryogenic spray cooling.* Archives of Dermatological Research, 2006. **298**(2): p. 82-95.

17. Senda, J., et al., *Characteristics of Spray Injected from Gasoline Injector.* Jsme International Journal Series B-Fluids and Thermal Engineering, 1994. **37**(4): p. 931-936.

18. Nishimura, Y., et al. *An experimental study on flash boiling spray using two-component fuel under the condition of advanced injection HCCI.* in *10th International Conference on Liquid Atomization and Spray Systems*. 2006. Kyoto, Japan.

19. Bowen, P.J. and L.C. Shirvill, *Combustion Hazards Posed by the Pressurized Atomization of High-Flashpoint Liquids.* Journal of Loss Prevention in the Process Industries, 1994. **7**(3): p. 233-241.

20. Johnson, D.W. and J.L. Woodward, *Release: a model with data to predict aerosol rainout in accidental releases*. 1999, New York: American Institute of Chemical Engineers. 184.

CHAPTER 5: Fluid and Thermal Dynamics of Cryogen Sprays Impinging on a Human Tissue Phantom

Cryogen spray cooling (CSC) protects the epidermis from unintended heating during cutaneous laser surgery. The present work investigated the time-dependent flow characteristics of cryogen sprays and correspondent thermal dynamics at the surface of a human tissue phantom. First, a numerical analysis was carried out to evaluate an epoxy block substrate as a human tissue phantom. Next, the velocity and diameter of cryogen droplets were measured simultaneously and correlated with surface temperature of the human tissue phantom during CSC. Finally, velocity and diameter measurements were used to compute the spray number, mass and kinetic energy fluxes, and temperature measurements were used to compute the surface heat flux. Numerical modeling showed that the thermal response of our phantom was qualitatively similar to that of human stratum corneum and epidermis; quantitatively, thermal responses differed. A simple transformation to map the temperature response of the phantom to that of tissue was derived. Despite the relatively short spurt durations (10, 30 and 50 ms), cryogen delivery is mostly a steady state process with initial and final fluid transients mainly due to the valve dynamics. Thermal transients (16 ms) are longer than fluid transients (4 ms) due to the low thermal diffusivity of human tissues; steady states are comparable in duration (10, 30 and 50 ms) although there is an inherent thermal delay ($\approx$12 ms). Steady-state temperatures are the lowest surface temperatures experienced by the

substrate, independent of spurt duration; hence, longer spurt durations result in larger exposures of the tissue surface to the same lower, steady state temperature as in shorter spurts. Temperatures in human tissue during CSC for the spray system and parameters used herein are estimated to be ≈-19 ˚C at the stratum corneum surface and > 0 ˚C across the epidermis.

Nomenclature

A_γ	reference area of PDPA detection volume
CSC	cryogen spray cooling
c	specific heat
D	droplet diameter
e_γ	unit vector
h	heat transfer coefficient
k	thermal conductivity
L	characteristic length
M	sample size or number of PDPA measurements
N	number of validated PDPA signals
n	normal unit vector
PDPA	phase Doppler particle analyzer
q''	surface heat flux
T	experimental temperature
t	time
V	droplet velocity
x	lateral coordinate
y	depth coordinate

subscripts

b	boiling
e	epoxy
f	final
h	highest
I	total number of PDPA measurements
i	PDPA measurement
J	total number of temperature measurements

j	temperature measurement
l	lowest
o	initial
p	tissue phantom
s	phantom surface
t	tissue

Greek symbols

α	thermal diffusivity
γ	particle trajectory angle
η	PDPA count correction factor
θ	numerical temperature
ξ	transformation coefficient
ρ	density
τ	measurement time
φ	spray flux

5.1 Introduction

Cryogen spray cooling (CSC) has proven essential for successful cutaneous laser surgery without adverse effects. A short cryogen spurt precools the epidermis during laser irradiation to avoid unintended injury therein from excessive heating induced by melanin absorption [1, 2]. Heat extraction from tissue during CSC is a function of many fundamental spray parameters, such as average droplet velocity and diameter, mass flow rate, temperature and spray density [3-7], that vary in time and space within the spray cone. There are many experimental and numerical studies that describe the thermal dynamics imposed by CSC on tissue models. However, only a few studies considered the spray characteristic structure in steady state, namely droplet velocity and diameter distributions. Karapetian et al. [4] reported droplet velocity and diameter ranges from 28–72 m/s and 12–18 μm, respectively, for inner nozzle diameters from 0.57–1.33 mm

and two lengths, 8 and 65 mm. It was concluded that changes in mass flow rate have a larger effect on the surface heat flux than changes in droplet size, and that for fully atomized sprays changes in velocity can substantially impact the surface heat flux. Pikkula et al. [5] reported that sprays with a higher Weber number (ratio of inertial forces to surface tension) increase heat removal; i.e., higher velocities and larger droplets enhance surface heat transfer. Hsieh and Tsai [8] also studied the effect of spray characteristics and mass flow on the surface heat flux using small nozzle diameters, 0.2–0.4 mm, at different nozzle-substrate distances. The authors proposed that nozzles with smaller diameters than those in current use may enhance surface cooling. While these experimental studies describe the thermal dynamics imposed by CSC on tissue models, they all consider the spray characteristic structure in steady state only. To the best of our knowledge, this is the first study correlating spray droplets dynamics (average velocity and diameter) and surface thermal dynamics (temperature and heat flux) during CSC of human tissue. A better understanding of CSC dynamics is essential for optimizing laser procedures, improving current technologies and providing insights into biophysical responses. For example, different studies have investigated multiple-intermittent cryogen spurts and laser pulses to improve cutaneous laser surgery [9-11]. Characterization of the spray system dynamics is fundamental to develop this technology. It is important to acknowledge the significant work of a large community devoted to liquid atomization and sprays, where related problems have been addressed and some of the analytical tools used herein have been developed. The main

differences between previous work and our intended application to human tissue are the low thermal diffusivity of the substrate and the short spurt durations.

5.2 Objectives

The objectives of the present study are (i) to evaluate an epoxy block substrate as a thermal model of human tissues, namely stratum corneum and epidermis; (ii) determine the flow characteristics of cryogen sprays in steady and transient states impinging onto the human tissue phantom; (iii) correlate the spray characteristics to the surface heat transferred from the human tissue phantom; and (iv) provide an estimate of the temperatures to be expected in human skin. Spray transient state refers to the period when average droplet velocity and diameter vary over time. Initial and final transients occur when the spray valve opens and closes, respectively.

5.3 Experimental and Numerical Methods

5.3.1 Spray System

Refrigerant hydrofluorocarbon 134a was delivered through a high pressure hose to an electronic valve attached to an angled-tube nozzle (120˚) with a length and inner diameter of 40 mm and 0.5 mm, respectively. The valve and nozzle were from a commercial skin cooling device (GentleLase, Candela, Wayland MA). The spray system was set to deliver a downward vertical spray. R134a (boiling temperature at

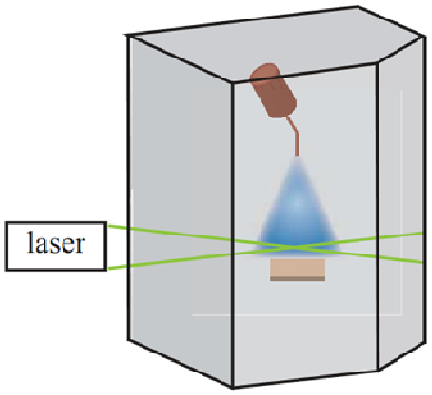

(a) Experimental Set

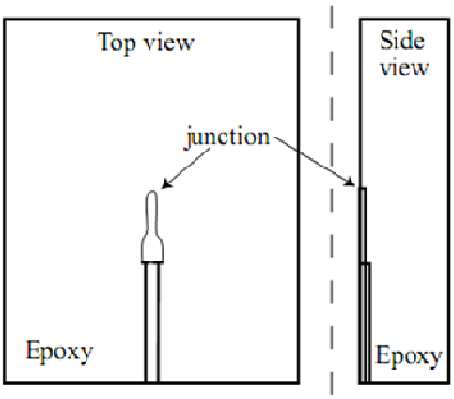

(b) Tissue phantom.

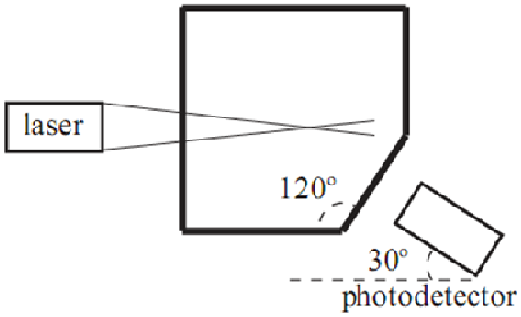

(c) Chamber and PDPA components (top view).

Figure 5.1: Schematic of tight-seal acrylic chamber, spray system, tissue phantom, and PDPA components. (a) Spray system and tissue phantom were placed inside to conduct experiments at reduced, constant relative humidity levels (16-18%). (b) A thin film thermocouple embedded in epoxy was used to measure surface temperatures. (c) Chamber walls were designed to be perpendicular to PDPA components to minimize refraction.

atmospheric pressure ≈-26 ˚C) was kept in its original container at 600 kPa and 21 ˚C. Spurt durations of 10, 30 and 50 ms were investigated. A schematic of the spray system is shown in Figure 5.1a.

5.3.2 Phase Doppler Anemometry and Particle Sizing

Spray droplet velocity and diameter were measured with a Phase Doppler Particle Analyzer (PDPA; TSI Incorporated, Shoreview MN). Although this system was capable of measuring velocity along two perpendicular axes, only axial velocities were considered because measurements correspond to the cone center of vertical cryogen sprays. The nozzle-to-phantom distance was 35 mm and the PDPA measurement volume was set 2.5 mm above the human tissue phantom; i.e., 32.5 mm away from the nozzle tip. For the analysis of droplet dynamics, velocity and diameter measurements were split in 1 ms time windows. Approximately 10 experiments were conducted for each spurt duration under study to obtain a minimum of 100 data points in each time bin. The deviation percentage from the cumulative size distribution as a function of the sample size M can be estimated as $127.32 \cdot M^{-0.492}$ [12], which corresponds to a maximum deviation of 13% in our study.

5.3.3 Human Tissue Phantom and Thermal Sensor

The human tissue phantom and thermal sensor consisted of an epoxy resin (EP30-3, Master Bond, Inc., Hackensack NJ) with a thin-foil thermocouple (CO2-K, Omega

Table 5.1: Thermal properties of tissue with 0.2 and 0.6 g of water per g of total tissue [13] and epoxy [14].

	tissue (0.3 water content)	tissue (0.6 water content)	epoxy
k (W/m K)	0.13	0.34	0.14
ρ (kg/m^3)	1210	1120	1019
c (J/kg K)	2241	3200	1631
α (m^2/s)	4.7×10^{-8}	9.5×10^{-8}	$8.4 \times 10^{-}$

Engineering, Stamford CT) embedded at the surface, as shown schematically in Figure 5.1b. Although the width and length of the thermocouple measurement junction are ~0.5 mm, the thin-foil sensor has a thickness of 13 µm to provide high vertical temperature resolution. This feature makes the sensor suitable for measuring surface temperature during CSC because the vertical temperature gradient in either a tissue phantom or human skin is much greater than that in the lateral direction [6]. The estimated response time is 2 ms and measurement uncertainty associated with K-type thermocouples is 0.28 ˚C after calibration. Thermal properties of tissues with different water content and epoxy are shown in Table 1. Details about preparation of the tissue phantom can be found in [15]. The measurement junction was aligned with the center of the spray cone, where the highest heat extraction occurs, and the tissue phantom was placed 35 mm away from the nozzle tip. Since PDPA and temperature measurements were performed simultaneously, the Results section presents average temperature measurements of approximately 10 experiments.

5.3.4 Isolation Chamber

The spray system and tissue phantom were placed inside a custom made chamber to maintain a reduced, constant relative humidity level, which is known to affect the efficiency of heat extraction from the tissue [16] and experimental repeatability. The chamber, schematically shown in Figures 5.1a and 5.1c, is made of transparent acrylic walls 12.7 mm thick. The walls were designed to be perpendicular to the PDPA's transmitter (laser beams) and receiver (photodetector) to minimize refraction and did not have an effect on droplet velocity although droplet diameter decreased (1–2 μm). Relative humidity levels were kept at 16–18% by flushing the chamber with dry air.

5.3.5 Spray Flux Calculations

Droplet velocity and size are two of the primary measurements required to calculate spray fluxes. The velocity measurement is not likely to influence the accuracy of overall flux since it is commonly measured with high accuracy. However, flux calculations are very sensitive to inaccuracies in droplet size measurements, which are elevated to the second or third power to calculate surface area or volume flux. Significant size errors can be made when the signal-to-noise ratio is low or if the assumption that a single scattering mode is dominant no longer holds. Rejection of improperly sized droplets or size validation has the disadvantage that these droplets are then missing in subsequent flux calculations. This then leads to a third primary measurement quantity, the number of particles passing through the detection volume during a given observation

time. In addition to rejection due to size validation, sources for counting errors are small droplets that fall below the detection threshold of the system and multiple particle passing simultaneously through the detection volume—leading to particle rejection or erroneous size information.

In this study we used a model that accounts for the complex geometry of the detection volume and for the probability of two or more drops in the probe volume simultaneously. The model is based on the assumption that the drops in the spray are distributed randomly and, consequently, the probability of two or more drops in the probe volume can be derived using the Poisson distribution. It is well known that for relatively dense sprays, like cryogen sprays at a short distance from the nozzle, the influence of overlapping signals from two or more drops on flux calculations may be significant.

Number, mass and kinetic energy fluxes of cryogen sprays were estimated from PDPA measurements following [17]:

$$\varphi = \frac{1}{\tau}\sum_{i=1}^{N}\frac{\eta_i \varphi_i}{A_{\gamma,i}(D_i,\gamma_i)}\vec{e}_{\gamma,i}\,, \tag{5.1}$$

where

$$\varphi_i = \begin{cases} 1 & \text{for number flux.} \\ \dfrac{\pi\rho}{6}D_i^3 & \text{for mass flux.} \\ \dfrac{\pi\rho}{12}D_i^3 V_i^2 & \text{for kinetic energy flux.} \end{cases} \tag{5.2}$$

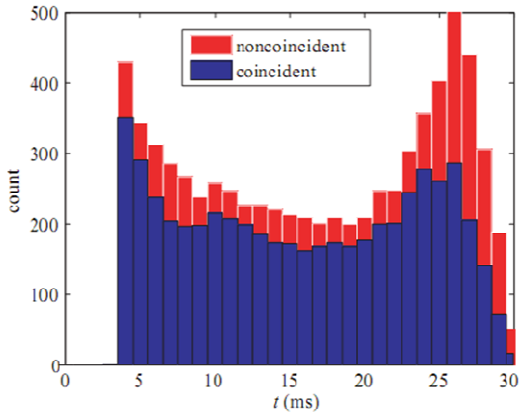

(a) Experimental Set

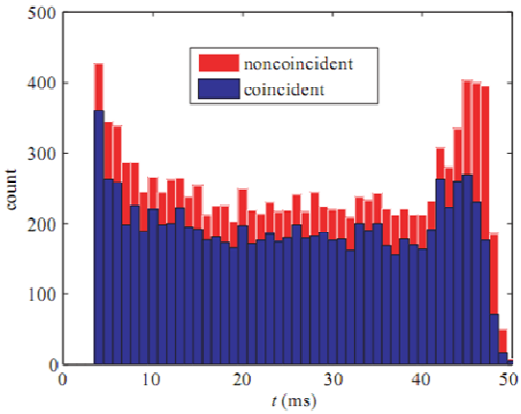

(b) Tissue phantom.

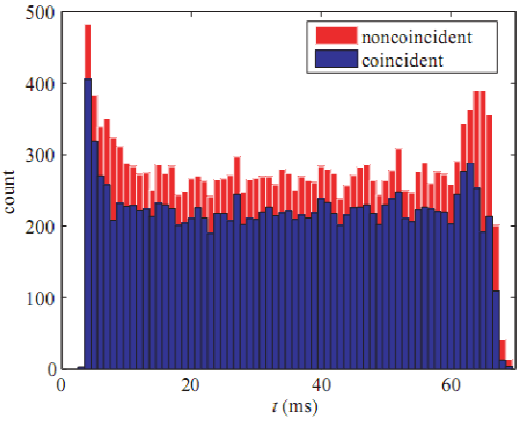

(c) Chamber and PDPA components (top view).

Figure 5.2: Count of coincident and non-coincident measurements in 1 ms time bins during CSC.

In addition to D and γ, A_γ is also a function of V, burst duration and hardware parameters (such as the width of the projected slit and the receiver off-axis angle). η accounts for count errors due to multiple particles scattering or for non-validation of particles and is a function of the relative signal presence (in the measured volume) of validated and non-validated signals. We used the coincident mode of our PDPA system to define validated signals; within this operational mode, a droplet diameter measurement corresponds to a simultaneous velocity measurement. With the coincident mode off, every signal corresponds to a velocity measurement but not necessarily to a diameter measurement. Coincident and non-coincident measurements counts per 1 ms bin are shown for 10, 30 and 50 ms spurts in Figure 5.2. Except for the last two bins in each figure (which are excluded from computations), there are more than 100 samples per bin. The difference between non-coincident and coincident measurements counts represents the number of non-validated particle size measurements, which in our PDPA system correspond to mismatches between two independent phase shifts (particle size) measurements—the system only accepts the velocity measurement. This situation may arise, for example, when there are two or more drops in the probe volume simultaneously. For details about the computation of η and A_γ the reader is referred to Roismann and Tropea [17].

5.3.6 Heat Flux Calculations

Temperatures recorded by the thin-foil sensor were assumed to be surface temperatures because the foil Biot number (hL/k) for a heat transfer coefficient h = 20,000 W/(m^2·K) [18], characteristic length $L = 13 \times 10^{-6}$ m and thermal conductivity k = 12 W/(m·K) [19] is ~2×10^{-2}; i.e., the temperature of the foil is spatially uniform, $hL/k << 1$. The following analytical expression based on Fourier's law and Duhamel's theorem was used to compute the surface heat flux q'' from the experimental temperature T:

$$q''_J = 2\sqrt{\frac{k\rho c}{\pi}} \sum_{j=1}^{J} \frac{T_j - T_{j-1}}{\sqrt{t_J - t_j} + \sqrt{t_J - t_{j-1}}} \tag{5.3}$$

A detailed derivation of Equation 5.3 can be found elsewhere [6, 20].

5.3.7 Heat Transfer Modeling

To model the thermal response of human tissue and epoxy to CSC, we solved the two-dimensional heat conduction equation:

$$\rho c \frac{\partial}{\partial t}\theta(x,y,t) - \nabla\left(k\nabla\theta(x,y,t)\right) = 0 \tag{5.4}$$

for which the surface boundary condition was specified as

$$-k\nabla\theta(x,0,t)\cdot\vec{n} = q''(t) \tag{5.5}$$

At the other boundaries, $-k\nabla\theta\cdot\vec{n}=0$. The computation domain was the following: -1 × 10^{-3} m $\leq$ x $\leq$ 1 × 10^{-3} m, -1.5 × 10^{-3} m $\leq$ y $\leq$ 0 m. Tissue thermal properties were approximated with empirical relations [13] and measured water content [21], Table 1. Thermal responses were modeled for human tissues with 0.3 and 0.6 g of water per g of total tissue, which correspond to the water content in the stratum corneum and epidermis, respectively.

5.4 Results and Analysis

5.4.1 An Epoxy Substrate as a Human Tissue Phantom

Figure 4.3a shows the experimental surface temperature T (left scale) during a 50 ms CSC spurt onto the tissue phantom and the corresponding surface heat flux q'' (right scale). This heat flux is next used as the boundary condition for comparing the thermal response between human tissues and tissue phantom. Figure 4.3(b) shows the numerical surface temperatures of the tissue with 0.3 and 0.6 water content, $\theta_{t,0.3}$ and $\theta_{t,0.6}$, and phantom, θ_p. The greatest temperature drops in tissues and phantom are $\Delta\theta_{t,0.3}$ = 51, $\Delta\theta_{t,0.6}$ = 27, and $\Delta\theta_{t,p}$ = 63 ˚C, respectively; temperature drops are 91%, 92% and 93% of $\Delta\theta_{t,0.3}$, $\Delta\theta_{t,0.6}$, and $\Delta\theta_p$, respectively, at t = 20 ms; lowest surface temperatures, -31, -7 and -43 ˚C, occur at t $\approx$60, 61 and 57 ms, respectively. Although dynamic responses of tissues and phantom to the same time-dependent heat flux are qualitatively similar, θ_p is considerably lower than θ_t. This is not surprising because the density—and mass for the same volume—and ability to conduct heat of these materials

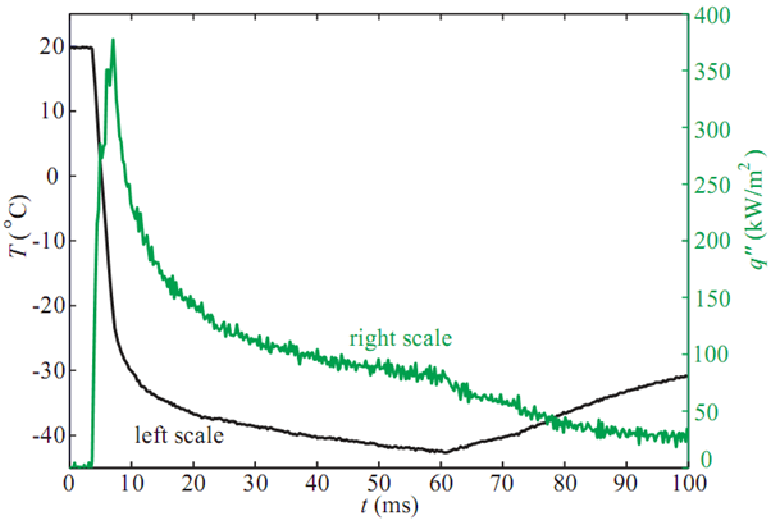

(a) Experiments on epoxy phantom.

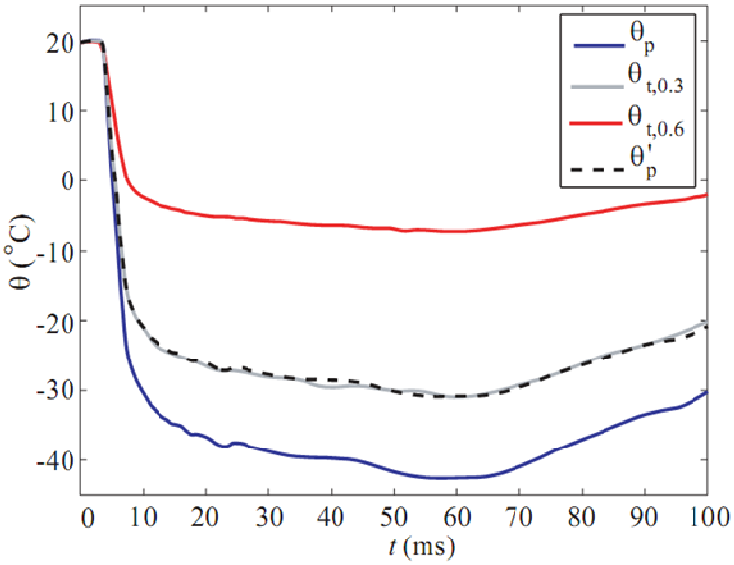

(b) Modeling of phantom and human tissue

Figure 5.3: (a) Experimental surface temperature (left scale) and estimated surface heat flux q'' (right scale). (b) Tissue and phantom surface temperature response, θ_t and θ_t, to q'' and mapped temperature, θ'_p, matching tissue response.

are comparable; however, more heat is needed to change the temperature of the tissues as compared to the epoxy, Table 1.

It is possible to introduce a simple transformation to map θ_p to θ_t as follows:

$$\theta_p'(t) = \theta_o + \xi\left(\theta_p(t) - \theta_o\right) \tag{5.6}$$

where θ_o is the initial temperature of the phantom and

$$\xi = \frac{k_p\sqrt{\alpha_t}}{k_t\sqrt{\alpha_p}} \tag{5.7}$$

The transformation is based on the analytical solution for constant surface heat flux evaluated at the surface [19]. Mapping of the epoxy surface temperature response to that of tissue with 0.3 water content, $\theta'_{p,0.3}$, is shown in Figure 5.3b, $\theta'_{p,0.3} = \theta_{t,0.3}$. Our results show that, assuming heat transferred from an epoxy tissue phantom during CSC is the same as that from tissue, $\Delta\theta_{t,0.3}$ and $\Delta\theta_{t,0.3}$ are 81% and 43% of $\Delta\theta_p$, respectively. Therefore, the thermal response of epoxy is better suited to study low-water content tissues, such as the stratum corneum, despite having a thermal diffusivity closer to that of the epidermis. However, the problem is far more complex as q'' is a function of the substrate thermal properties and spray thermodynamics such as phase (liquid, vapor) and temperatures. Dynamics of q'' during CSC of human tissue may be similar to those reported in this study; however, q'' might be quantitatively smaller and, subsequently, θ_t may drop even less than shown in Figure 5.3b.

We assumed that CSC would induce the same $q''(t)$ on each substrate and computed $\theta(t)$ to be able to compare dynamic thermal responses. An alternative approach would be to assume that CSC induces the same $\theta(t)$ on each substrate and compute $q''(t)$. To satisfy $\theta(t)_{s,0.6} = \theta(t)_{s,0.3} = \theta(t)_p$ it follows that $q''(t)_{s,0.6} > q''(t)_{s,0.3} > q''(t)_p$ because more heat extraction is needed to lower the temperature of substrates with higher specific heat, as stated above.

5.4.2 Spray Characteristics in Steady State

Figure 4 shows steady-state velocity and diameter distributions for a 50 ms cryogen spurt at the cone center and 32.5 mm away from the nozzle tip. The total droplet count was 16660, which resulted in a 1.1% deviation from the cumulative size distribution. Figure 4 shows that for a commercial spray system the velocities of cryogen droplets impinging onto the tissue surface range from 20–70 m/s and average 48 m/s. Droplet diameters as large as 15 µm and 6 µm on average were measured inside the chamber. However, because the chamber effects droplet diameter, droplets are expected to be as large as 17 µm and on average 8 µm under atmospheric conditions at the laboratory or clinic. Experiments at different relative humidity levels (16–50%) resulted in the same velocity and diameter values and distributions; i.e., the spray characteristics were not sensitive to changes in relative humidity conditions. Average velocity and diameter are in agreement with those reported in [4], 40 m/s and 13 mm, for a 25 mm nozzle-surface distance and a

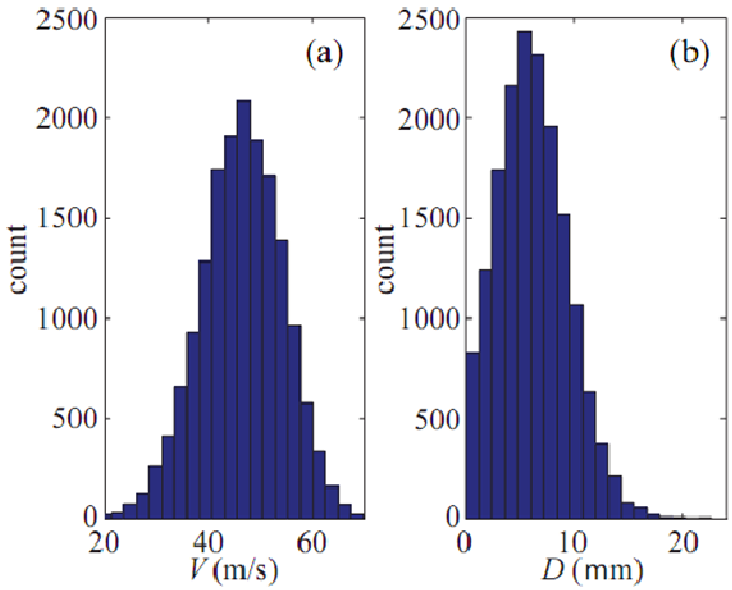

Figure 5.4: (a) Velocity and (b) diameter distributions for the cone center of a cryogen spray in steady state 32.5 mm away from the nozzle tip.

similar nozzle (65 mm length, 0.57 mm inner diameter). Although average droplet velocity and size for CSC of human tissue have been measured before [22], Figure 5.4 shows velocity and size distribution for a spray system and parameters currently used in clinical practice.

5.4.3 Fluid and Heat Transfer Dynamics during CSC

5.4.3.1 Spray Fluid Dynamics.

Average droplet velocity V and diameter D as a function of time during 10, 30 and 50 ms spurts are shown in Figure 5.5. The times at which steady states began, $\bar{t}_o$, and ended, $\bar{t}_f$, are represented by vertical dashed lines. Cryogen droplets took ~4 ms to reach the tissue phantom surface after the valve was energized. Independent measurements of laser light transmittance at the nozzle exit (not included) showed that this initial delay was mainly due to the valve's opening mechanics. Furthermore, if the initial droplets $V >$ 50 ms, their in-flight time from the nozzle to the phantom surface would be < 0.7 ms which is only a small fraction of the total delay time. For each spurt, the initial and final spray transients, respectively, lasted ~4 and 10 ms; these are the times required for the valve to fully open and close, respectively. Figure 5(a) shows that during the initial transient, t = 4–8 ms, V increased reaching a maximum of 55 m/s, then decreased to reach a steady state value $\bar{V}$ = 48 m/s. During the final transient, V increased monotonically beyond its initial transient maximum value. Final transients began 8 ms after the end of the period in which the normally closed valve was energized

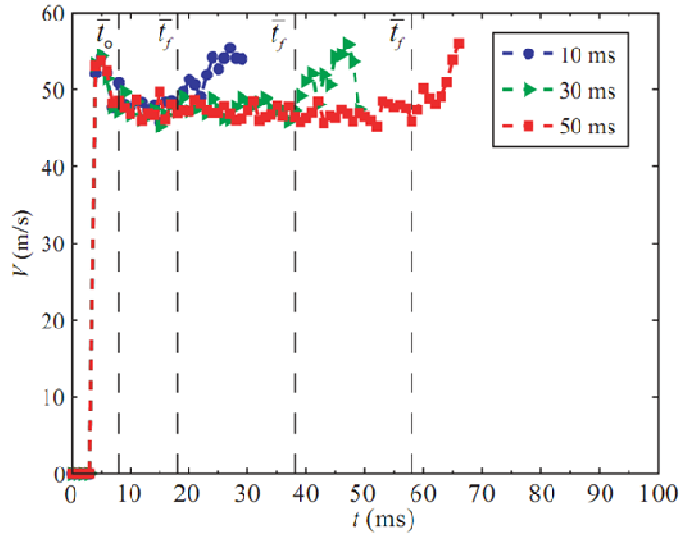

(a) Dynamics of droplet velocity.

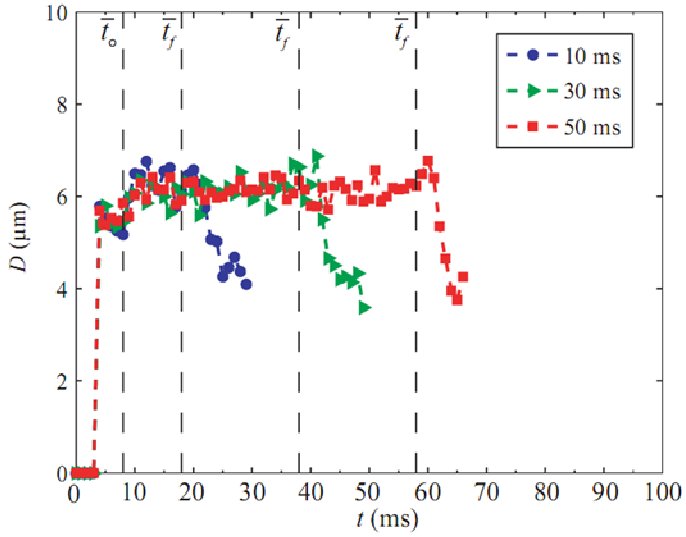

(b) Dynamics of droplet diameter.

Figure 5.5: Average cryogen droplet (a) velocity and (b) diameter as a function of time during 10, 30 and 50 ms cryogen spurts. Vertical dashed lines represent the beginning and end, $\bar{t}_o$ and $\bar{t}_f$, of the spray steady state.

(i.e., nominal spurt duration)—these times were also the end of the steady state, represented by vertical dashed lines $\bar{t}_f$ in the figures. Figure 5(b) shows that during the transient states, D decreased and increased when V increased and decreased, respectively; i.e., small droplets traveled faster than larger droplets and vice versa. Steady state value $\overline{D}$ = 6 μm. Flow through an orifice is proportional to the orifice area and fluid velocity; hence, for a constant flow the velocity is inversely proportional to the orifice area. During valve opening, initial droplets coming from a small orifice traveled faster than those coming from a fully open valve. Initial droplets were also smaller because they comprised the front of the spray and, consequently, were exposed to different surrounding conditions and aerodynamic forces (most likely resulting in different evaporation rates), such as, temperature differentials, saturated vapor levels and drag forces. During valve closure, droplet velocity also increased due to reductions in orifice area and droplet size decreased due to changes in aerodynamic forces.

5.4.3.2 Surface Heat Transfer Dynamics.

The average tissue phantom surface temperature T and heat flux q'' as a function of time during 10, 30 and 50 ms spurts are shown in Figure 5.6. Vertical dashed lines represent the spray $\bar{t}_o$ and $\bar{t}_f$, which are included to facilitate the transient-state correlation between spray characteristics and phantom cooling. As for the spray fluid dynamics, initial and final temperature transients can be identified in Figure 5.6a. Initially, T decreased abruptly during the first 6 ms (t = 4–10 ms), continued decreasing at a slower

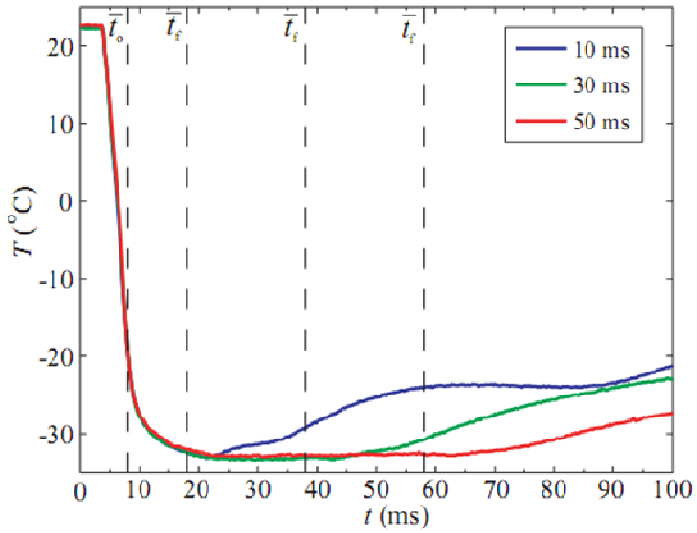

(a) Dynamics of surface temperature.

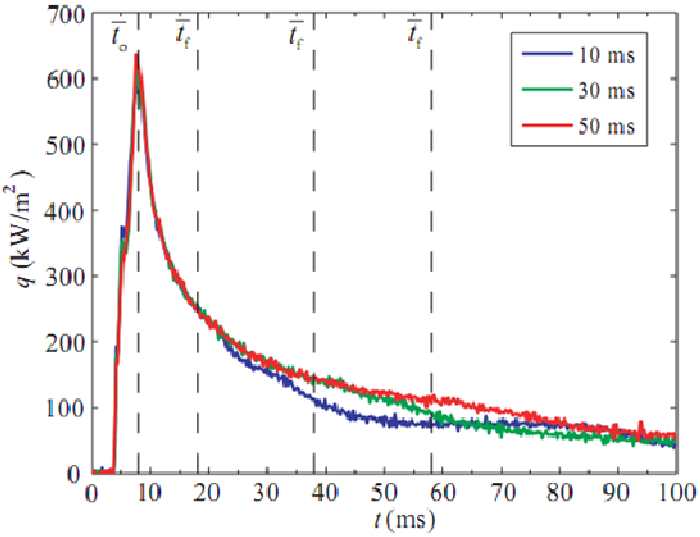

(b) Dynamics of surface heat flux.

Figure 5.6: Average tissue phantom surface (a) temperature and (b) heat flux as a function of time during 10, 30, and 50 ms spurts. Vertical dashed lines represent the beginning and end, $\bar{t}_o$ and $\bar{t}_f$, of the spray steady state.

rate during the next 10 ms (t = 10–20 ms) and, finally, reached steady state $\overline{T}$ = -33 ˚C, which was also the lowest surface temperature T_l. During the final transient, T slowly increased to reach room temperature. Figure 6(b) shows that q'' is highly dynamic: q'' increased abruptly reaching a maximum 5 ms after the droplets impinged on the surface; subsequently, q'' decreased at different rates from high to low—as evidenced by slope changes in the curves. The highest heat flux q_h'' = 591 (t = 8.1 ms), 611 (7.8 ms) and 636 kW/m^2 (7.5 ms) for 10, 30 and 50 ms spurt durations, respectively. Figures 6(a) and (b) also show that increasing the spurt duration increased the time when the surface remained at T_l (or $\overline{T}$) and decreased the rate of change of q''. Previous studies reported that T_l depends on spurt duration for nozzle-surface distances shorter than 25–30 mm but not for longer distances: T_l = -30 ˚C for a 0.7 mm inner diameter nozzle and 50 mm nozzle-substrate distance [23, 24]. Although there are differences in thermal sensors (location, type, dimensions), spray system (nozzle geometries, nozzle-surface distance) and experimental conditions (relative humidity level) between the present and cited studies, our results are in agreement with observations for large distances: in the present study T_l = -33 ˚C for each spurt duration, Figure 5.6a.

5.4.4 Spray and Tissue Phantom Fluid-Thermal Interactions

During the initial spray transient, when small and fast droplets wet the phantom surface, the greatest temperature drops and highest heat flux occurred because the temperature difference between the cryogenic liquid and warm substrate was at a maximum. If T is

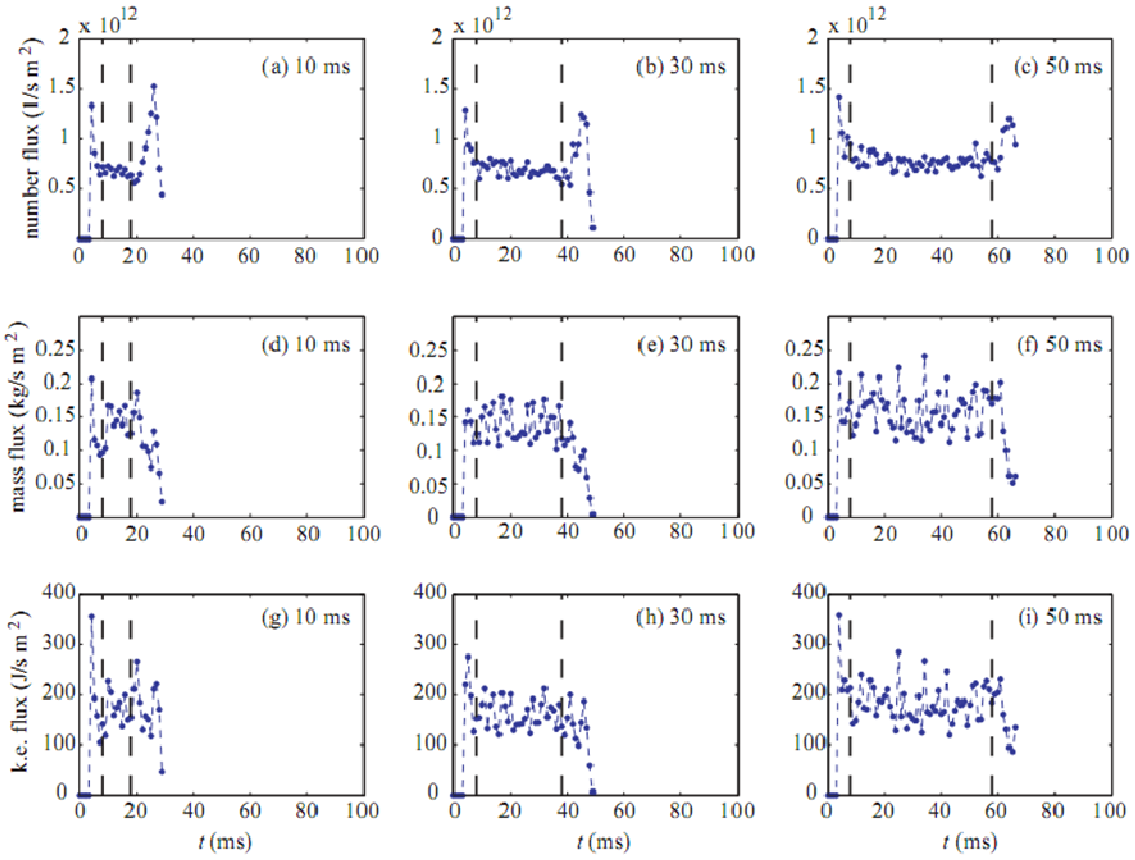

Figure 5.7: Spray number, (a)-(c), mass, (d)-(f), and kinetic energy, (g)-(i), fluxes during 10, 30 and 50 ms spurts. Vertical dashed lines represent the beginning and end (left and right lines, respectively) of the spray steady state.

lower than the cryogen boiling temperature T_b, it is reasonable to assume that there is liquid cryogen on the surface. It follows that during most of the spray steady state, the surface was wet with a pool of liquid since $T < T_b$. For the 30 and 50 ms spurts, after spurt termination T departed from $\overline{T}$ (t ~50 and 65 ms). For the 10 ms spurt, this departure occurred during the spray final transient state; a shorter spurt duration produced less accumulation of liquid cryogen during the spray steady state and, consequently, a surface—with a thinner pool—more sensitive to small changes in surface heat transfer.

During the final transient, droplets were smaller and faster but did not enhance the surface heat transfer. During this transient, there was an increase in the number flux followed by a decrease, Figures 5.7a–c, while the mass flux, Figures 5.7d–f, and kinetic energy flux, Figures 5.7g–i, only decreased. Therefore, during the final transient, droplets had less energy to penetrate into the liquid pool enhancing heat transfer, and their accumulation appeared to be negligible due to a low mass flux. Furthermore, even if these droplets had impinged on a cryogen free surface, the temperature difference between liquid and substrate would have been minor resulting in small heat fluxes.

5.4.5 Temperature Estimation for Human Tissue

Figure 8 shows the estimated human tissue temperatures using the transformation introduced in section 4.1 (Equation 5.6) and the experimental measurements presented in

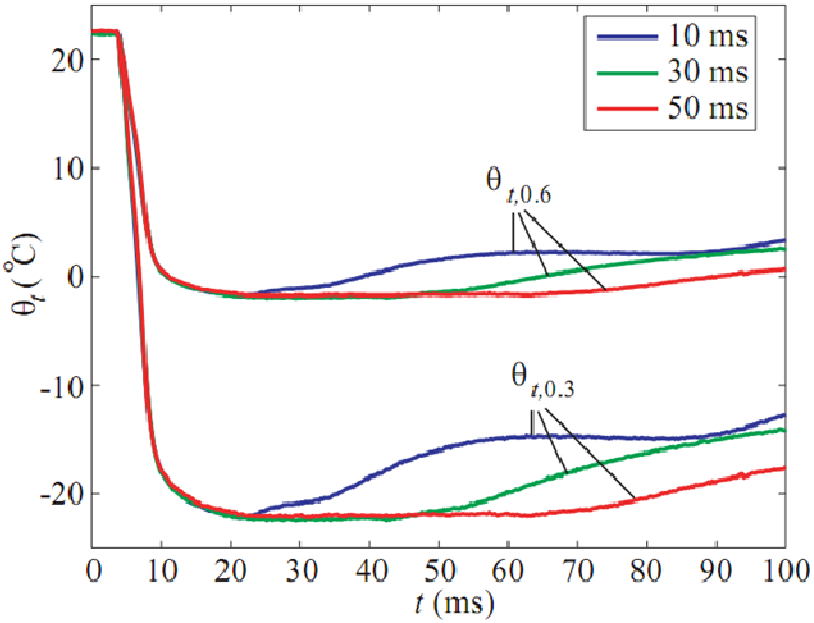

Figure 5.8: Estimated human tissue surface thermal responses during CSC with 10, 30 and 50 ms spurts for tissues with 0.3 and 0.6 water content.

Figure 5.6a; i.e., the surface thermal responses of stratum corneum and epidermis substrates to CSC. Although CSC is never applied directly to the epidermis, it is relevant to calculate the epidermal thermal-response to direct cooling to obtain an estimate of the lowest temperature boundary therein. $\overline{\theta}_{t,0.3}$ = -22 and $\overline{\theta}_{t,0.6}$ = -2 ˚C for $\overline{T}$ = -33 ˚C and an initial substrate temperature of 22.5 ˚C. However, human tissue (skin) temperature is considerably higher, ˜ 32.5 ˚C. Jia et al. [18] quantified the surface heat transfer during 50 ms (and 20 mm nozzle-substrate distance) CSC of substrates at different initial temperatures: 20, 40 and 80 ˚C, for which the lowest substrate temperatures were, respectively, -40, -35 and -30 ˚C. A 20 ˚C difference between initial temperatures resulted in a 5 ˚C difference between lowest temperatures. If the initial temperature was 32 ˚C in our experiments, it is reasonable to assume that $\overline{T} \approx$ -30 ˚C, for which $\overline{\theta}_{t,0.3} \approx$ 19 and $\overline{\theta}_{t,0.6} \approx$ 0 ˚C. Since the stratum corneum is the most superficial layer of human skin with a thickness of 20 µm above the epidermal layer, epidermal temperatures during CSC are expected to be higher than 0 ˚C even for larger spurt durations.

Phase of change at subzero temperatures of biological components with a water composition was not considered in this study. The stratum corneum has a very low water content since it is composed mainly of layers of death cells. Our results show that the epoxy thermal response is closer to that of stratum corneum. If phase of change is present, then a tissue phantom with higher water content may be appropriate for considering the changes in thermal properties of tissue as a function of temperature; for example, agar phantoms.

5.5 Conclusions

Numerical modeling of epoxy and human tissues with 0.3 and 0.6 water content (stratum corneum and epidermis, respectively) show that, subject to the same heat flux, their thermal response is qualitatively similar but the total temperature drops in tissues are about 81 and 43% less as compared to epoxy, respectively. Epoxy is a good thermal phantom to study low- water content tissues, such as the stratum corneum. A simple transformation can be used to map the temperature response of the epoxy to that of tissue. Using this transformation and experimental measurements on a tissue phantom, the lowest stratum corneum and epidermal temperatures in human tissue during CSC with commercial devices using 10, 30 and 50 ms spurts are estimated to be approximately -19 and > 0 ˚C, respectively.

Despite the relative short spurt durations, cryogen delivery is mostly a steady state process with initial and final transients mainly due to valve dynamics. Thermal transients are longer than fluid transients due to the low thermal diffusivity of human tissues; steady states are comparable in duration although there is an inherent thermal delay. During the initial spray transient, fast and small droplets (with respect to steady state values) induce large temperature drops and the highest heat flux since the temperature difference between cryogen and tissue phantom is greatest; during the spray steady state, surface temperature remains at its lowest value; during the final transient, droplets are fast and small again, although in this period their impact on the surface heat transfer is negligible due to decreasing mass and kinetic energy fluxes and, in particular, reduced temperature differences between cryogen and tissue phantom.

Steady state temperatures are the lowest surface temperatures experienced by the substrate, independent of spurt duration; hence, longer spurt durations result in larger exposures of the tissue to the same lower, steady state temperature as shorter spurts.

References

1. Nelson, J.S., et al., *Dynamic Epidermal Cooling During Pulsed-Laser Treatment of Port-Wine Stain - a New Methodology with Preliminary Clinical-Evaluation.* Archives of Dermatology, 1995. **131**(6): p. 695-700.
2. Nelson, J.S., et al., *Dynamic epidermal cooling in conjunction with laser-induced photothermolysis of port wine stain blood vessels.* Lasers in Surgery and Medicine, 1996. **19**(2): p. 224-229.
3. Aguilar, G., et al., *Influence of nozzle-to-skin distance in cryogen spray cooling for dermatologic laser surgery.* Lasers in Surgery and Medicine, 2001. **28**(2): p. 113-120.
4. Karapetian, E., et al., *Effects of mass flow rate and droplet velocity on surface heat flux during cryogen spray cooling.* Physics in Medicine and Biology, 2003. **48**(1): p. N1-N6.
5. Pikkula, B.M., et al., *Effects of droplet velocity, diameter, and film height on heat removal during cryogen spray cooling.* Annals of Biomedical Engineering, 2004. **32**(8): p. 1131-1140.
6. Franco, W., et al., *Radial and temporal variations in surface heat transfer during cryogen spray cooling.* Physics in Medicine and Biology, 2005. **50**(2): p. 387-397.
7. Franco, W., et al., *Extent of lateral epidermal protection afforded by a cryogen spray against laser irradiation.* Lasers in Surgery and Medicine, 2007. **39**(5): p. 414-421.

8. Hsieh, S.S. and H.H. Tsai, *Thermal and flow measurements of continuous cryogenic spray cooling.* Archives of Dermatological Research, 2006. **298**(2): p. 82-95.

9. Jia, W.C., et al., *Treatment of cutaneous vascular lesions using multiple-intermittent cryogen spurts and two-wavelength laser pulses: Numerical and animal studies.* Lasers in Surgery and Medicine, 2007. **39**(6): p. 494-503.

10. Aguilar, G., et al., *Cryogen spray cooling efficiency: Improvement of port wine stain laser therapy through muttiple-intermittent cryogen spurts and laser pulses.* Lasers in Surgery and Medicine, 2002. **31**(1): p. 27-35.

11. Anvari, B., et al., *Nd:YAG laser irradiation in conjunction with cryogen spray cooling induces deep and spatially selective photocoagulation in animal models.* Physics in Medicine and Biology, 1997. **42**(2): p. 265-282.

12. Tate, R.W. *Some problems associated with the accurate representation of droplet size distributions*. in *Proceedings of the Second International Conference on Liquid Atomization and Spray*. 1982.

13. Jacques, S.L., et al., *Pulsed Photothermal Radiometry of Port-Wine-Stain Lesions.* Applied Optics, 1993. **32**(13): p. 2439-2446.

14. Tunnell, J.W., J.H. Torres, and B. Anvari, *Methodology for estimation of time-dependent surface heat flux due to cryogen spray cooling.* Annals of Biomedical Engineering, 2002. **30**(1): p. 19-33.

15. Jia, W.C., et al., *Improvement of port wine stain laser therapy by skin preheating prior to cryogen spray cooling: A numerical simulation.* Lasers in Surgery and Medicine, 2006. **38**(2): p. 155-162.

16. Majaron, B., et al., *Cryogen spray cooling in laser dermatology: Effects of ambient humidity and frost formation.* Lasers in Surgery and Medicine, 2001. **28**(5): p. 469-476.

17. Roisman, I.V. and C. Tropea, *Flux measurements in sprays using phase Doppler techniques.* Atomization and Sprays, 2001. **11**(6): p. 667-699.

18. Jia, W.C., et al., *Heat-transfer dynamics during cryogen spray cooling of substrate at different initial temperatures.* Physics in Medicine and Biology, 2004. **49**(23): p. 5295-5308.

19. Incropera, F.P., *Fundamentals of heat and mass transfer*. 2007, Hoboken, NJ: John Wiley.

20. Beck, J.V., B. Blackwell, and C.R. St. Clair Jr., *Inverse Heat Conduction: Ill Posed Problems*. 1985, New York: Wiley. 308.

21. Caspers, P.J., et al., *Automated depth-scanning confocal Raman microspectrometer for rapid in vivo determination of water concentration profiles in human skin.* Journal of Raman Spectroscopy, 2000. **31**(8-9): p. 813-818.

22. Aguilar, G., et al., *Experimental study of cryogen spray properties for application in dermatologic laser surgery.* Ieee Transactions on Biomedical Engineering, 2003. **50**(7): p. 863-869.

23. Aguilar, G., G.X. Wang, and J.S. Nelson, *Dynamic behavior of cryogen spray cooling: Effects of spurt duration and spray distance.* Lasers in Surgery and Medicine, 2003. **32**(2): p. 152-159.

24. Aguilar, G., G.X. Wang, and J.S. Nelson, *Effect of spurt duration on the heat transfer dynamics during cryogen spray cooling.* Physics in Medicine and Biology, 2003. **48**(14): p. 2169-2181.

CHAPTER 6: The Effect of Ambient Pressure and Impact Angle on Droplet Splashing

Nomenclature

Ca	capillary number ($V\mu/\sigma$)
C_g	sound speed in ambient gas
C_l	sound speed in liquid
$\vec{F}$	force
h	thickness of flatten droplet at maximum spread diameter
k	wave number
m	mass
M_m	molecular weight of the gas [g/mol]
n	adiabatic gas constant
p	ambient gas pressure
P_o	atmospheric pressure [1atm]
P	pressure inside droplet
r	radius of droplet spread
R_m	maximum spread radius
Re	Reynolds number ($\rho VD/\mu$)
R_u	universal gas constant [8314 Nm/kg/mol/K]
t	time from droplet impact
t_c	characteristic spreading time
T	temperature
T_{sat}	saturation temperature of droplet at 1 atm
V	droplet velocity
$\vec{V}_n$	impact velocity in normal direction to the impact surface
V_{rel}	relative velocity
V_s	spreading velocity
We	Weber number ($D\rho V^2/\sigma$)

Greek symbol

μ	dynamic viscosity
ν	kinematic viscosity
ω	interface growth rate

θ	static wetting angle
ρ	liquid density
ρ_g	ambient gas density
σ	surface tension
τ_{ST}	shear stress caused by surface tension

6.1 Introduction

In this study, we observe and record the dynamics of droplets of various fluid properties as they impact against a rigid solid dry surface at different inclination angles, at pressures ranging from 0.2 to 6 atm. Though they are known to influence impact dynamics, the influence of surface wettability and temperature on splashing threshold was assumed to be small relative to other factors [1]. Based on the experimental results, we develop an empirical expression to predict the threshold of splashing that uses the balance between the droplet internal pressure and the droplet surface tension while considering K-H instability and gas pressure. To further validate the applicability of the K-H instability on splashing, a numerical simulation based on a volume of fluid (VOF) algorithm was also performed.

Table 6.1: Properties of FC-72 in comparison to water and ethanol.

	FC-72	**H_2O**	**CH_3OH**
Density ρ (kg/m^3)	1680	1000	791
Surface tension σ $(mN/m)/T$	12.0	73	26
Viscosity μ (Pa s)	0.00064	0.000978	0.00058
Boiling point (^oC)	56	100	65

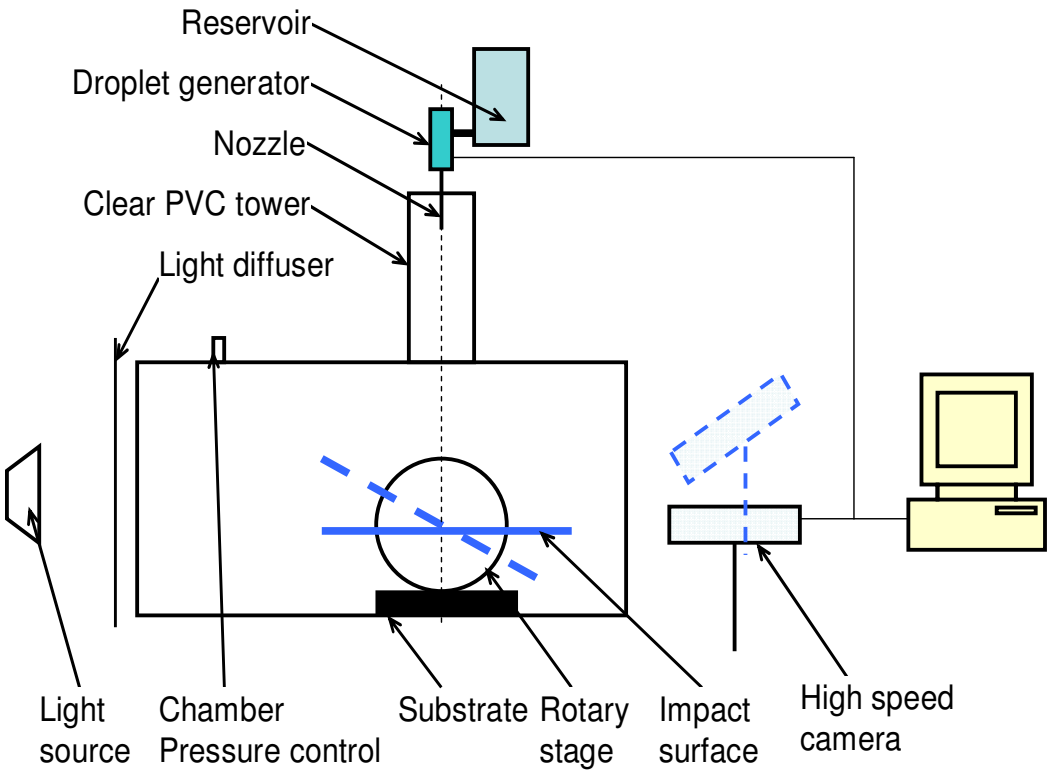

Figure 6.1: A schematic diagram of the experimental set up.

6.2 Methods

6.2.1 Experimental Approach

The liquid used in this study was FC-72 or perfluorohexane (C_6F_{14}) whose properties are shown in Table 6.1 along with two other commonly used liquids, water and ethanol, for comparison. FC-72 is normally used as an electronic cooling fluid and its selection for the current study provided a wide range of values for the Weber number (*We*). A diagram of the experimental set is provided in Figure 1. A precision micro-liter valve (Model 740V-SS, EFD Inc., East Providence, RI, USA) with stainless steel tips of various outer diameters was used to generate droplets of 1.7 mm diameter. The distance from the

nozzle tip to the impact surface was varied from 0.06 to 1.32 m to produce impact velocities from 1 to 5 m/s. A smooth Plexiglas surface with less than 0.8 μm in roughness was mounted on a rotary stage (Model B5990TS, Velmex Inc., Bloomfield, NY, USA) at various impact angles ranging from 0^o to 45^o relative to the horizontal plane.

To help quantify the significance of K-H instability, ambient air pressure was varied from 1-6 atm by performing experiments in an aluminum pressure chamber. Dry air was used to vary ambient pressure. All experiments were performed isothermally at 298 K to maintain constant fluid properties and eliminate heat transfer effects. Two clear, polycarbonate windows facilitated video imaging of the impact phenomena using a Phantom V7.1 high-speed video camera at a rate of 4,800 to 17,021 frames per second. Quantitative results for each condition were determined by averaging 4 test runs.

6.2.2 Numerical Simulation

To study how the ambient gas pressure affects splashing during impact, computational fluid dynamics (CFD) software, Fluent 6.3 (Fluent Inc., Lebanon, NH, USA) was used to simulate the droplet impact, based on an implicit volume of fluid (VOF) scheme. This scheme simulates multiphase flows by assigning a volume fraction of each phase within each cell. If α_q is the volume fraction of the q^{th} fluid, then values of α_q =0 and α_q =1 represent cells empty and full of the q, respectively. Values of α_q between 0 and 1 represent interfaces between phases. The interface is tracked using continuity:

$$\frac{\partial \alpha_q}{\partial t} + u_i \frac{\partial \alpha_q}{\partial x_i} = 0 \tag{6.a}$$

The momentum equation is used to solve a single velocity field representing all phases:

$$\frac{\partial}{\partial t}\rho u_j + \frac{\partial}{\partial x_i}\rho u_i u_j = -\frac{\partial P}{\partial x_j} + \frac{\partial}{\partial x_i}\mu\left(\frac{\partial u_i}{\partial x_j} + \frac{\partial u_j}{\partial x_i}\right) + \rho g_j + F_j \tag{6.b}$$

with fluid properties determined by using volume fraction averages, *e.g.* for μ:

$$\mu = \sum \alpha_q \mu_q \tag{6.c}$$

FC-72 droplets of 1.7 mm in diameter were generated and allowed to impact at velocities of either 2 or 5 m/s. The droplets impacted onto a horizontal or 45^o inclined surface at surrounding ambient pressures of 1 or 4 atm. Although the droplet was spherical, a 2-D simulation, instead of a full 3-D simulation, was performed [2] to increase the calculation efficiency. It can be reasonably assumed that the impact phenomena are axially symmetric. Therefore, a 2-D simulation through the center of the droplet should adequately resolve the flow phenomena. A rectangular calculation domain of 4 mm in width and 3 mm in height was used, and the initial position of the droplet was set at the center of the calculation domain. Larger domains were tested, but this had no impact on the results during the time period of interest. The boundary condition at the impact surface was a solid wall [2] and the other three boundary conditions were also set to a solid wall [3]. For all simulations, the initial velocity of the air was set to 0.

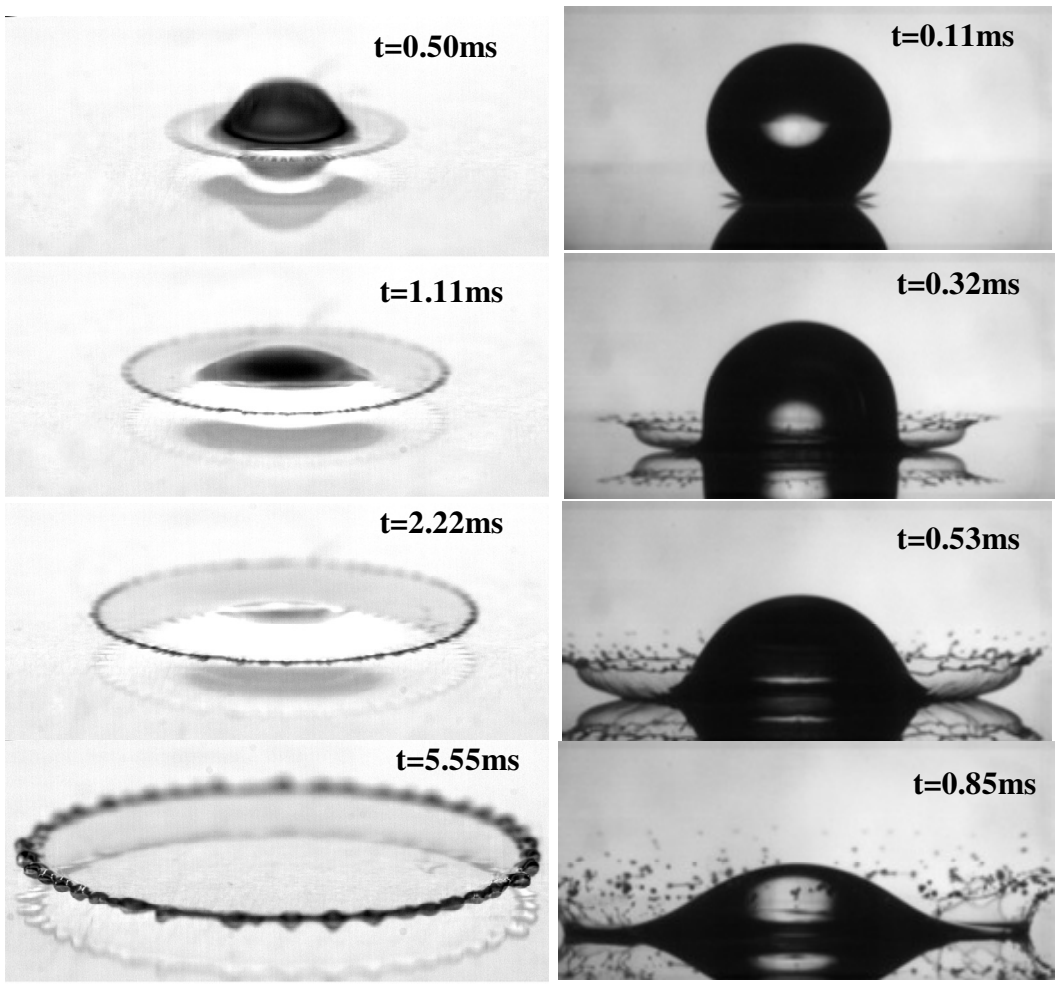

Figure 6.2: Effect of *We* on splashing. Left column: Water droplet with *We* = 695; and Right column: Ethanol droplet with *We* = 1870 [6].

A dynamic mesh was used, with finer element spacing near the impact surface. The governing equations were solved using a fully implicit scheme with a strict convergence criterion, $\varepsilon_n^{l,m} = (U_n^{l,m+1} - U_n^{l,m}) / U_n^{l,m} < 10^{-6}$, where n is the element; l is the time step and m is iteration. The simulation showed good convergence with an error decreasing to 10^{-9} as l increased for each element. A time step of less than 10^{-5} s was used in the final simulation.

6.3 Experimental Results

6.3.1 Effect of the Weber Number (*We)*

Figure 2 shows the effect of *We* on the impact dynamics. For *We* = 695 (left side) it is observed that the water sheet spreads along the flat surface with no splash, For *We* = 1870 (right side), however, the edge of the liquid is ejected at a certain angle from the horizontal plane at *t* = 0.11 ms. At *t* = 0.32 ms, a crown-shaped splash is clearly observed. At *t* = 0.85 ms, tiny water droplets are separated from the main crown structure of the liquid.

6.3.2 Effect of Ambient Pressure

Figure 3 shows a sequence of a FC-72 droplet impact against a flat surface for *We* = 970 at different values of the ambient pressure ranging from 1 to 6 atm. At 1 atm, the FC-72 liquid spreads along the flat surface and no splashing occurs. As the pressure increases to 2 atm, mild splashing is observed at the advancing edge of the spread. The splash droplets also travel a longer distance than the leading edge of the spread on the flat surface. By further increasing the pressure to 4 atm, splashing is observed earlier than

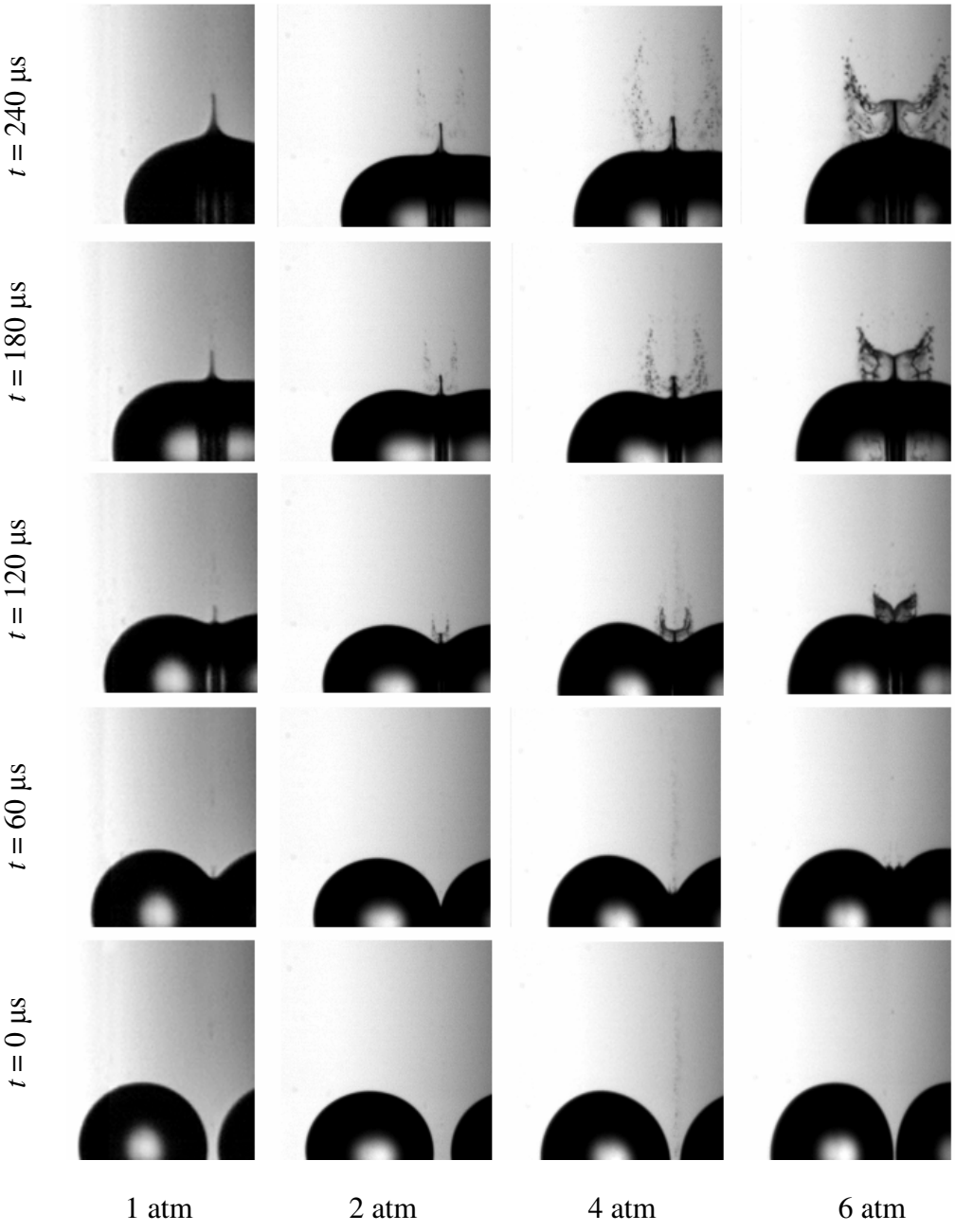

Figure 6.3: Effect of ambient air pressure on splashing with FC-72 droplet with $We = 970$ and $Re = 8700$ with pressure at 1, 2 4 and 6 atm for frames at each row, respectively.

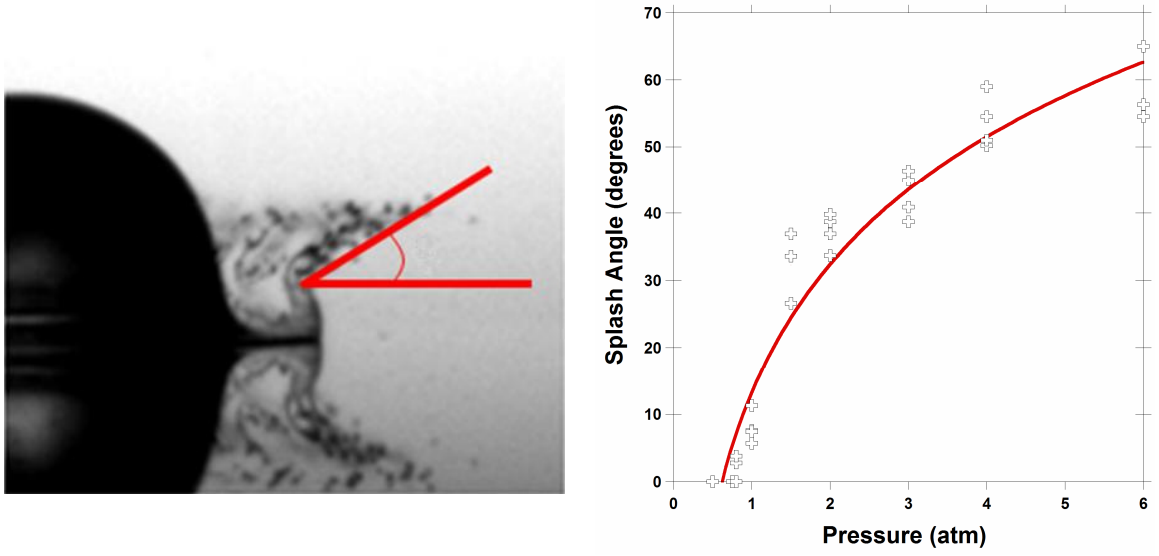

(a) (b)

Figure 6.4: (a) A depiction of the method of splash angle measurement. (b) Splash angle increases as the ambient pressure increasing with FC-72 droplet with *We* = 970 and *Re* = 9620.

that at 2 atm. Splashing is also stronger and the height of the splashed droplets is larger, but spreading still occurs along the impact surface. At 6 atm, splashing is again more pronounced and develops into a crown shape, which is different from the shape of the splashing at 2 and 4 atm. The bottom of the splash is detached from the flat surface at a large angle. The height of the splashed droplets at 6 atm is also higher than that at 4 atm.

To provide some quantitative description of the splashing phenomenon, the angle between the splashing projectile and the horizontal level was obtained, as shown in Figure 4a, from a series of high-speed images. Figure 4b shows how the splashing angle increases with increasing ambient pressure for an FC-72 droplet. Splashing angles of 10^{o}, 30^{o}, 45^{o} and 60^{o} correspond to ambient pressures of 1, 2, 4, and 6 atm, respectively. From

the weak splashing at 2 atm to the strong crown splashing at 6 atm, it is clear that the ambient pressure has a significant effect on the splashing behavior.

6.3.3 Effect of Impact Angle

In addition to the ambient pressure, the impact angle is another important parameter affecting the splashing. Figure 5 shows the impact of a FC-72 droplet onto an inclined Plexiglas surface at angles of 15^{o}, 30^{o} and 45^{o} for We = 970 and gas pressure of 3 atm. The arrows show the inclined and normal directions of the impact plate, respectively, and the cross indicates the initial point of contact. At 15^{o}, the splash occurs clearly on both sides of the droplet. However, unbalanced splashing is observed with spreading distance and splash height in the downhill direction larger than that in the uphill direction. As the inclination angle increases to 30^{o} the magnitude of splashing is much weaker and only occurs in the downhill direction. Again, the displacement of the FC-72 layer is much larger in the downhill direction. At 45^{o}, the splashing is nearly eliminated but with significantly higher overall spreading displacement downhill. The velocities in the downhill and uphill directions were measured by using image measurement software as shown in Figure 6. The downhill velocity is larger than the uphill velocity for all the inclined surfaces. At t = 70 μs, the dimensionless velocities (Vs/V), where Vs is the spreading velocity of the liquid sheet and V the impact velocity) of downhill and uphill are 3.65 and 3.17 for 15^{o}; 3.99 and 2.83 for 30^{o}; and 4.54 and 2.81 for 45^{o}. Thus, the differences of the dimensionless velocity between the downhill and uphill directions are

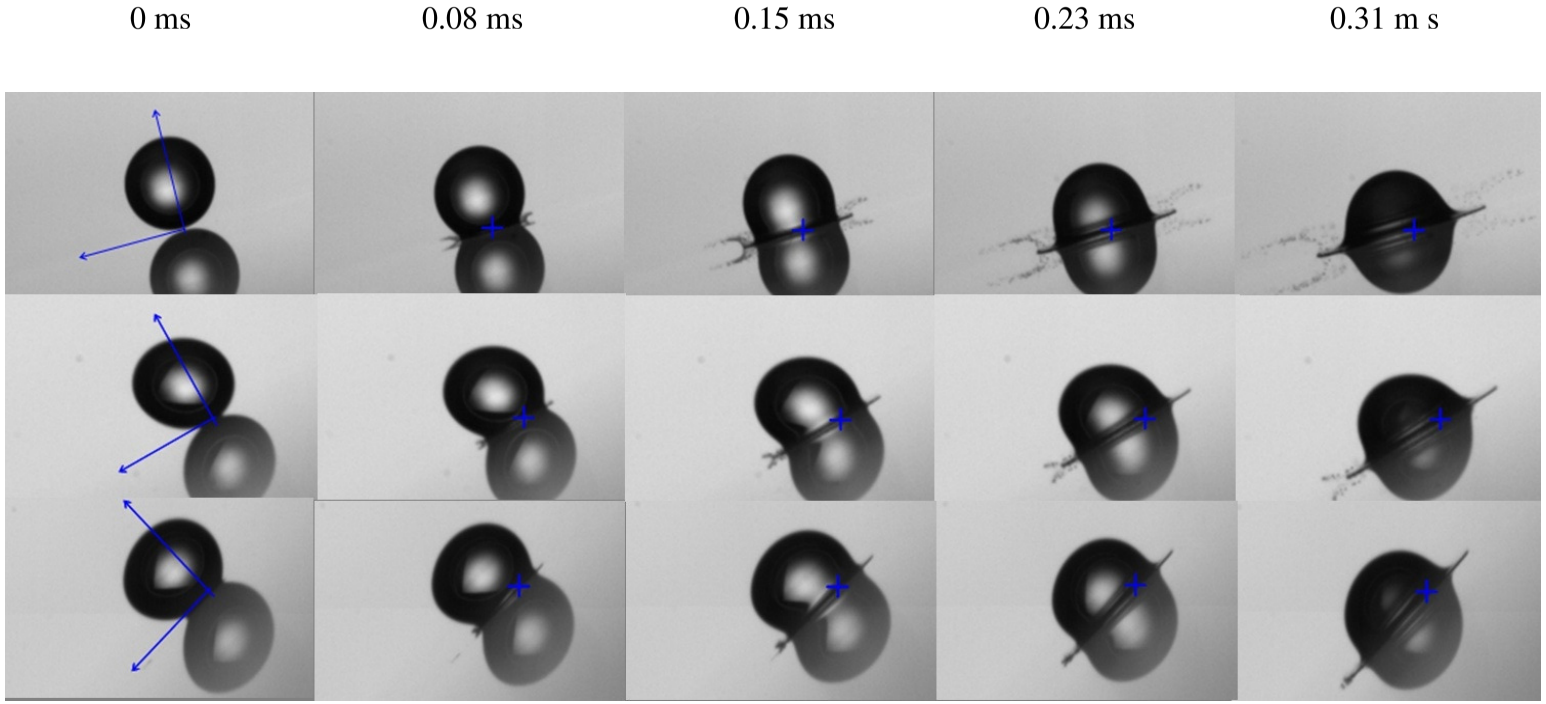

Figure 6.5: Effect of angle of impact surface. Top: inclined angle 15^{o}; middle: inclined angle 30^{o} and bottom: inclined angle 45^{o} with FC-72 droplet with *We* = 970 and *Re* = 8700 at 3 atm. The marked cross is an impact point.

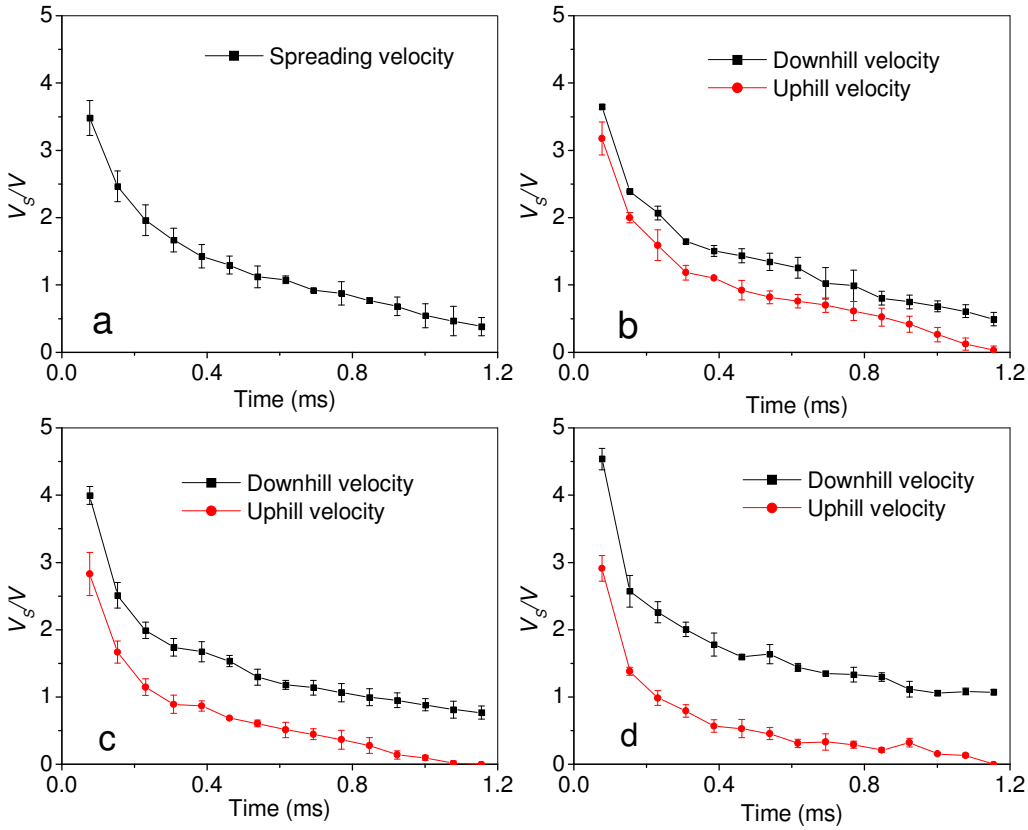

Figure 6.6: Spreading velocity of downhill and uphill with FC-72 droplet with *We* = 970 and *Re* = 8700 impact onto (a) flat surface, (b) 15°, (c) 30° and (d) 45° angle Plexiglas.

0.48, 1.16 and 1.78, respectively. At 1.2 ms after impact, the dimensionless velocities uphill are about 0 for all three cases of inclined surfaces, but the dimensionless downhill velocities are 0.6, 1.1 and 1.4 for inclination angles of 15°, 30 ° and 45°, respectively.

6.4 Numerical Results

Figures 7a and 7b show the simulation of air movement near the droplet of D = 1.7 mm just in contact with the substrate at ambient pressures of 1 and 4 atm, respectively. The impact velocity V was 2 m/s for We = 970 and Re = 8700. The solid curve shows the contour of the droplet as it establishes contact with the surface. At this stage, the spreading or splashing has not yet occurred and the front edge of the droplet flattens at the contact area. The air between the droplet and the impact surface moves outward quickly near the contact area.

The effect of the ambient gas pressure on the magnitude and angle of the air velocity vectors is also shown. Increasing the value of the ambient pressure reduces the maximum air velocity from 30.4 m/s at 1 atm to 26.4 m/s at 4 atm, but the air velocity angle increases with pressure. Figure 7c shows that the air velocity near the contact area of the droplet moving at V = 5 m/s and 1 atm is much greater than that of the droplet moving at V = 2 m/s. As V increases from 2 m/s to 5 m/s, the movement of the air near the contact point increases dramatically; the maximum velocity of the air is about 30 m/s for the droplet impacting at V = 2 m/s and it reaches a value over 80 m/s when the droplet impacts at V = 5 m/s.

Figure 8 shows that at the impact angle of 45^{o} for V = 2 m/s, the maximum air velocity in the downhill direction is only 22 m/s, while it is less than 10 m/s in the uphill direction; both being

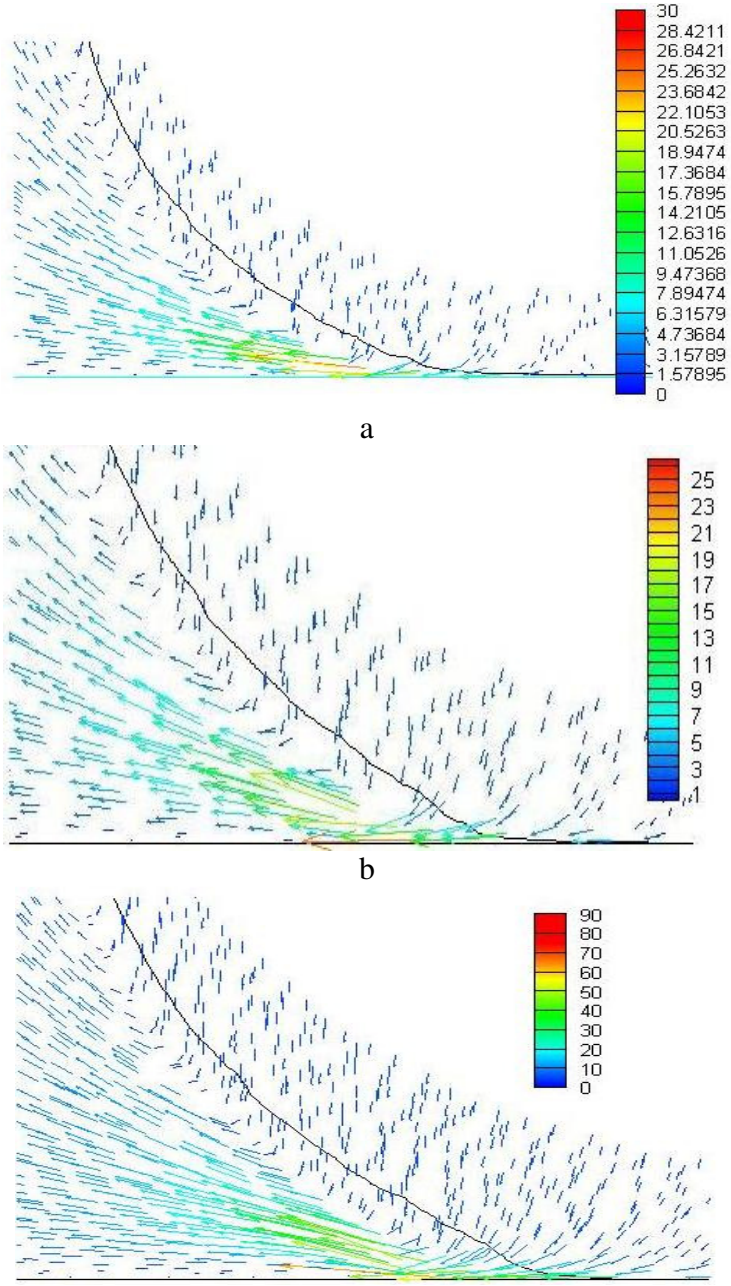

Figure 6.7: The velocity profiles of the air as the FC-72 droplets with 1.7 mm in diameter initiate contact with flat surface. (a) V = 2 m/s at 1 atm pressure; (b) V = 2 m/s at 4 atm pressure; and (c) V = 5 m/s at 1 atm pressure.

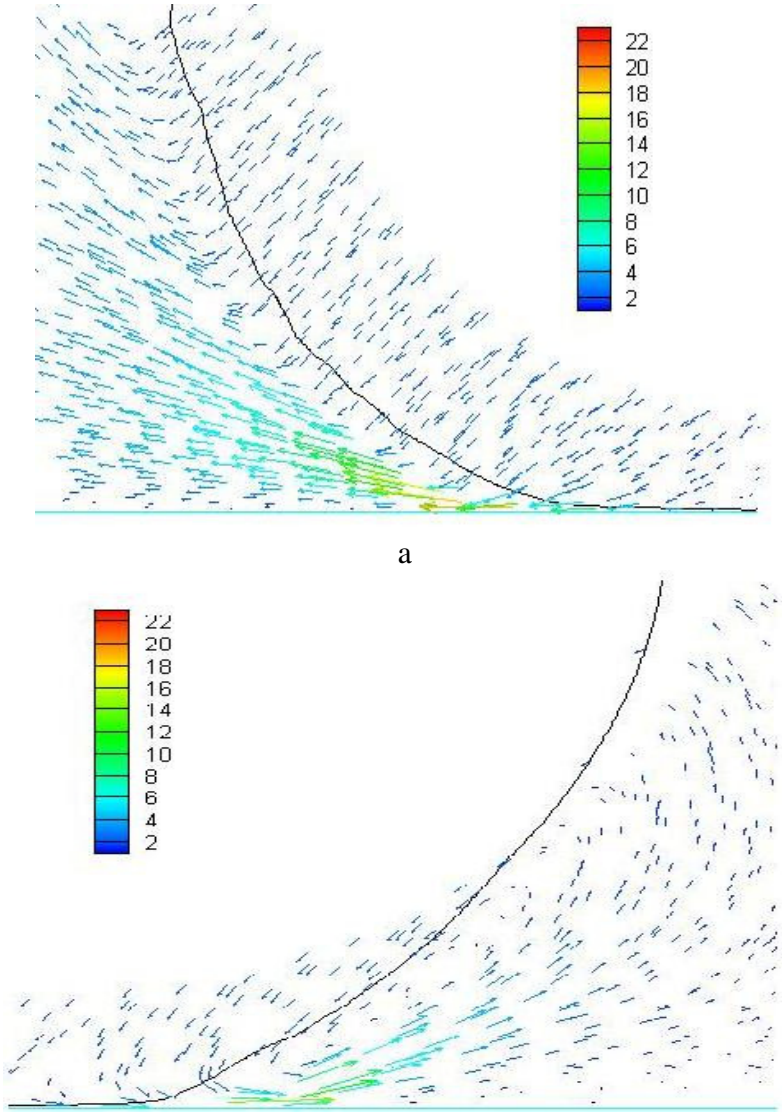

Figure 6.8: Velocity profile of FC-72 droplet with D = 1.7 mm and V = 2 m/s impact onto inclined surface with angle 45^{o}. (a). Downhill direction; (b) Uphill direction.

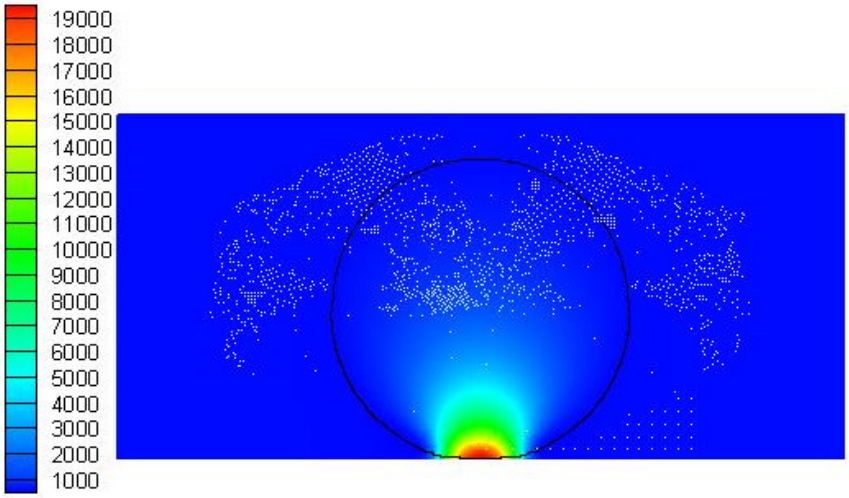

a

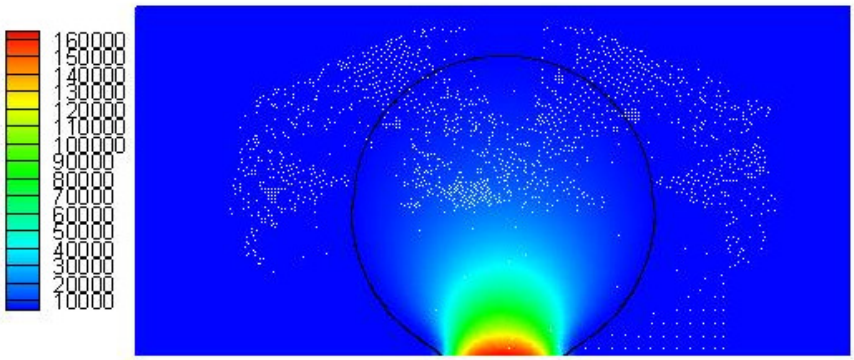

b

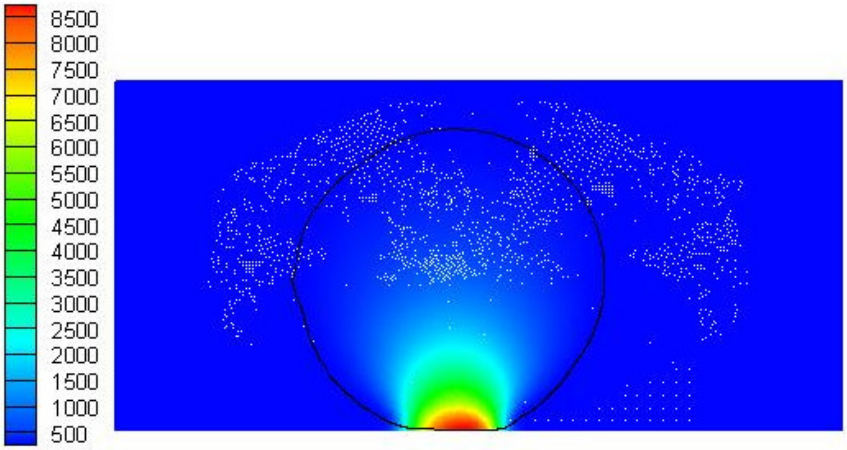

c

Figure 6.9: The pressure profile of droplet with 1.7 mm in diameter initiating contact with impact surface. (a) V = 2 m/s at 1 atm; (b) V = 5 m/s at 1 atm and (c) V = 2 m/s at 1 atm, 45^{o} inclined surface.

lower than the corresponding air velocity seen for impacts on a horizontal surface ($\approx$30 m/s), as seen in Figure 7.

Figure 9 shows the simulated pressure profile inside the droplet. Some aberrations in the droplet boundary can be seen and occurred due to the change in mesh spacing, but this is far from the area of interest and did not affect the results. Figure 9a shows the case of a droplet with D = 1.7 mm impacting at V = 2 m/s on a horizontal surface. The maximum internal pressure at the moment of impact is 19 kPa. For V = 5 m/s, the maximum pressure increases to 160 kPa, as seen in Figure 9b. Note too, that as the same droplet of D = 1.7 mm and V = 2 m/s impacts onto a 45^{o} inclined surface, the maximum pressure reaches only 8.5 kPa, as seen in Figure 9c.

6.5. Analysis

6.5.1. Splashing Threshold

According to previous research, the pressure inside the droplet is generated during the process of impact or during the conversion of the momentum of the impacting droplet into the momentum of flow along the impact surface [4]. Once the inside pressure exceeds the surface tension, splashing occurs. The most recognized theory that explains how pressure is generated in the droplet during droplet impact is the "water hammer" effect [5],

$$P = \rho V C_l \,, \tag{6.1}$$

where ρ is the liquid density, V is the droplet impact velocity, and C_l is the speed of sound in the liquid. In the water hammer theory, the liquid on the contact area is compressed and pressure is generated as the shockwave propagates in the liquid with the speed of sound. Once the front of the shockwave reaches the free surface of the liquid droplet, spreading or splashing is initiated. Therefore, the pressure due to the impact initiates splashing. However, this analysis only considered the cases in which the droplet impact velocity was over 100 m/s. Xu [6] modified Equation 6.1, and the pressure due to the water hammer effect for low impact velocity was expressed as

$$P \sim \rho_g V_S C_g \,, \tag{6.2}$$

where ρ_g is the gas density, V_S is the spreading velocity after droplet impact on a solid surface, and C_g is the speed of sound in the gas. Considering the ideal gas formulation, ρ_g can be written as

$$\rho_g = \frac{pM_m}{R_u T} \,, \tag{6.3}$$

where p is the ambient gas pressure, M_m is the molecular weight of the gas, R_u is the universal gas constant (8314 N m/kgmol K), and T is the gas temperature. The speed of sound in the gas is expressed as

$$C_g = \sqrt{\frac{nR_uT}{M_m}}\,, \tag{6.4}$$

where n is the adiabatic constant for a compressible gas. The velocity of the spreading edge is

$$V_S = \sqrt{\frac{DV}{4t}}\,. \tag{6.5}$$

Thus, the pressure caused by the shock wave can be expressed as:

$$P \sim \rho_g C_g V_S = \frac{pM_m}{R_uT} \cdot \sqrt{\frac{nR_uT}{M_m}} \cdot \sqrt{\frac{DV}{4t}}\,. \tag{6.6}$$

The stress caused by the surface tension can be expressed as

$$\tau_{ST} = \sigma / h = \sigma / \sqrt{\nu t}\,, \tag{6.7}$$

where σ is the surface tension, h is the thickness of the liquid layer and ν is the kinematic viscosity of the liquid. Thus, the splash occurs when the ratio of

$$P / \tau_{ST} \sim \sqrt{nM_m}\, p \cdot \sqrt{\frac{DV}{4R_uT}} \frac{\sqrt{\nu}}{\sigma} > S_{critical}\,. \tag{6.8}$$

From experimental results, $S_{critical}$ was found to be 0.45 [6]. Interestingly, Equations 6.5 and 6.6 show that P should increase proportionally with V_s, and the empirical correlation expressed by Equation 8 shows that, provided the P/τ_{ST} ratio exceeds $S_{critical}$, splashing should occur. That is, Equation 6.8 can predict the splashing threshold of droplets impacting against flat horizontal surfaces for any given ambient pressure (p) and impact velocity (V). However, this prediction is in contradiction with our experimental results on inclined surfaces (Figure 6), which show that as V_s increases with steeper angles, splashing is reduced.

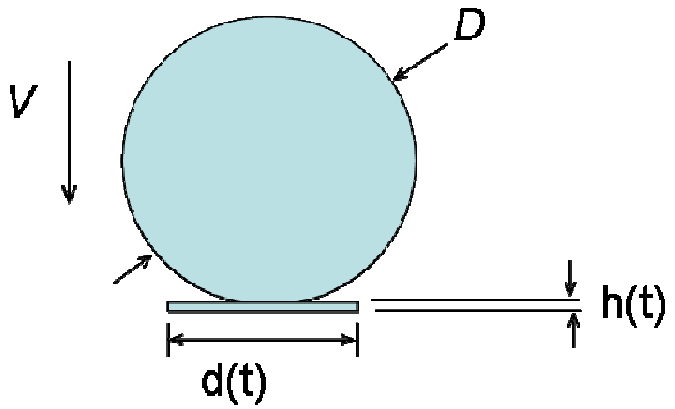

Figure 6.10: Sketch of the spreading after droplet impact onto rigid flat surface.

Until now, the most accepted explanation has been that splashing occurs once the momentum of the droplet cannot be converted into the momentum of flow along the surface [7]. Although the droplet impact is a dynamic and transient process, we simplified the impact analysis by assuming that the droplet impact was a pseudo-steady state process, as shown in Figure 10, to illustrate the effects of droplet velocity and impact angle on the pressure variation inside the droplet. During this pseudo steady-state

impact process, the momentum variation of the droplet at contact with the impact surface can be expressed as

$$\frac{dm\vec{V}_n}{dt} = \vec{F} = P\left(\pi r^2\right), \tag{6.9}$$

where $\vec{V}_n$ and P are the velocity and pressure of the droplet normal to the impact surface, respectively, and r is the radius of the spreading layer defined as [8]

$$r(t) = R_m\left(1 - e^{-t/t_c}\right). \tag{6.10}$$

In Equation 6.10, R_m is the maximum spreading radius that can be expressed as [9]

$$R_m = \frac{D}{2}\sqrt{\frac{We + 12}{3(1 - cos(\theta)) + 4\left(We/\sqrt{Re}\right)}}, \tag{6.11}$$

where t_c is the characteristic spreading time, which is given as the time from initial droplet contact to maximum spreading. The value can be defined as *8D/3V* [10]. The mass of the spreading can be expressed as

$$\pi(r(t))^2 h(t)\rho\,. \tag{6.12}$$

Inserting Eqns. 10-12 into the left hand side of Equation 6.9 and simplifying,

$$P = \left|\vec{V}_n\right|\sqrt{\rho\mu}\left(\frac{2e^{-t/t_c}\sqrt{t}}{t_c\left(1 - e^{-t/t_c}\right)} + \frac{1}{2\sqrt{t}}\right). \tag{6.13}$$

The numerical simulation shown in Figure 9 demonstrates that the pressure inside the droplet increases with increasing $\vec{V}_n$. The ratio of the pressure caused by a sudden change of momentum to the shear stress caused by the surface tension shown in Equation 6.7 can be expressed as

$$P/\tau_{ST} = P/\left(\sigma/\sqrt{\nu t}\right) = \frac{\left|\vec{V}_n\right|\mu}{\sigma}\left(\frac{2e^{-t/t_c}t}{t_c\left(1-e^{-t/t_c}\right)}+\frac{1}{2}\right) \approx 2.5\frac{We_n}{Re_n} = 2.5Ca_n . \tag{6.14}$$

Figure 3 shows that the ambient pressure also affects the threshold of the splashing. Therefore, to predict the threshold of splashing ($S_{critical}$), we propose the following power law correlation, which must yield a value larger than 0.45 according to previous studies [6]:

$$S_{critical} \sim c_1(Ca_n)^{c_2}\left(\frac{p}{P_o}\right)^{c_3} > 0.45, \tag{6.15}$$

where p is the environmental gas pressure and P_o is the atmospheric pressure. Vander Wal et al. [8] found a similar splashing threshold dependence on Ca_n, with its exponent equal to 0.5. Using this value for c_2 and applying the experimental results, we obtain

$$2.84(Ca_n)^{0.5}\left(\frac{p}{P_o}\right)^{0.42} > 1. \tag{6.16}$$

Figure 11 shows the comparison of experimental results and the model predictions at atmospheric pressure. Because the threshold of splashing $2.84(Ca_n)^{0.5}\left(\frac{p}{P_o}\right)^{0.42}$ equals 1,

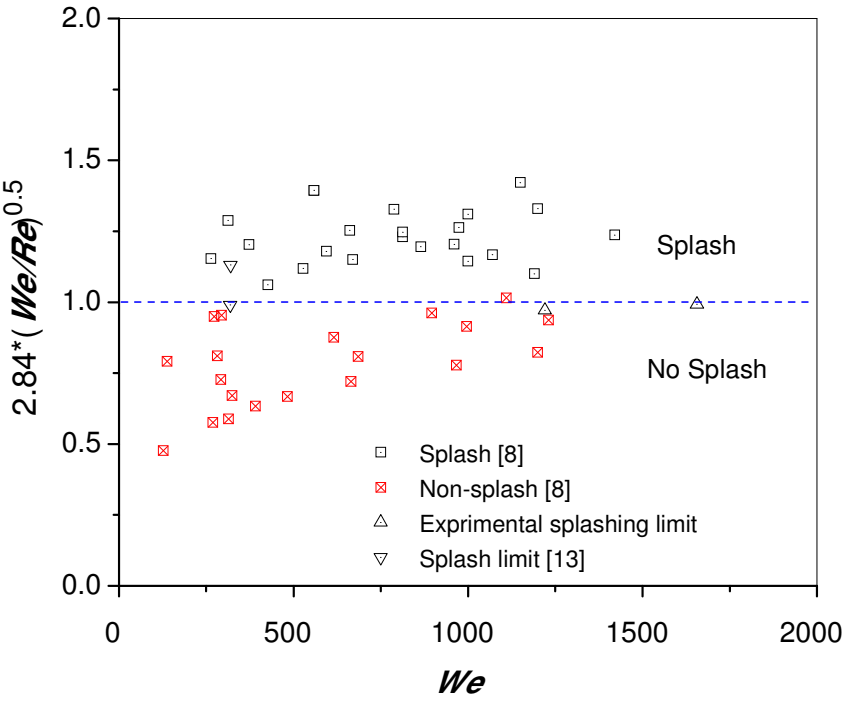

Figure 6.11: Model predicted splashing limit vs. experimental results.

the splashing and no splashing zones are clearly divided. Vander Wal et al. varied droplet diameter and fluid properties to determine the splashing threshold. As shown in Figure 11, Vander Wal's experimental data distribute evenly around the threshold of 1.

Figure 12 shows the comparison between model simulations and our experimental results of the splashing threshold as a function of normalized pressure. It shows that, for sub-atmospheric pressures, the *Ca* number for the splashing threshold drops dramatically but it decreases gradually as the pressure increases above atmospheric. For sub-atmospheric pressures, Xu's experimental data [11] also show strong agreement with the correlation proposed by Equation 6.16.

6.5.2. Kelvin-Helmholtz Instability

The mechanism of the splashing phenomenon may be explained by K-H instability theory, which occurs when shear stress is present within a continuous fluid or when there is sufficient velocity difference across the interface between two fluids [2, 12]. The dispersion relationship of K-H instability can be expressed as

$$\omega^2 = \frac{\rho_g}{\rho} V_{rel}^2 k^2 - \frac{\sigma}{\rho} k^3 , \tag{6.17}$$

where ω is the interface growth rate, k is the wave number, σ is the surface tension of the liquid. ρ and ρ_g represent the densities of the liquid and gas, respectively, and V_{rel} is the relative velocity between the liquid and ambient gas. The k corresponding to the maximum growth rate, ω_{max}, can be obtained when the derivative of k in the right side of Equation 6.17 is set to zero, and expressed as

$$k_{max} = \frac{2V_{rel}^2 \rho_g}{3\sigma} . \tag{6.18}$$

Equations 6.17 and 6.18 shows that as V_{rel} increases, both k_{max} and ω_{max} increase [2]. An analogous increase results as the ambient gas density (ρ_g) increases. Considering the ambient gas as an ideal gas, the relationship between the gas pressure and density can be expressed as

$$p = \rho_g R_u T \ , \tag{6.19}$$

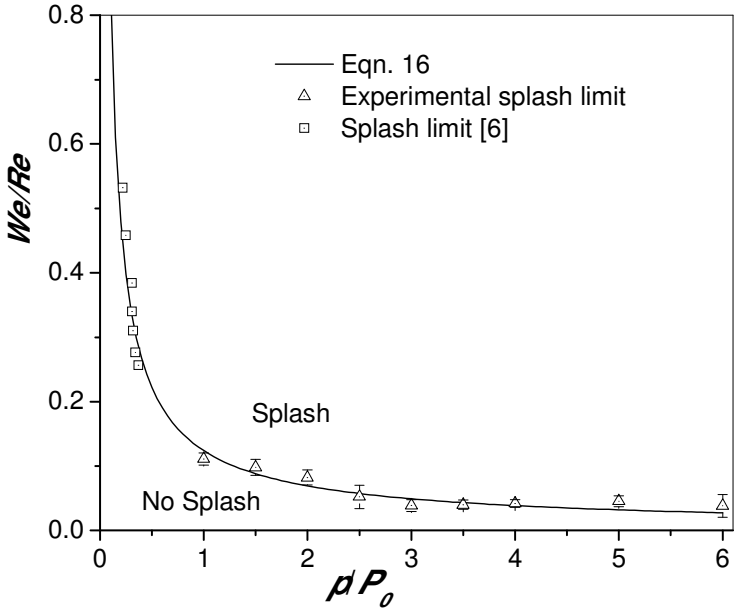

Figure 6.12: The splash limit as a function of pressure.

Thus, Equation 6.18 also illustrates that as the ambient pressure increases, the strength of the instabilities increase as well. This is congruent with experimental evidence, shown in Figures 3 and 4, that the splashing angle increases with the increase of the ambient pressure. The K-H instability is determined by the molecular force between the two fluids moving at a relative velocity. Macroscopically, this molecular force is expressed as the shear stress. As the density of the air increases, the number of air molecules in the surrounding volume increases. Inevitably, the stress increases as well. As a result, the splashing or instability increases with the increase of the ambient gas pressure, as observed in our experiments.

An apparent paradox appears in Figures 5 and 6, which show that as the inclined angle increases, the splashing weakens, although the spreading velocities (V_{rel}) increases in the

downhill direction. According to Equation 6.18, instabilities or splashing at 45^o should be stronger than that at 15^o under the assumption that the velocity of the ambient gas during droplet impact is 0 and V_{rel} is the spreading velocity parallel to the impact surface [13, 14].

This apparent paradox may be reconciled by examining Figures 7 and 8. Clearly the velocity of the ambient air near the droplet impact area is much greater than the spreading velocity. Also, the ambient air moves at a certain angle with respect to the impact surface and thus can have velocity normal to the impact surface. Furthermore, for the same impact velocity, the angle of the ambient air velocity vector increases as the ambient pressure increases (Figures 7a and 7b). Therefore, with the understanding of ambient air movement, V_{rel} not only provides a reasonable solution to the above paradox, but it also explains why the splashing droplets move at an inclined angle relative to the impact surface, which varies with ambient pressure (Figure 4).

The K-H instability analysis (Equation 6.18) not only provides a better explanation of the mechanism of splashing, but it also shows good agreement with the splashing threshold correlation analysis shown by Equation 6.16. First, both analyses show that as the surface tension decreases, the possibility of splashing increases. Namely, with decreasing σ, k_{max} increases (see Equation 6.18) as well as the value of $2.84(Ca_n)^{0.5}\left(\frac{p}{P_o}\right)^{0.42}$. Conversely, with increasing ρ_g, k_{max} increases (see Equation 6.18) and so does the value of

$2.84(Ca_n)^{0.5}\left(\frac{p}{P_o}\right)^{0.42}$. Finally, though the quantitative relationship between V_{rel} and $\vec{V}_n$ cannot be directly determined from Equations 6.18 and 6.16, the results of our numerical simulations (Figures 7 and 8) show that as $\vec{V}_n$ increases, V_{rel} increases as well.

6.6 Conclusions

1. The threshold of splashing on a smooth, flat surface has been examined under a wide *We* range under varying air pressures and oblique impact angles. Increasing *We* increases the magnitude of splashing, confirming the results of previous studies. The effect of air pressure on splashing, first studied by Xu [6, 11], has been verified to extend into super-atmospheric conditions. Increasingly oblique impact angles appeared to reduce splashing.

2. A new semi-empirical splash threshold correlation was derived, considering the internal pressure generation during droplet impact and the opposing, retentive surface tension. The correlation is similar in form to Vander Wal's [8] but extends the range of applicability to non-atmospheric air pressures. The decrease in splashing observed in oblique impacts is accounted for by using $\vec{V}_n$.

3. According to Xu's results, splashing should increase with increasing spreading velocity, V_s. However, our experimental evidence demonstrated that with increasingly oblique impact angles, spreading velocity increases, but splashing

reduces. This apparent paradox is resolved by our re-examination of K-H instability theory and numerical analyses, which shows that the occurrence of splashing is more attributable to V_{rel}, the relative velocity between air and the spreading droplet, rather than V_s alone. Thus the air motion initiated by the impacting droplet cannot be neglected. V_{rel} appears to scale well with $\bar{V}_n$ used in our correlation, though a direct quantitative relation was not obtained.

References

1. Li, X.Y., X.H. Ma, and Z. Lan, *Behavioral Patterns of Drop Impingement onto Rigid Substrates with a Wide Range of Wettability and Different Surface Temperatures.* Aiche Journal, 2009. **55**(8): p. 1983-1992.
2. Jepsen, R.A., S.S. Yoon, and B. Demosthenous, *Effects of air on splashing during a large droplet impact: Experimental and numerical investigations.* Atomization and Sprays, 2006. **16**(8): p. 981-996.
3. Fujimoto, H., et al., *Three-dimensional numerical analysis of the deformation behavior of droplets impinging onto a solid substrate.* International Journal of Multiphase Flow, 2007. **33**(3): p. 317-332.
4. Harlow, F.H. and J.P. Shannon, *Splash of a Liquid Drop.* Journal of Applied Physics, 1967. **38**(10): p. 3855-&.
5. Engel, O.G., *Waterdrop Collisions with Solid Surfaces.* Journal of Research of the National Bureau of Standards, 1955. **54**(5): p. 281-298.
6. Xu, L., W.W. Zhang, and S.R. Nagel, *Drop splashing on a dry smooth surface.* Physical Review Letters, 2005. **94**(18): p. 505-516.
7. Levin, Z. and P.V. Hobbs, *Charge Separation Due to Splashing of Water Drops.* Bulletin of the American Meteorological Society, 1970. **51**(6): p. 577-&.
8. Vander Wal, R.L., G.M. Berger, and S.D. Mozes, *The splash/non-splash boundary upon a dry surface and thin fluid film.* Experiments in Fluids, 2006. **40**(1): p. 53-59.

9. Pasandideh-Fard, M., et al., *Splat shapes in a thermal spray coating process: Simulations and experiments.* Journal of Thermal Spray Technology, 2002. **11**(2): p. 206-217.

10. Pasandideh-Fard, M., et al., *Deposition of till droplets on a steel plate: simulations and experiments.* International Journal of Heat and Mass Transfer, 1998. **41**(19): p. 2929-2945.

11. Xu, L., *Liquid drop splashing on smooth, rough, and textured surfaces.* Physical Review E, 2007. **75**(5): p. 26-28.

12. Yoon, S.S. and P.E. DesJardin, *Modelling spray impingement using linear stability theories for droplet shattering.* International Journal for Numerical Methods in Fluids, 2006. **50**(4): p. 469-489.

13. Rioboo, R., et al., *Experimental evidence of liquid drop break-up in complete wetting experiments.* Journal of Materials Science, 2006. **41**(16): p. 5068-5080.

14. Sikalo, S., C. Tropea, and E.N. Ganic, *Dynamic wetting angle of a spreading droplet.* Experimental Thermal and Fluid Science, 2005. **29**(7): p. 795-802.

CHAPTER 7: The Effects of Liquid Viscosity on Droplet Corona Splashing

Nomenclature

C_G	sound speed in ambient gas
D	droplet diameter
M_G	molecular weight of the gas
Oh	Ohnesorge number = $We^{0.5}/Re$
P	ambient gas pressure
P_o	atmospheric pressure [1 atm]
Re	Reynolds number ($\rho VD/\mu$)
R_u	universal gas constant [8314 N m/kgmol K]
t	time from droplet impact
T	temperature
V	droplet impact velocity
V_s	spreading velocity
We	Weber number ($D\rho V^2/\sigma$)

Greek symbol

γ	adiabatic gas constant
μ	dynamic viscosity
ν	kinematic viscosity
ρ	liquid density
ρ_G	ambient gas density
σ	surface tension

7.1 Introduction

The ability to accurately predict the occurrence of splashing of single droplet impacts remains of interest due to a number of important applications including materials processing, ink printing, spray cooling, fuel injection, fire suppression and irrigation. Many mechanisms for splashing have been proposed, however a complete picture of the

phenomenon is yet unattained. The phenomenon was first studied by Worthington [1]. Since then, many mechanisms have been proposed to explain splash formation. At high droplet impact velocities over 100 m/s, an internal pressure shockwave may form to initiate splashing [2-6]. At lower velocities, splashing may still be initiated through a redirection of spreading momentum to the location of lowest surface energy [7-9]. Surface roughness plays an important role by obstructing the flow of momentum along the impact surface, forcing a redirection vertically. Splashing of this form has been referred to as "prompt" splashing [10]. However, splashing may also take place on smooth surfaces, though of a distinctly different nature. Splashing of this type is labeled "corona" splashing because of the distinct crown shape that forms at the leading edge of spreading [10] It is this, lesser-studied mechanism of splashing that we examine further in this paper.

Allen [11, 12] applied Rayleigh-Taylor (R-T) instability theory to demonstrate that splashing on smooth surfaces was one of the products of instability formation. Recent research, however, has shown that Kelvin-Helmholtz (K-H) instability, which is caused by the shear stress between two fluids moving in parallel at a relative velocity, may also contribute to splashing [13-15]. According to K-H instability, the shear stress between the droplet and the surrounding gas becomes a determining parameter during splashing. Therefore, the surrounding gas density, or pressure, would influence splashing. In a recent study, Xu et al. provided supporting evidence for this claim by discovering that as the ambient pressure drops to 0.17 atm, splashing was suppressed [16]. Further description of the interaction between a water droplet and ambient gas during impact was

presented by Jepsen et al. [17], who used the Schlieren photography method to provide experimental evidence of gas movement, which varied with the ambient pressure during a water slug impact onto a solid surface. Recently, Liu et al. [18] (Chapter 6) confirmed the validity of this effect under super-atmospheric conditions.

Many experimental correlations exist to predict the quantitative threshold of splashing during droplet impact and most are based on the Weber number (*We*) and the Reynolds number (*Re*) or some combination of the two [8, 18-21]. These studies have related the threshold of splashing to liquid properties, most importantly the surface tension and viscosity, droplet size and velocity, and to the impact surface characteristics. These correlations often have applicability limited to the narrow physical domains used to derive them, limiting their usefulness. Correlations may often be divided into those that predict a direct relationship between droplet viscosity and splashing [8, 21] and those that predict an inverse relationship [16, 18-20]. Clearly these correlations would thus diverge widely in their splash predictions through a broad range of fluid properties. Most of these correlations also do not consider the effect of air pressure on splashing. Thus, broader experimental data sets are required for deeper understanding of the physical mechanisms of splashing to aide in the development of more universal predictive schemes.

In this study, some droplet splash threshold correlations for impact onto smooth surfaces are reviewed and evaluated for their range of applicability. With the use of an experimental pressure chamber and varying fluid properties, we provide new experimental data. Fluid viscosity, in particular, is examined through a wide *Re* range to

determine its effect on splashing. The results are fairly robust predictors of single droplet splashing on smooth, dry surfaces and a deeper understanding of the physical processes involved.

Table 7.1. Relevant properties of fluids tested.

	ρ [kg/m^3]	μ [Pa s]	σ [N/m]
FC-72	1680	0.00064	0.012
Water	998	0.001	0.0728
50% Water-glycerol	1126	0.006	0.0674
40% Water-glycerol	1154	0.0108	0.0669
30% Water-glycerol	1181	0.0225	0.0665
20% Water-glycerol	1209	0.0601	0.0657
15% Water-glycerol	1223	0.1065	0.0652
10% Water-glycerol	1235	0.219	0.0645
Glycerol	1260	1.41	0.0633

7.2 New Measurements of Splash Threshold

To supplement available existing experimental data [16, 19, 22], additional droplet impact measurements were performed using FC-72 and aqueous glycerol mixtures ranging from 0-100%. Fluid properties are provided in Table 1. The selection of these fluids provides a wide range of fluid viscosity. A precision pneumatic micro-liter valve with stainless steel tips of various outer diameters was used to generate droplets of 1.5-3.8 mm diameter. The distance from the nozzle tip to the impact surface was varied from 0.051 to 0.82 m using an adjustable tower to produce impact velocities from 1 to 5 m/s. A smooth Plexiglas surface with less than 0.8 μm in roughness was used as the impact

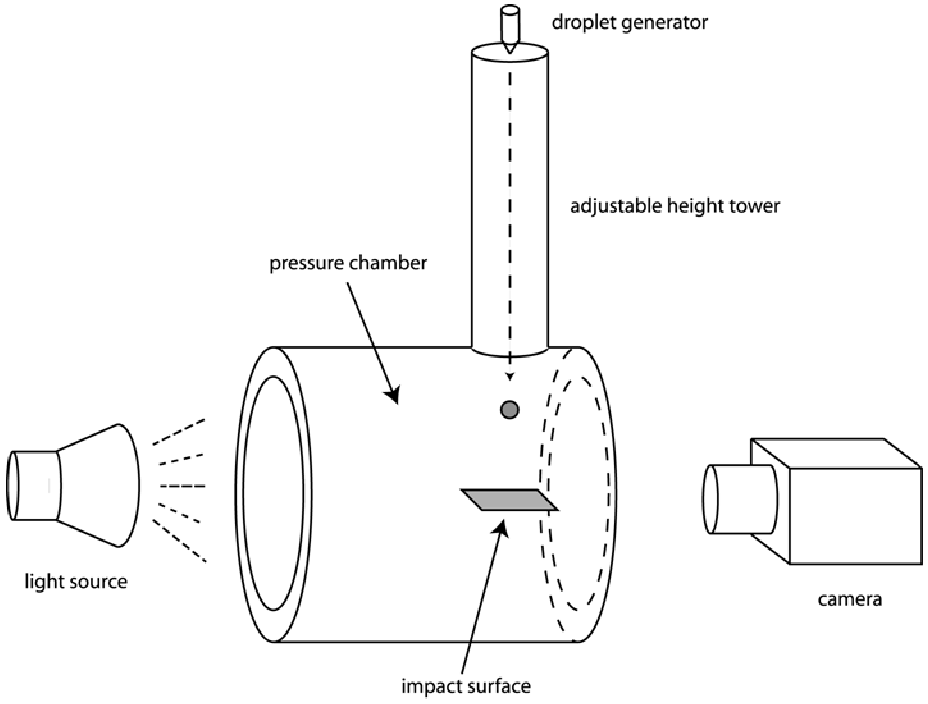

Figure 7.1: Schematic of the experimental apparatus.

surface. All experiments were performed isothermally at room temperature and within a custom-made aluminum pressure chamber (Figure 7.1) to vary ambient pressure from 0.3-6 atm. Clear polycarbonate windows permitted imaging of the impact phenomena with a Phantom V7.1 high-speed camera set at 10000 fps. Images were backlit with a high-power tungsten lamp with light diffuser.

Impact outcomes for each of the tested cases were verified by repeating each case at least once. For cases of questionable outcomes or high variability, more measurements were taken and the results averaged. Threshold cases where splashing and non-splashing occurred equally are designated as “T”.

7.3 Viscosity and Splashing

Figure 7.2 shows the changes in impact dynamics as *Re* and *We* are changed at 3 atm. This pressure was chosen because the results are qualitatively clearer than those seen at other pressures. Here, *Re* and *We* are used as non-dimensional representations of fluid viscosity and surface tension. The conditions shown are, from left to right: (a) water at 2.5 m/s, (b) water at 3.5 m/s, (c) 50% water-glycerol at 3.5 m/s, and (d) 10% water-glycerol at 3.5 m/s. The corresponding *Re* and *We* are given below the figure with dimensionless times defined as *tV/D* given in each frame. Splashing does not occur for the water droplet impacting at 2.5 m/s. But as impact velocity and thus *We* is increased, some splashing becomes visible at a time of 0.2 after impact (Figures 7.2a and 7.2b). Interestingly, as *Re* is decreased significantly for the 50% water-glycerol with *We* remaining fairly constant, splashing quantity is increased dramatically (Figures 7.2b and 2c). Further decrease in *Re* by increasing viscosity with a 10% water-glycerol solution, however, inhibits splashing and spreading completely (Figure 7.2c and 7.2d). Clearly, a non-obvious combination of *Re* and *We* exists that minimizes the impact energy required for splashing. Figure 7.3 further reinforces this notion for atmospheric conditions by revealing that the *We* required for splashing reaches a minimum in the *Re* range of approximately 100-500 for water-glycerol mixtures. Outside this range, the impact energy required for splashing is higher. The threshold space is defined for the region between splashing and non-splashing. For highly viscous mixtures with *Re* below 100, splashing could not be achieved within the limits of the experimental apparatus so a projected threshold region is proposed.

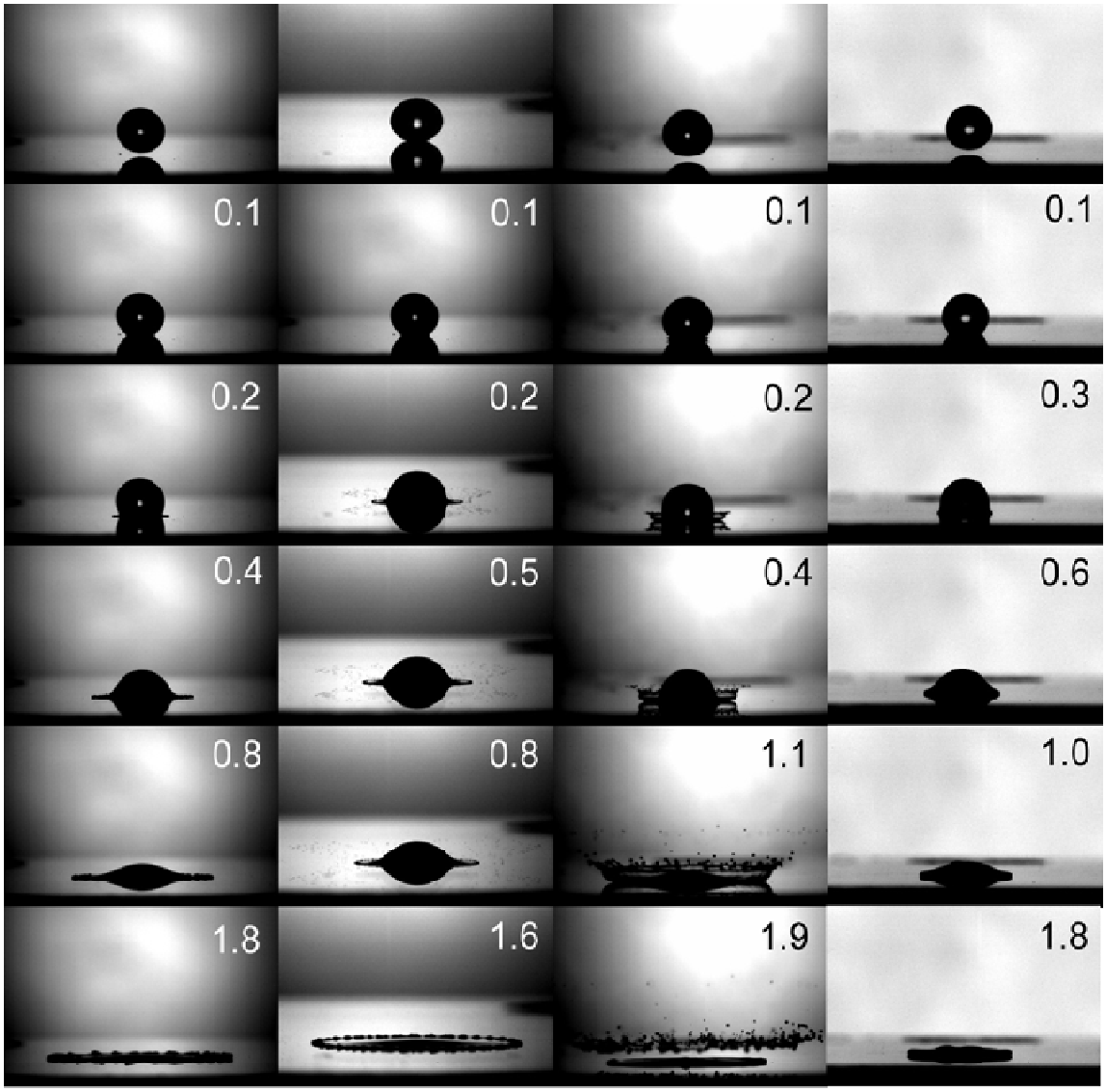

Figure 7.2: Changing splashing characteristics through a range of *Re* and *We* using aqueous glycerol solutions at 3 atm. The inset numbers are dimensionless times from impact.

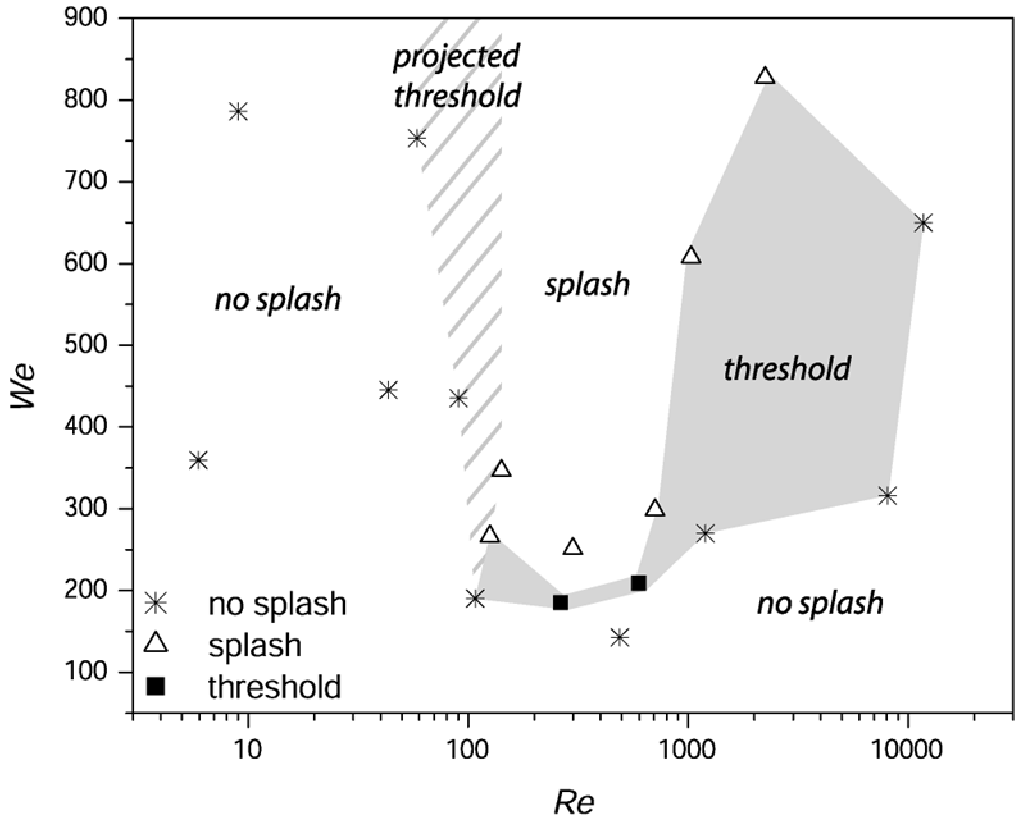

Figure 7.3: Changes in impact energy (*We*) required for splashing as a function of *Re* at 1 atm.

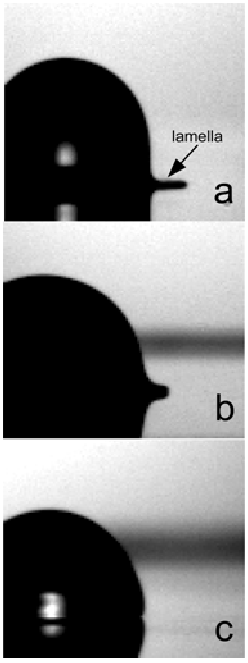

Figure 7.4: A spreading lamella thickness comparison at a dimensionless time of approximately 0.2 after impact for (a) water, (b) 50% water-glycerol and (c) glycerol.

A closer look at the impact dynamics reveals some of the effects of increasing viscosity. As shown in Figure 7.4, the spreading lamella appears to increase in thickness as the fluid viscosity increases. In effect, viscosity may destabilize the lamella by increasing its thickness and reducing the cohesive effect of surface tension. However, the opposing effect of slowing splashing dynamics also occurs with increasing viscosity. Evidence for this may be seen in the 15% water-glycerol solution, as time of actual satellite droplet formation appears to be significantly delayed relative to the 50% water-glycerol solution from time of impact, occurring at the location of maximum spreading (Figure 7.5). A suppressive mechanism of viscosity may thus be to delay the onset of splashing beyond a certain time window of opportunity. Much of the splashing data for the 15% water-

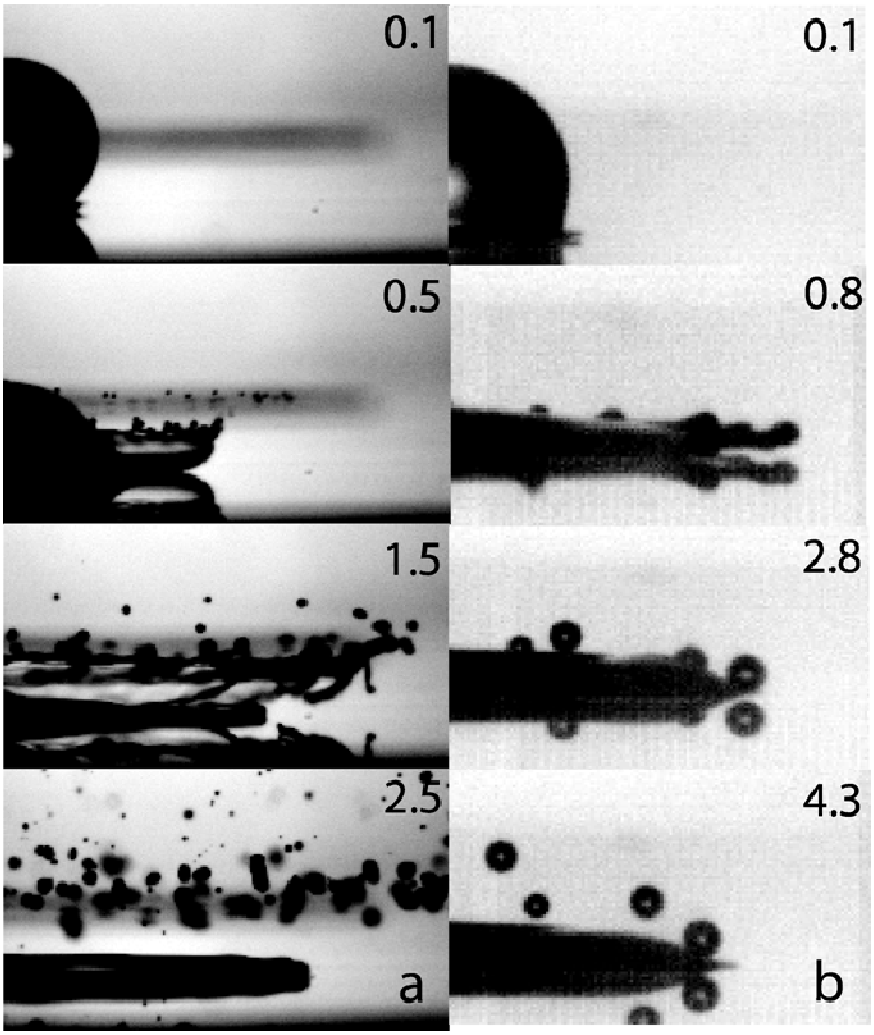

Figure 7.5: A comparison of crown formation and break up times relative to spreading in (a) 50% Water-glycerol at 3 atm and (b) 15% Water-glycerol at 5.5 atm. Dimensionless times from impact are provided.

glycerol solution is inconsistent, and this may be an indication that the growth rate of instabilities is bordering at this time threshold of opportunity.

7.4 Re-Evaluation of Existing Splash Criteria

In a recent work, Xu et al. [16] identified the influence of the surrounding gas pressure on splashing by suggesting K-H instability [23] as the initiating mechanism. The stress of the surrounding compressible gas on the droplet is characterized as:

$$\Sigma_G \sim (\rho_G)(C_G)(V_S) \sim \frac{PM_G}{k_B T}\sqrt{\frac{\gamma R_U T}{M_G}}\sqrt{\frac{DV_o}{4t}} \tag{7.1}$$

where C_G is the speed of sound in the gas, V_s is the droplet spreading velocity, γ is the adiabatic constant of the gas, and R_U is the universal gas constant. In opposition to the gas stress is the surface tension of the liquid, which works to keep the liquid together:

$$\Sigma_L = \frac{\sigma}{l} = \frac{\sigma}{\sqrt{\upsilon_L t}} \tag{7.2}$$

where l is the thickness of the spreading lamella on the substrate surface. The ratio of these two defines the threshold of splashing:

$$\frac{\Sigma_G}{\Sigma_L} = \frac{\rho_G C_G}{\rho_L V_o} We\, Re^{-0.5} \geq 0.9 \tag{7.3}$$

It was argued that the droplet viscosity facilitated splashing by thickening the lamella, as shown experimentally in Section 3, therefore destabilizing it to the shearing from the

upwardly-directed eddies produced in the gas phase. Equation 7.3, however, does not capture the effect of splash retardation at high viscosity, as evidenced by comparison with the new high-viscosity data in Figure 7.6a. Using a threshold value of 0.9, the correlation gets progressively worse with decreasing *Re*. Significant hysteresis is also evident between data sets of different experimenters. In Figure 7.6b, Equation 7.3 is accurate for threshold data of Xu used to derive it, but appears to fail for most data from Vander Wal et al. [19] which seems to converge around a threshold of 1.5. Because of the varied chemical compositions of the fluids used by Vander Wal, with many of a hydrophobic nature, a wettability effect with the impact surface may be present which is also not captured by Equation 7.3. Intuitively, fluids with a greater affinity to the impact surface should require a higher threshold value to splash.

Other researchers have attempted to develop empirical splash correlations based on relevant dimensionless parameters [19, 21]. Frequently the threshold of splashing was delineated in *Oh* vs. *Re* space. Mundo et al. [21] developed a correlation using various water-sucrose-ethanol mixtures:

$$57.7 = Oh \cdot \mathrm{Re}^{1.25} = \frac{\mu}{\sqrt{\rho\sigma d}} \frac{(\rho u d)^{1.25}}{\mu^{1.25}} = \frac{(\rho u d)^{0.75} u^{1.25}}{\sigma^{0.5} \mu^{0.25}} \tag{7.4}$$

where values above the constant of 57.7 denoted splashing. More recently, Vander Wal et al. [19] developed their own, albeit slightly different, functional dependence:

$$0.35 = Oh\sqrt{Re} = \frac{\mu}{\sqrt{\rho\sigma d}} \sqrt{\frac{\rho u d}{\sigma}} = \sqrt{\frac{\mu u}{\sigma}} \tag{7.5}$$

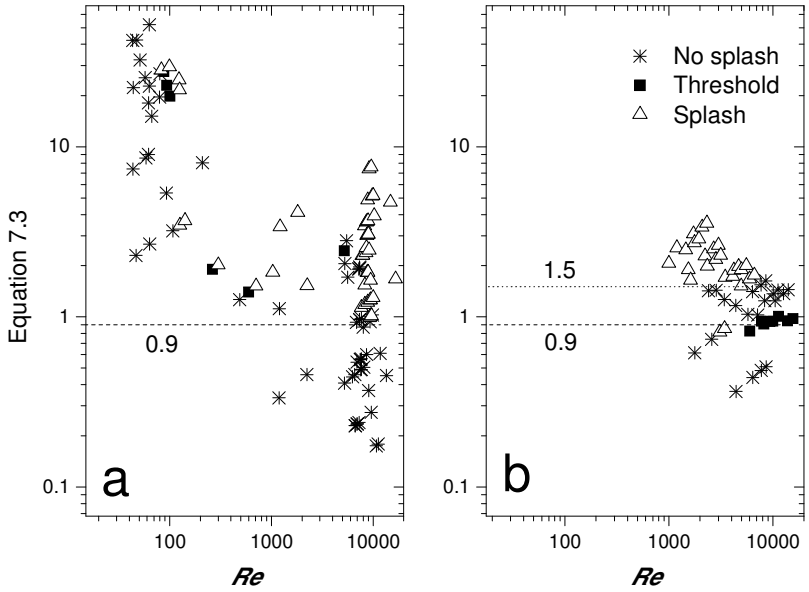

Figure 7.6: Evaluation of Equation 3 with (a) present data and (b) data from Vander Wal [19] (no splash and splash cases) and Xu [16] (threshold cases).

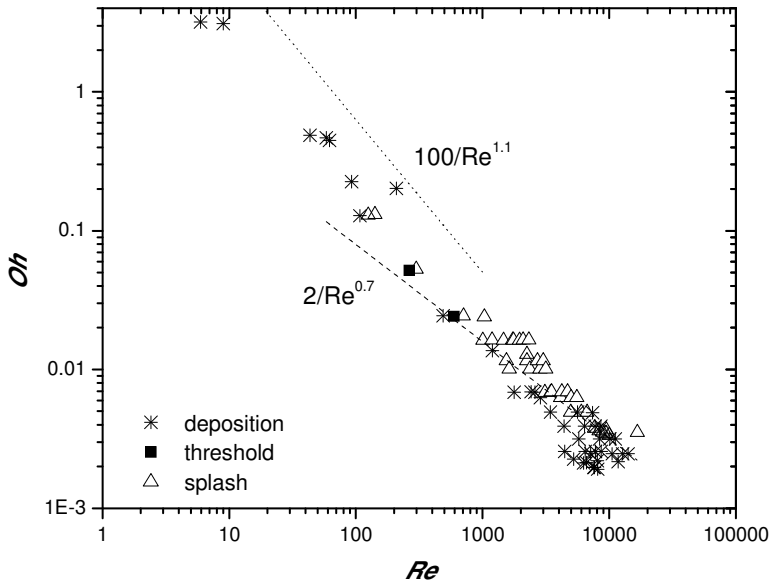

Figure 7.7: Evaluation of *Oh* vs. *Re* correlations using current experimental data at atmospheric pressure and data from Vander Wal [19].

These correlations, though similar in form, have an important distinction in their relation with viscosity. In Equation 7.4, splashing diminishes with increasing liquid viscosity, whereas the opposite is true for Equation 7.5 and likewise Equation 7.3. Clearly an expression in the form of Equation 7.4 would work in the high viscosity or low *Re* range and vice versa for Equation 7.5. As shown in Figure 7.7, with some modification to the exponents to fit the present data due to hysteresis, expressions of the form of Equations 7.4-5 appear to capture the threshold of splashing through a wide *Re* range, though the exact location of the threshold at low *Re* cannot be determined due to lack of splashing data at atmospheric pressure. These correlations are limited by the fact that they do not consider the effect of the surrounding ambient pressure, which clearly affects splashing [16, 18].

7.5 New Predictors of Splashing

Because of the limitations in the analytical derivation of Xu's correlation, an attempt will be made to correlate the corona splash threshold in *Oh* vs. *Re* space of the form $C(Oh \cdot Re^{a})$. The robustness of these types of correlations makes them attractive for practical prediction of splashing. Along the lines of Chapter 6, the effect of the surrounding air pressure may be captured by the addition of a pressure term [18]:

$$C\left(Oh \cdot \mathrm{Re}^{a}\right)\left(\frac{P}{P_{atm}}\right)^{b} = 1 \tag{7.6}$$

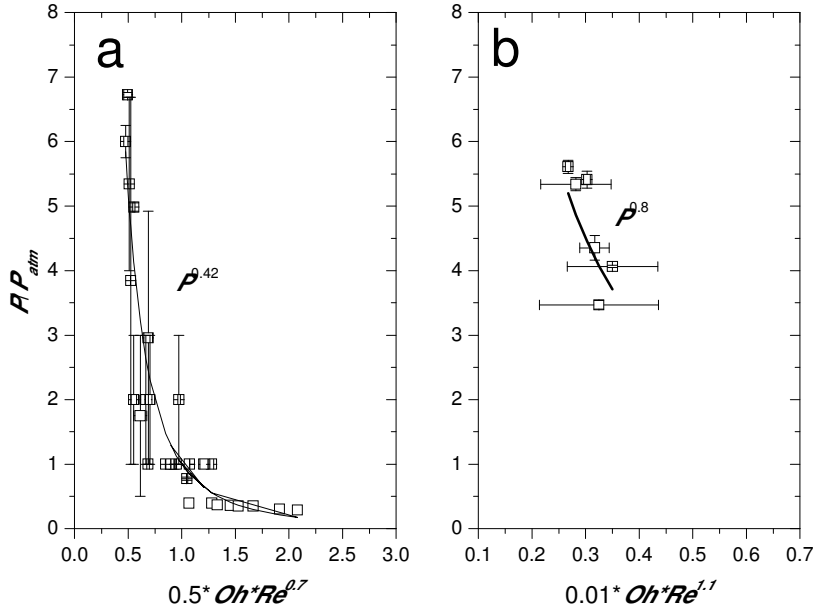

Figure 7.8: Determination of *P* exponent using estimated threshold data for (a) low viscosity and (b) high viscosity data.

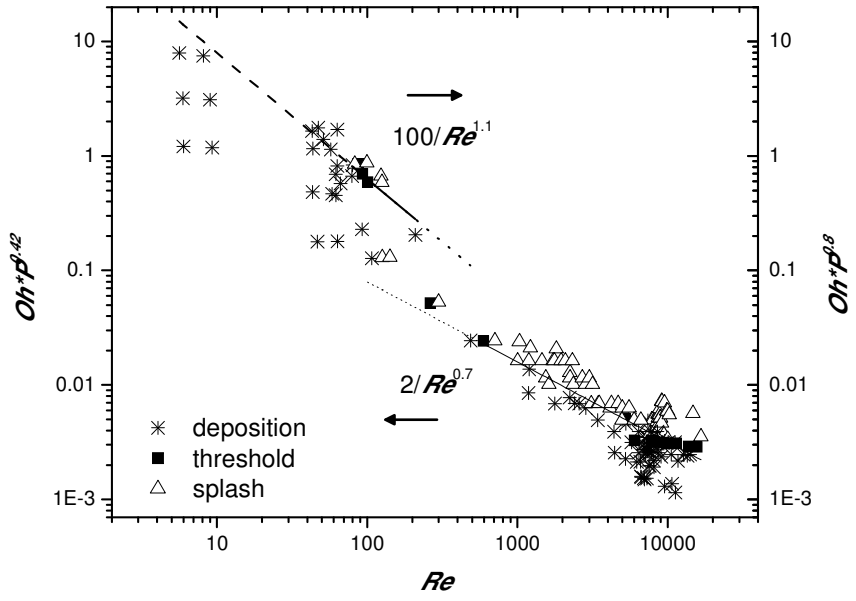

Figure 7.9: Final data fit through entire *Re* range using all available experimental data.

Using the parameters found in the previous section for low and high *Re*, the expressions are fitted to approximate threshold pressure values to determine *b* as shown in Figure 7.8a and 7.8b. These threshold values are determined by averaging adjacent splashing and non-splashing data points with error bars representing the uncertainty in the exact location of the threshold. Data at high *Re* above ~3000 show a dependence of $P^{0.42}$, confirming the earlier study [18]. At low *Re*, a dependence of $P^{0.8}$ is shown.

The end result is evaluated for all data points at all tested pressures in Figure 7.9. As one can see, a region of ambiguity exists for *Re* of approximately 100-500, with data points appearing to follow both expressions. Also for very low *Re* below 80, the threshold of splashing appears to increase sharply, though the exact location cannot be determined as splashing is not possible within the limitations of the experimental apparatus. Below that, and analogous to the atmospheric only data, significant changes appear to occur in the physics of droplet impact that may make it nearly impossible for splashing to occur. With this exception and for most practical *Re*, splashing may be predicted adequately by Equation 7.6 by adjusting *C*, *a* and *b* to the appropriate values given in the figure.

A time scale analysis during droplet impact provides a plausible explanation for the lower *Re* limit of splashing. Figures 7.10a and 7.10b depict the scales involved during droplet impact. If we assume that the spreading lamella moves at approximately the impact velocity, *V*, then we may represent the droplet impact with a characteristic time scale of D/V. A viscous diffusive time scale may be represented as D^2/ν. Taking the ratio of these times is simply *Re*. *Re* itself, therefore, represents a time window of opportunity for

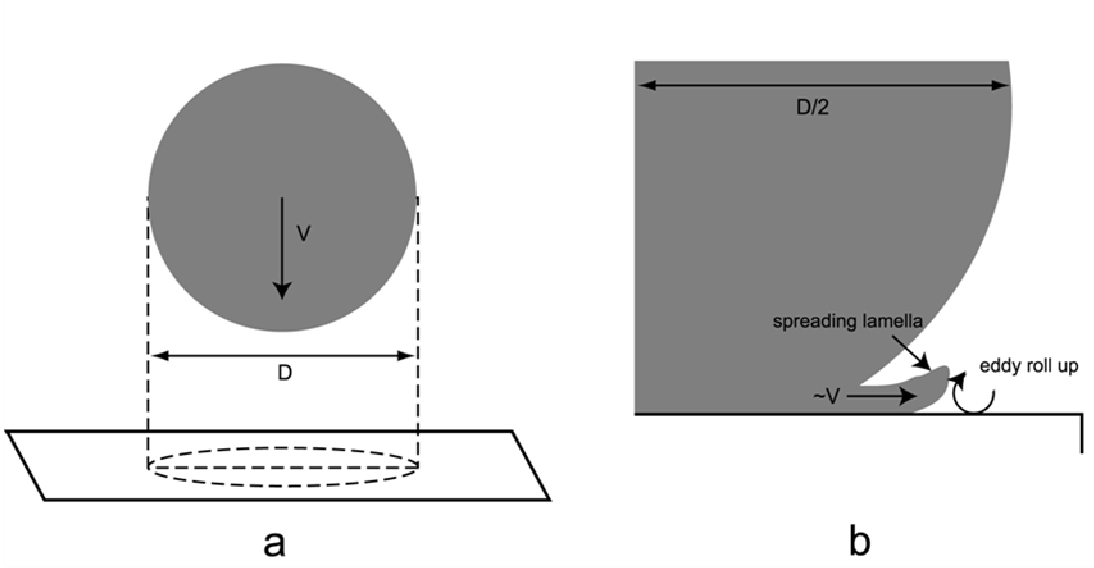

Figure 7.10: Schematic of a droplet approaching impact (a) and post-impact with lamella spreading and lifting (b) with relevant scales for time window for splashing.

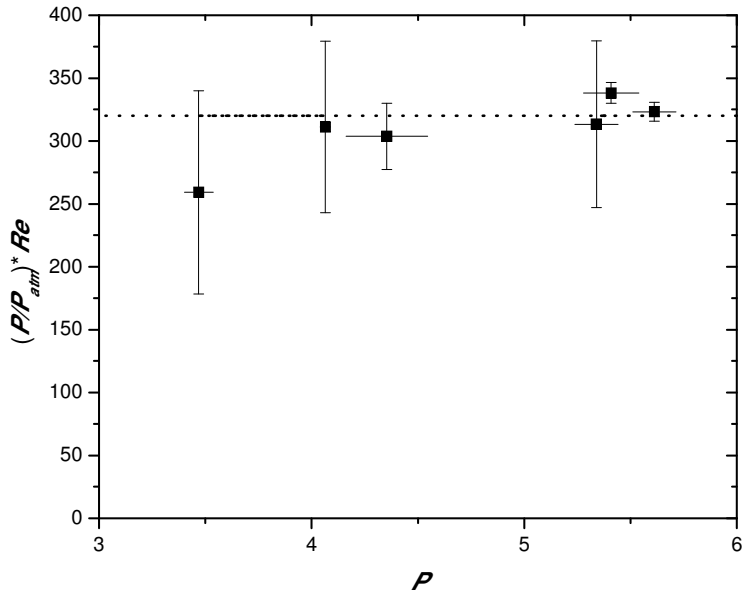

Figure 7.11: The time window value showing a constant value of ~320 for 15% Water-glycerol mixture.

splashing and may explain why splashing becomes increasingly more difficult for low *Re*. The effect of ambient pressure on this time window may be accounted for by adding the pressure dependence determined for high viscosity (Figure 7.8b):

$$\left(\frac{P}{P_{atm}}\right)^{0.8} Re \sim O\left(10^2\right) \tag{7.7}$$

Values for Equation 7.7 are given at threshold values for high viscosity at different pressures in Figure 7.11 and indicate a fairly constant value of about 320. This further supports the notion of a time window of opportunity for splashing. Droplets therefore must satisfy both kinetic and time requirements for splashing, as illustrated in Figure 7.12 for low *Re* fluids.

7.6 Conclusions

Corona splashing on smooth, dry surfaces was studied by examining the influence of droplet viscosity with changing air pressure. New results are presented and reveal a range of *Re* from 100-500 where minimum impact energy is required to induce splashing. Viscosity has the opposing effects of increasing the thickness of the spreading lamella, making it more unstable to surrounding airflow, and slowing the splashing dynamics. By dividing the physical domain into low (*Re*<500) and high viscosity (*Re*>500) regions, splash threshold correlations based on *Oh* and *Re* are fairly robust, fitting a wide variety of liquids and surrounding air pressures, though some ambiguity exists within the transition region.:

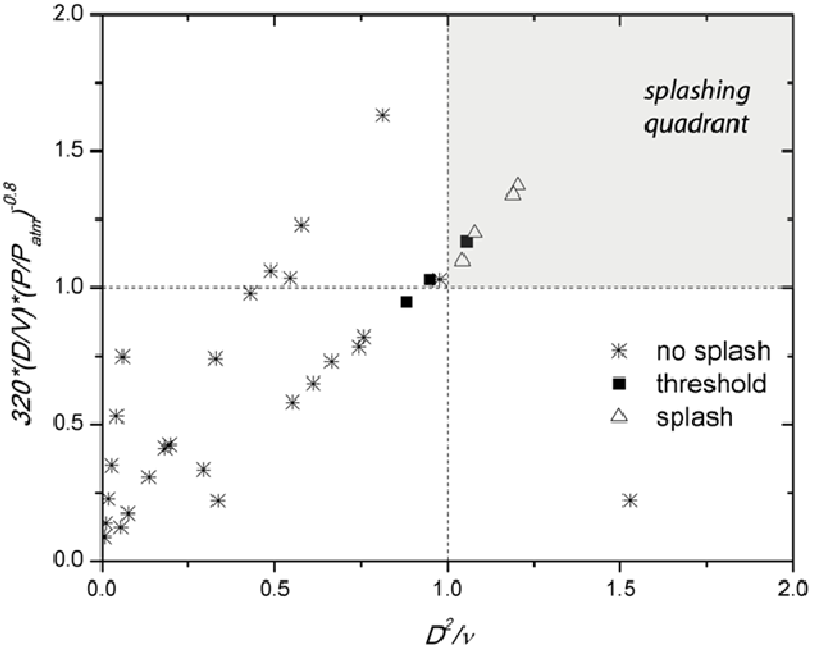

Figure 7.12: Evaluation of both the kinetic and time requirements for splashing for low *Re* droplets. Data in the splashing quadrant satisfies both requirements.

$$0.5\left(Oh \cdot Re^{0.7}\right)\left(\frac{P}{P_{atm}}\right)^{0.42} = 1 \qquad (100<Re<17000)$$

$$0.01\left(Oh \cdot Re^{1.1}\right)\left(\frac{P}{P_{atm}}\right)^{0.8} = 1 \qquad (80<Re<500)$$

Below about *Re*=80, splashing could not be induced within the limitations of the experimental apparatus. A time scale argument was presented to provide a plausible explanation for this lower limit on splashing:

$$\left(\frac{P}{P_{atm}}\right)^{0.8} Re \sim 320 \qquad (Re<500)$$

So, though certain low *Re* impact scenarios may inherently have sufficient energy to induce splashing, their high viscosities limit the growth rate of instabilities to beyond a window of opportunitiy. Future work would require additional experimental data to supplement existing data and to examine causes of data hysteresis, such as varying fluid affinity to the impacting surface. A complete analytical description of corona splashing has not yet been attained, but the empirical correlations developed here may be practically useful.

References

1. Worthington, A., *On the froms assumed by drops of liquids falling vertically on a horizontal plate.* Proc. R. Soc. London, 1876. **25**: p. 261-271.
2. Bowden, F.P. and J.E. Field, *Brittle Fracture of Solids by Liquid Impact by Solid Impact + by Shock.* Proceedings of the Royal Society of London Series a-Mathematical and Physical Sciences, 1964. **282**(139): p. 331-&.
3. Hobbs, P.V. and T. Osheroff, *Splashing of Drops on Shallow Liquids.* Science, 1967. **158**(3805): p. 1184-&.
4. Levin, Z. and P.V. Hobbs, *Splashing of Water Drops on Solid and Wetted Surfaces - Hydrodynamics and Charge Separation.* Philosophical Transactions of the Royal Society of London Series a-Mathematical and Physical Sciences, 1971. **269**(1200): p. 555-&.
5. Lesser, M.B. and J.E. Field, *The Impact of Compressible Liquids.* Annual Review of Fluid Mechanics, 1983. **15**: p. 97-122.
6. Field, J.E., *ELSI conference: invited lecture - Liquid impact: theory, experiment, applications.* Wear, 1999. **235**: p. 1-12.
7. Harlow, F.H. and J.P. Shannon, *Distortion of a Splashing Liquid Drop.* Science, 1967. **157**(3788): p. 547-&.
8. Stow, C.D. and M.G. Hadfield, *An Experimental Investigation of Fluid-Flow Resulting from the Impact of a Water Drop with an Unyielding Dry Surface.* Proceedings of the Royal Society of London Series a-Mathematical Physical and Engineering Sciences, 1981. **373**(1755): p. 419-441.

9. Range, K. and F. Feuillebois, *Influence of surface roughness on liquid drop impact.* Journal of Colloid and Interface Science, 1998. **203**(1): p. 16-30.

10. Rioboo, R., C. Tropea, and M. Marengo, *Outcomes from a drop impact on solid surfaces.* Atomization and Sprays, 2001. **11**(2): p. 155-165.

11. Allen, R.F., *The Mechanics of Splashing.* Journal of Colloid and Interface Science, 1988. **124**(1): p. 309-316.

12. Allen, R.F., *Role of Surface-Tension in Splashing.* Journal of Colloid and Interface Science, 1975. **51**(2): p. 350-351.

13. Kim, H.Y., Z.C. Feng, and J.H. Chun, *Instability of a liquid jet emerging from a droplet upon collision with a solid surface.* Physics of Fluids, 2000. **12**(3): p. 531-541.

14. Yoon, S.S. and P.E. DesJardin, *Modelling spray impingement using linear stability theories for droplet shattering.* International Journal for Numerical Methods in Fluids, 2006. **50**(4): p. 469-489.

15. Yoon, S.S., et al., *Experimental investigation on splashing and nonlinear fingerlike instability of large water drops.* Journal of Fluids and Structures, 2007. **23**(1): p. 101-115.

16. Xu, L., *Liquid drop splashing on smooth, rough, and textured surfaces.* Physical Review E, 2007. **75**(5): p. 056316-1-8.

17. Jepsen, R.A., S.S. Yoon, and B. Demosthenous, *Effects of air on splashing during a large droplet impact: Experimental and numerical investigations.* Atomization and Sprays, 2006. **16**(8): p. 981-996.

18. Liu, J., et al., *Splashing phenomena during liquid droplet impact.* Atomization and Sprays, 2010. **(in press)**.

19. Vander Wal, R.L., G.M. Berger, and S.D. Mozes, *The splash/non-splash boundary upon a dry surface and thin fluid film.* Experiments in Fluids, 2006. **40**(1): p. 53-59.

20. Bird, J.C., S.S.H. Tsai, and H.A. Stone, *Inclined to splash: triggering and inhibiting a splash with tangential velocity.* New Journal of Physics, 2009. **11**.

21. Mundo, C., M. Sommerfeld, and C. Tropea, *Droplet-Wall Collisions - Experimental Studies of the Deformation and Breakup Process.* International Journal of Multiphase Flow, 1995. **21**(2): p. 151-173.

22. Liu, J., et al. *Splashing phenomena during liquid droplet impact*. in *ILASS Americas, 21th Annual Conference on Liquid Atomization and Spray Systems*. 2008. Orlando, FL.

23. Acheson, D.J., *Elementary fluid dynamics*. Oxford applied mathematics and computing science series. 1990, Oxford; New York: Clarendon Press ; Oxford University Press.

CHAPTER 8: Droplet Spreading Dynamics and Splashing

My previous efforts in droplet splashing research yielded some interesting results, but many questions remain as to the actual physics behind droplet splashing. Here I borrow from some recent theoretical advancement in spray formation to present a more in-depth analysis of what causes splashing. This treatment is, again, limited to the case of single droplets impinging on a smooth, flat, and rigid surface.

Nomenclature

ADH	adhesive force
C_d	coefficient of drag
g	acceleration
k	wave number
L	ligament thickness
Oh	Ohnesorge number
Re	Reynolds number
S	surface area of lamella edge
t	time
u	velocity
V	volume of ligament

Greek

λ	wavelength
v	kinematic viscosity
σ	surface tension

Subscripts

g	gas
l	liquid
lam	lamella
mom	momentum
o	impact

8.1 A Closer Look at the Leading Edge of Spreading

It has already been proven by Xu [1] and in Chapters 6 and 7 that the ambient air pressure has a significant effect on splashing. This has been explained in Chapter 6 and by Jepsen [2] as a compressive effect in which the gas below the droplet is compressed and forced outward, while causing a shearing force on the droplet surface. A closer look at the splashing dynamics, however, reveals that splashing is initiated and continues long after droplet impact. Splashing is more likely initiated post-impact, at the leading edge of the spreading lamella. Therefore, a closer look at this location is warranted. Splashing requires some vertical momentum in order for satellite droplets to separate from the surface and the bulk droplet. With this as a premise, a requirement for splashing is that the lamella lifts off of the impinged surface. Referring to Figure 8.1, a momentum balance may be performed at the lamella edge:

$$\rho_l V \frac{du_{lam}}{dt} = \frac{1}{2}\rho_g u_g^2 C_d S - \sigma L - ADH \tag{8.1}$$

where *ADH* is some adhesion or chemical affinity that the liquid has on the impinged surface. The term on the left is the change in vertical momentum of the lamella with time. This is equated to the momentum imparted on the lamella by the gas motion minus the opposing effect of surface tension and adhesion. We may assume that as the lamella spreads radially outward, the surrounding gas is displaced upward, creating a vertical velocity, $u_g \sim u_s \approx \sqrt{Du_o / 4t}$. The thickness of the lamella will scale with the boundary layer

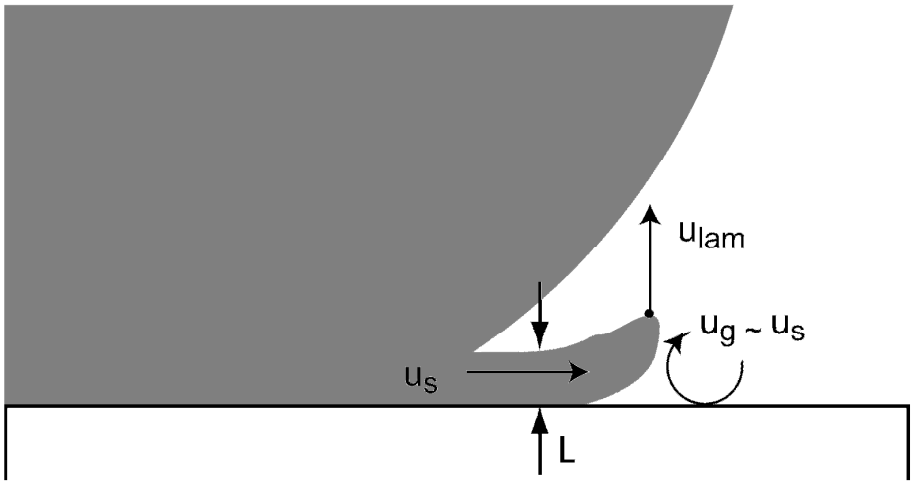

Figure 8.1: A schematic of lamella lift and the relevant velocities.

thickness so $L \sim \sqrt{\upsilon_l t}$. The surface area, *S*, is determined by the *L* and the perimeter of the lamella:

$$P = 2\pi r(t) \approx 2\pi \int \sqrt{\frac{Du_o}{4t}} dt \approx 2\pi \sqrt{Du_o t} \tag{8.2}$$

A requirement for lamella lift is that its vertical momentum be greater than zero. Therefore, we may set the LHS of Equation 8.1 to zero to determine the threshold conditions for lift. Substituting and rearranging terms, we have:

$$\frac{\pi}{4} \rho_g (Du_o)^{3/2} C_d \sqrt{\upsilon} = \sigma \sqrt{\upsilon_l t} + ADH \tag{8.3}$$

Lift is most likely to occur at the earliest possible time after impact since the air velocity will decrease significantly with time. This is the moment when a distinct lamella layer

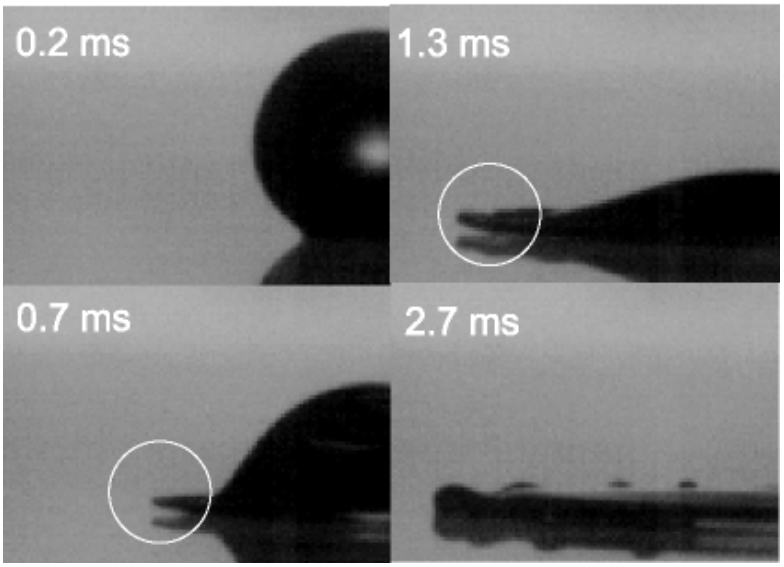

Figure 8.2: Lamella lift without splashing for 85% glycerol solution at 4.5 atm. Elapsed times from impact are provided.

extends beyond the outer boundary of the bulk droplet. According to Bird et al. [3], this time is $t_c \sim \upsilon_l / u_o^2$. Substituting and simplifying again:

$$\rho_g C_d \, Re^{3/2} \, \upsilon_l^2 = \frac{\rho_l \, Re \, \upsilon_l^2}{We} + ADH \tag{8.4}$$

Because of the very low *Re* existing with respect to the lamella thickness, C_d may be computed using:

$$C_d = \frac{1.328}{Re^{1/2}} \approx \frac{1.328\sqrt{\upsilon_g}}{\left(\frac{Du_o\upsilon_l}{4}\right)^{1/4}} \tag{8.5}$$

which is for the average drag coefficient for laminar flow over a flat plate [4]. Interestingly, if we ignore *ADH*, Equation 4 simplifies to a form very similar to Equation 7.6:

$$\left(\frac{\rho_g \mu_g}{\rho_l \mu_l}\right)^{1/4} Oh\, Re^{9/8} = 1 \sim \frac{1}{\mu_l^{3/8}} \tag{8.6}$$

This analytically derived expression shows that splashing should always decrease with increasing liquid viscosity, following intuition. As will be shown later, the regime in the high *Re* range where viscosity appears to promote splashing is actually due to the *ADH* term.

8.2 Predicting Lamella Fingering with Rayleigh-Taylor Instability

Lamella lift is a necessary, though insufficient condition for splashing since it provides no provision for satellite droplet formation. Figure 8.2 demonstrates this with a 15% water-glycerol droplet where lamella lift occurs without splashing. What follows is a theoretical framework describing the physics of a second requirement for splash formation.

Until this point, no mention has been made of the obvious wave-like undulations of the lamella edge during spreading. Analogous to the formation of a spray from an unbroken liquid jet, droplets form from these undulations as they elongate into ligaments, or "fingers", and eventually break by capillary pinching. But the mechanism by which these

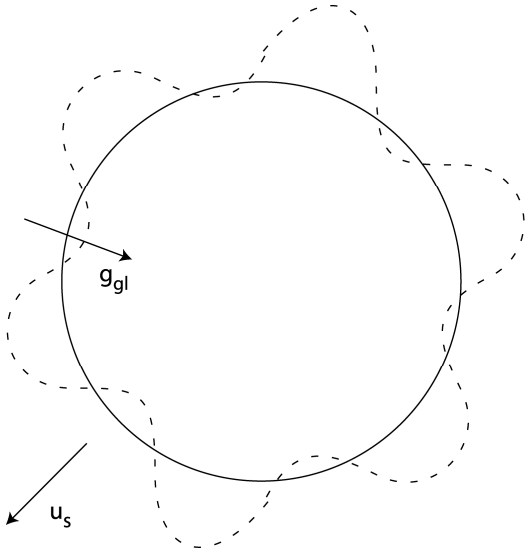

Figure 8.3: Top view of droplet impact with undulations formed under the strong acceleration field.

ligaments initially form has been under debate for the past few years. Here I will use the Rayleigh-Taylor (RT) instability theory as I believe it is the most plausible for to explain the undulations forming along the leading edge of the lamella. The effect of the surrounding gas pressure on splashing has been accounted for in the lamella lift requirement of the previous section. RT instability arises at the interface between two fluids of different densities where there is an acceleration from the lighter to heavier fluid, as depicted in Figure 8.3. If we assume irrotational, inviscid 2-D flow, we may use the following dispersion relation describing the interfacial wave dynamics [5]:

$$n^2 = \frac{\rho_l - \rho_g}{\rho_l + \rho_g} g_{gl} k - \frac{\sigma k^3}{\rho_l + \rho_g} \tag{8.7}$$

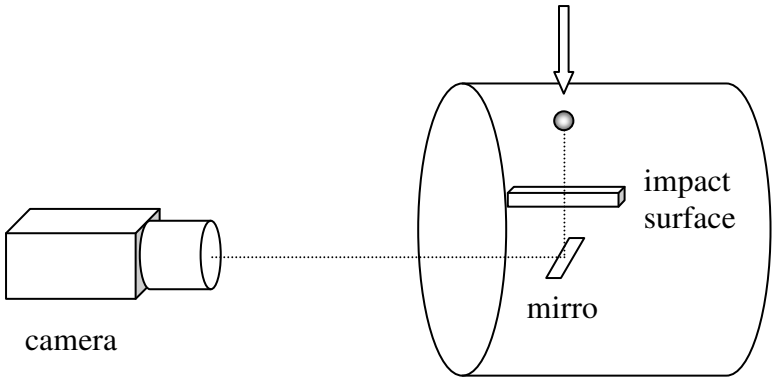

a

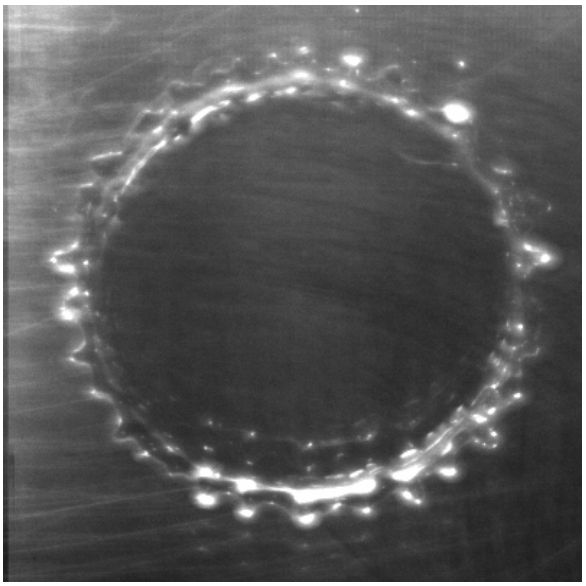

b

Figure 8.4: (**a**) The experimental apparatus of Chapters 6 and 7 modified to image fingering from below and (**b**) a typical image of fingering for a water droplet.

Taking $\partial n / \partial k = 0$ and inverting, we get an expression for the fastest growing wavelength:

$$\lambda = \sqrt{\frac{3\sigma}{g_{gl}\left(\rho_l - \rho_g\right)}} \tag{8.8}$$

This is the wavelength most likely to manifest. The acceleration may be determined by taking the derivative of the now familiar expression for spreading velocity:

$$g_{gl} = 0.5\sqrt{\frac{Du_o}{4}}t^{-1.5} \tag{8.9}$$

According to Equations 8.8 and 8.9, the wavelength and, thus, number of fingers clearly remains a function of time and will theoretically vary over the course of spreading. This has been shown to be the case by Thoroddsen and Sakakibara [6]. By retrofitting the pressure chamber with a mirror to obtain an axisymmetric view of spreading from below the impact surface (Figure 8.4), we may count the number of fingers that form at a given instance in time. Several representative cases are shown in Figure 8.5 and indicate that despite the many assumptions of RT instability, it predicts a similar number of fingers to those experimentally observed. For the case of water and FC-72, the theoretical prediction is very close to the experimental data. With the higher viscosity 50% glycerol solution, however, the predicted value deviates somewhat. This may be due to the different spreading dynamics of higher viscosity fluids since the acceleration from gas to liquid is higher. If we shift the experimental measurement to later times, it appears to agree with the asymptotic value of RT theory.

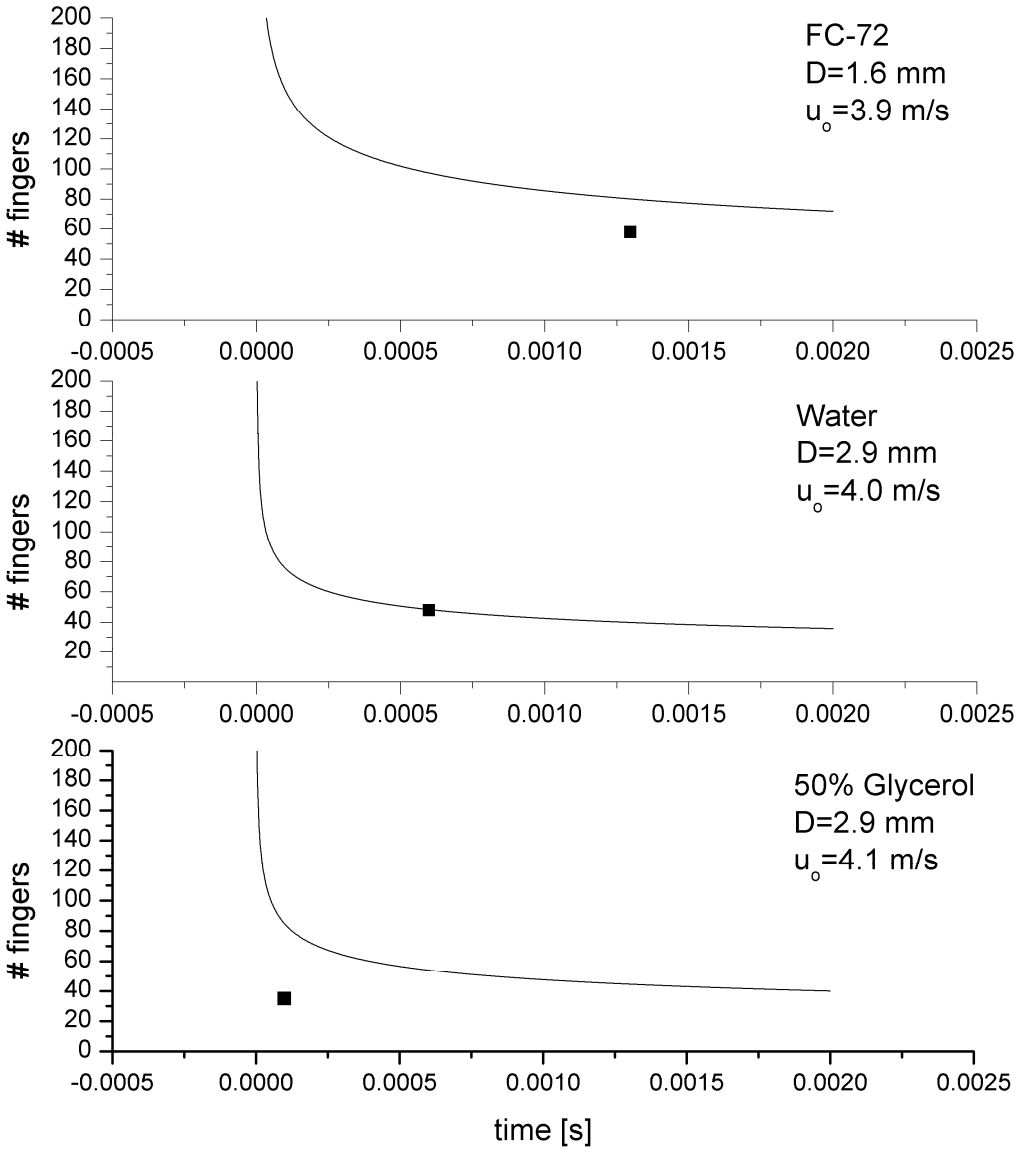

Figure 8.5: Comparison of RT instability predictions of the number of fingers at the lamella edge to experimentally determined values at fixed times.

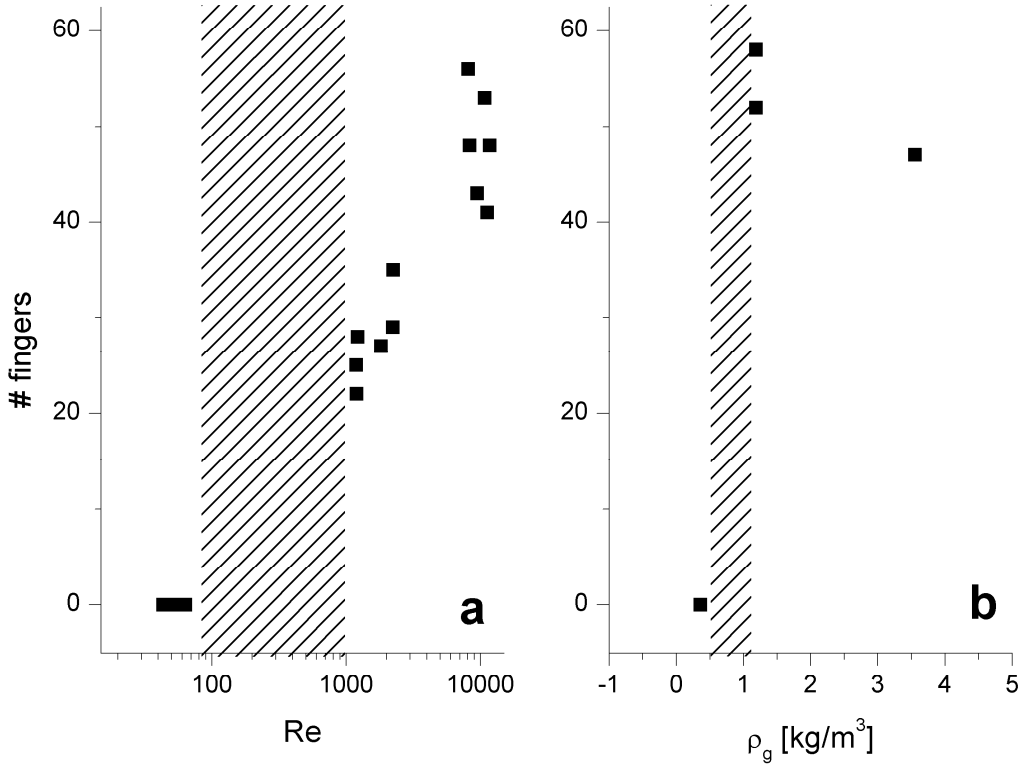

Figure 8.6: Experimentally determined number of fingers as a function of (**a**) *Re* using water, 50% glycerol and 90% glycerol; and (**b**) ρ_g using FC-72. Shaded areas are the expected transition regions where fingers abruptly appear.

It is also interesting to note that at low viscosity or low gas pressure, an abrupt threshold is observed experimentally in which no fingers will form (Figure 8.6). This is not predicted by Equation 8.8 since it is not a function of viscosity and is only weakly a function of gas density. The reasons for this are currently unknown and beyond the scope of my study.

8.3 Ligament Dynamics and Satellite Droplet Formation

Despite the aforementioned limitations, RT theory appears to be an acceptable expression to determine ligament thickness under most cases, so we now move to the dynamics of elongation and breakup. We first look at a momentum balance within the ligament to ensure that breakup can physically occur. The volume of a ligament as a function of time is:

$$\frac{\pi}{4}\lambda^2 \int_t \left(\frac{Du_o}{4t}\right)^{0.5} dt = \frac{\pi}{4}\lambda^2 \left(Du_o t\right)^{0.5} \tag{8.10}$$

The momentum of a ligament may then be equated to surface tension to determine the time window of breakup:

$$\frac{1}{2}\rho_l \left(\frac{\pi}{4}\lambda^2 \left(Du_o t\right)^{0.5}\right)\left(\frac{1}{4}\frac{\left(Du_o\right)^{0.5}}{t^{1.5}}\right) = \sigma\frac{\pi}{4}\lambda^2 \tag{8.11a}$$

$$t_{mom} = \frac{\rho_l Du_o \lambda}{32\sigma} \tag{8.11b}$$

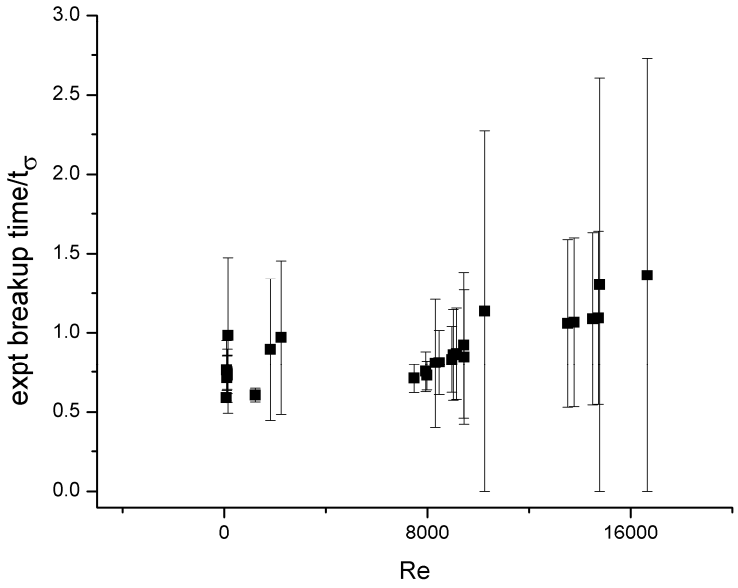

Figure 8.7: Ratio of experimental breakup times to ligament capillary times, t_σ as a function of *Re*.

This time represents the time from impact in which the momentum of the ligament is sufficient to break surface tension. Using typical droplet properties of water, we find that t_{mom} is ~2 ms, on par with the total spreading time. This is, therefore, not a likely limiting factor to ligament breakup. Another timescale of interest is the capillary or emptying time of a ligament, as determined by Marmottant and Villermaux in their studies of spray formation [7]:

$$t_\sigma = \sqrt{\frac{\rho_l \lambda^3}{\sigma}} \tag{8.12}$$

This is a value representing the time required for the liquid to flow through the ligament as it elongates. If ligament dynamics occur on a shorter timescale, breakage will occur.

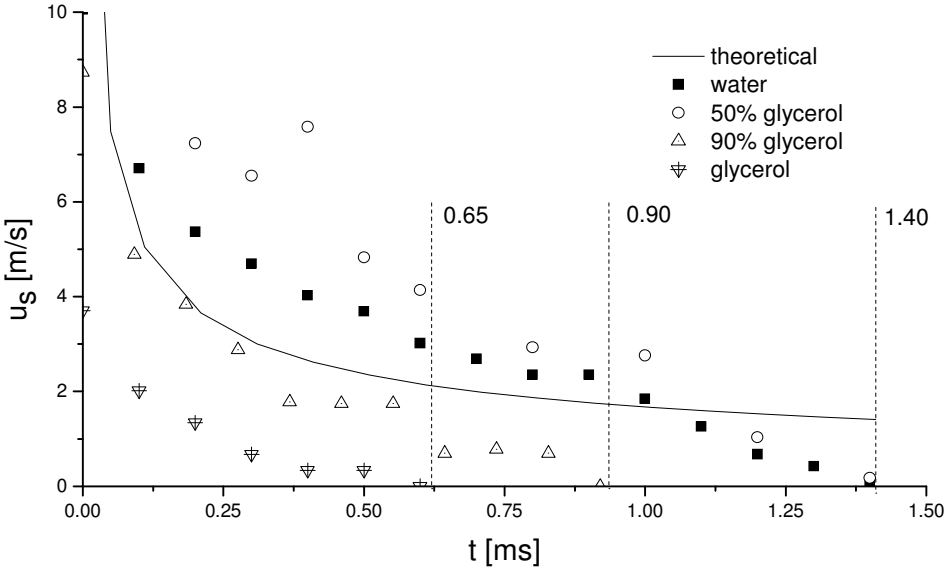

Figure 8.8: Changes in spreading dynamics with increasingly viscous liquids. For all cases, $D \approx 2.9$ mm and $u_s \approx 4$ m/s. Dashed lines indicate times of spreading cessation.

To test if this is the limiting time to ligament breakage, we take the ratio of t_σ to the experimentally determined time of breakup as a function of ligament *Re*, shown in Figure 8.7. The large error bars represent the uncertainty in measured time of breakup due to the video frame rate. At early times, this error is comparable to the actual time of breakup. Despite the significant scatter, the ratios generally are near 1, an indication that t_σ is likely the major limiting time for breakup.

In Chapter 7 I discussed the notion of a "time window" of opportunity for splashing in highly viscous droplets. In light of the analytical developments just presented, this time window is most likely either the spreading time of the droplet or t_{mom}. For viscous droplets, spreading time may be reduced significantly as shown in Figure 8.8. The

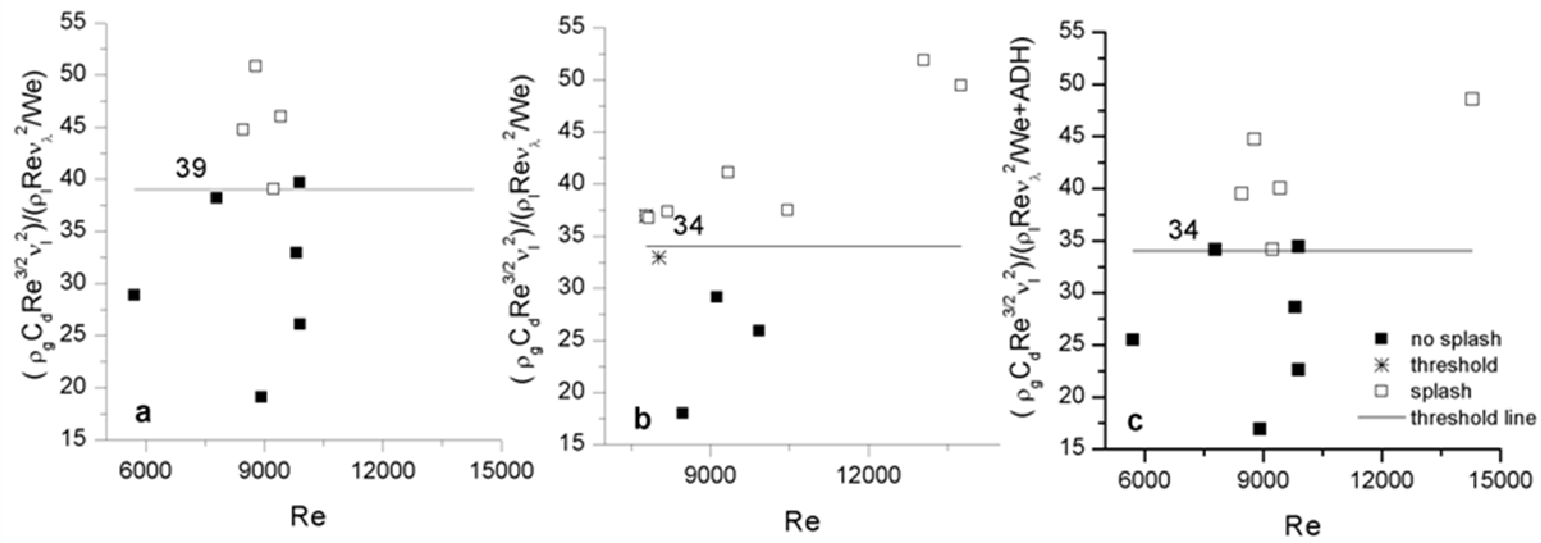

Figure 8.9: Threshold requirements for lamella lift for water droplets impinging onto a (**a**) hydrophilic and (**b**) hydrophobilc surface. The addition of the ADH term (**c**) lowers the hydrophilic threshold to that of the hydrophobic surface.

ligament breakup time, t_σ, must be smaller than the spreading time or t_{mom} for breakup to occur. If not, there is insufficient time for the dynamics of ligament elongation to take place and breakup cannot happen.

8.4 Droplet-Surface Affinity and Implications on Splashing

We now revisit the *ADH* term of Equation 8.1 and discuss its implications on splashing. The absolute value of this quantity is difficult to determine experimentally, but droplet experiments were repeated for water droplets impacting on Plexiglas surfaces chemically treated to be hydrophilic and hydrophobic using a commercially available products (Rain-X, Blue Coral-Slick 50, Ltd., Cleveland, OH). For the hydrophilic case, the water droplets completely wetted the surface, while the hydrophobic case produced a contact angle of ~130˚ (untreated Plexiglas produces a contact angle of ~150˚). Theoretically, the *ADH* term should be larger for the hydrophilic case.

As shown in Figure 8.9, this is confirmed by the experimental data. The hydrophilic data requires a higher gas momentum relative to surface tension to induce splashing. The difference in threshold represents a relative quantity for *ADH*, 4 x 10^{-9} N in this case. Using this value to correct the hydrophilic data brings the threshold to the same level as the hydrophobic data. This confirms that *ADH* is a constant, dependent only on the chemical affinity of the liquid to the impact surface, and is not a function of kinematic properties.

A major implication of recognizing the *ADH* term is shown in Figure 8.10 with the lift threshold as a function of viscosity. It reveals that there is a non-obvious viscosity corresponding to the minimum energy to induce lift. This minimum point changes with *ADH*. A very similar curve was measured experimentally by Xu [1] by varying the viscosity of the droplet, drawing attention to the seemingly paradoxical effect of viscosity in which it can both promote and inhibit splashing. As the quantity of the surface tension term becomes comparable to the *ADH* term, a reversal of the role of viscosity can be seen.

8.5 Conclusions

Analytical advancements were made in explaining and predicting the onset of splashing of single droplets impinging on a flat smooth surface. Two separate requirements for splashing were revealed: lamella lift, and ligament elongation and breakup. Both must be satisfied for splashing to occur. The dependence of splashing on gas density was incorporated in the lamella lift requirement. RT instability theory was found to accurately predict finger formation except for the cases of high liquid viscosity or low gas density, where instabilities appear to cease abruptly. For highly viscous droplets, the "time window" of opportunity of splashing is reduced as the spreading time of the lamella is reduced. The capillary time of the ligament is the time required for it to break up into droplets. If the spreading time is shorter, then the impact dynamics end before the ligament has time to fully elongate and break. The inclusion of an adhesion term in the lift threshold may explain the paradoxical effect of viscosity on splashing.

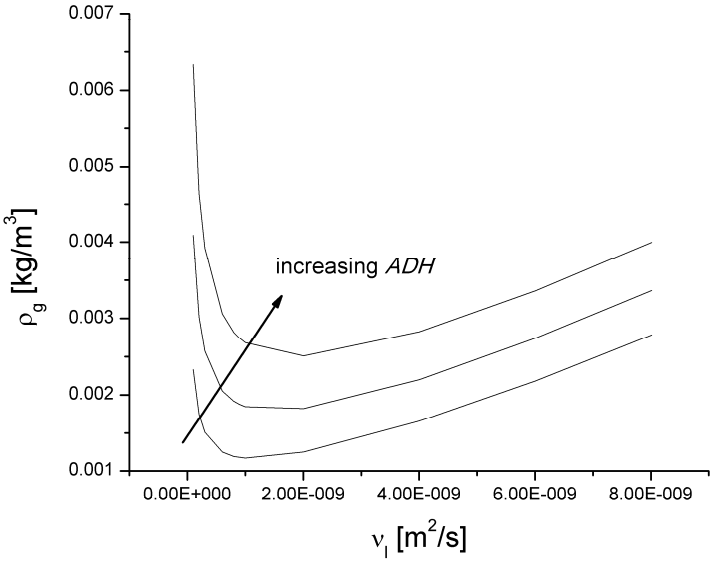

a

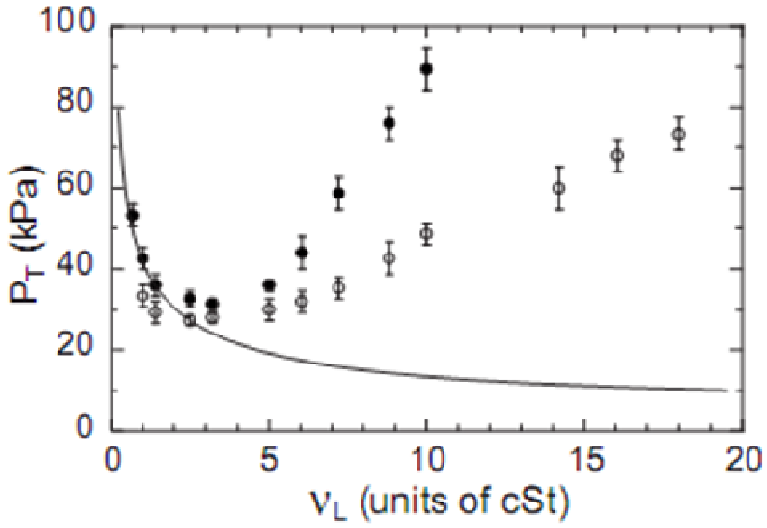

b

Figure 8.10: (**a**) A parametric analysis of the effect of ν_l on the threshold ρ_g required for lamella lift using a water droplet with D = 3.6 mm and u_s = 2.8 m/s. (**b**) A figure of the threshold pressure required for splashing (solid points) and fingering (open points) as a function of ν_l [1]. The solid line is the threshold given by Equation 7.3.

References

1. Xu, L., *Liquid drop splashing on smooth, rough, and textured surfaces.* Physical Review E, 2007. **75**(5): p. 056316-1-8.

2. Jepsen, R.A., S.S. Yoon, and B. Demosthenous, *Effects of air on splashing during a large droplet impact: Experimental and numerical investigations.* Atomization and Sprays, 2006. **16**(8): p. 981-996.

3. Bird, J.C., S.S.H. Tsai, and H.A. Stone, *Inclined to splash: triggering and inhibiting a splash with tangential velocity.* New Journal of Physics, 2009. **11**.

4. Çengel, Y.A. and R.H. Turner, *Fundamentals of thermal-fluid sciences*. McGraw-Hill series in mechanical engineering. 2001, Boston: McGraw-Hill.

5. Acheson, D.J., *Elementary fluid dynamics*. Oxford applied mathematics and computing science series. 1990, Oxford; New York: Clarendon Press ; Oxford University Press.

6. Thoroddsen, S.T. and J. Sakakibara, *Evolution of the fingering pattern of an impacting drop.* Physics of Fluids, 1998. **10**(6): p. 1359-1374.

7. Marmottant, P.H. and E. Villermaux, *On spray formation.* Journal of Fluid Mechanics, 2004. **498**: p. 73-111.

CHAPTER 9: Conclusions and Future Work

This dissertation is primarily an experimental work on the dynamics of flashing sprays and single droplet impacts. Chapters 2-5 detail my earlier work on flashing spray atomization mechanisms. It was found that flashing sprays may have highly time dependent breakup mechanisms, depending on the internal nozzle flow regimes. Numerical modeling showed that phase change is the dominant mechanism controlling flow characteristics. A large velocity differential develops between the liquid and vaporized gas phases so shearing between the phases was also found to be a major mechanism of atomization and explained the measured droplet accelerations away from the nozzle exit in the external spray. So in many ways, flashing or thermodynamic sprays resemble mechanically atomized sprays. This may have important implications for future work as we may borrow from theory already developed for more common sprays.

This work, though revealing new insights into flashing atomization, has thus far been mostly qualitative. I unfortunately did not have the time to pursue a more in-depth analysis of the atomization mechanisms to improve nozzle designs and explore new applications. However, the application of dynamic cooling of human skin was explored and revealed that despite large dynamics in spray characteristics, cooling appears to be dictated more by the substrate thermal properties.

The second part of the dissertation examined a very specific case of droplet impingement dynamics—that of single droplets impinging on flat, smooth, dry surfaces. Some significant advancement was made on this topic. The effects of gas pressure on splashing

were confirmed for super-atmospheric cases. Significant limitations on existing theory and empirical correlations were revealed and motivated further work. A new analytical framework of the dynamics was then developed and identified three distinct stages of splashing: lamella lift, finger formation, and finger elongation and breakup. All three stages must occur in order for splashing to take place. The splash dependence on gas pressure was incorporated into a momentum balance on lamella lift while RT instability was shown to fairly accurately predict finger formation. The seemingly paradoxical effect of liquid viscosity to both promote and suppress splashing was explained through the addition of a chemical adhesion term between the droplet and impinged surface. This term was measured and confirmed to exist using impact surfaces treated to be either hydrophilic or hydrophobic. Time limitations on finger elongation and breakup were proposed to explain why high viscosity liquids get progressively more difficult to splash.

I had planned to do significantly more work on these issues, but due to time constraints, I was not able to complete them. So for future work, the flash atomization mechanisms should be reanalyzed to develop more quantitative relations to predict atomization characteristics. The observed effect of nozzle orientation with respect to gravity on the internal flow regimes and atomization also needs explanation. The ability to control average droplet size and size distribution is a significant goal that would allow flashing to be used in applications such as flame spray pyrolysis of particulates. Reducing droplet sizes to submicron scale while narrowing the size distribution may greatly increase throughput and lower the cost of manufacture of many types of particulates used in applications such as color dying and chemical catalysis. For droplet impacts, the

evaluation of time limitations on finger breakup needs to be further explored. Most notably, the momentum time, t_{mom}, was not fully evaluated and may be a major limiting factor to splashing. Also, a more quantitative measurement of chemical adhesion may be possible using more advanced surfaces engineered to have specific surface properties. The influence of this effect is also of great interest in heat transfer applications, as it may affect wetting and boiling characteristics.

Appendix: My Publications

Journal

1. **Vu, H.** and G. Aguilar, Lamella dynamics during droplet corona splashing. (in preparation).

2. **Vu, H**., H. Jung, and G. Aguilar, Breakup mechanisms of flashing water jets. (in preparation).

3. **Vu, H**., D. Banks, S.S. Yoon, R. Jepsen, A.L. Brown, and G. Aguilar, The Effects of Liquid Viscosity on Droplet Corona Splashing. to be submitted to Experiments in Fluids.

4. Liu, J., **H. Vu**, S.S. Yoon, R. Jepsen, and G. Aguilar, Splashing phenomena during liquid droplet impact. Atomization and Sprays, 2010. **(in press)**.

5. Franco, W., **H. Vu**, W. Jia, J.S. Nelson, and G. Aguilar, Fluid and thermal dynamics of cryogen sprays impinging on a human tissue phantom. Journal of Biomechanical Engineering-Transactions of the Asme, 2008. **130**(5).

6. **Vu, H**., O. García-Valladares, and G. Aguilar, Vapor/Liquid Phase Interaction in Flare Flashing Sprays Used in Dermatologic Cooling. International Journal of Heat and Mass Transfer, 2008. **51**: p. 5721-5731.

7. Aguilar, G., **H. Vu**, and J.S. Nelson, Influence of angle between the nozzle and skin surface on the heat flux and overall heat extraction during cryogen spray cooling. Physics in Medicine and Biology, 2004. **49**(10): p. N147-N153.

8. **Vu, H**., G. Aguilar, and J.S. Nelson, Passive mass deposition control of cryogen sprays through the use of wire meshes. Lasers in Surgery and Medicine, 2004. **34**(4): p. 329-334.

Conference Proceedings

1. Jepsen, R., A.L. Brown, G. Aguilar, and **H. Vu**. Drop fingering on oblique impact: part 1—experimental data. in 11th International Congress on Liquid Atomization and Spray Systems. 2009. Vail, CO.

2. **Vu, H**. and G. Aguilar. High-speed internal nozzle flow visualization of flashing jets. in 11th International Congress on Liquid Atomization and Spray Systems. 2009. Vail, CO.

3. **Vu, H**., G. Aguilar, and R. Jepsen. Single droplet heat transfer through shallow liquid pools. in 11th International Congress on Liquid Atomization and Spray Systems. 2009. Vail, CO.

4. **Vu, H**., H. Jung, and G. Aguilar. Influence of a coaxial gas flow on a flashing liquid jet: implications for flame spray synthesis of nanoparticles. in 21st Annual Conference on Liquid Atomization and Spray Systems. 2008. Orlando, FL.

5. **Vu, H**., O. García-Valladares, and G. Aguilar. Insights Into Flashing Spray Characteristics Using a Capillary Tube Expansion Model. in 20th Annual ILASS-Americas Conference. 2007. Chicago, IL.

6. Franco, W., **H. Vu**, W.C. Jia, J.S. Nelson, and G. Aguilar. Spray cooling dynamics of cryogen sprays impinging on a human skin model. in ASME-JSME Thermal Engineering Summer Heat Transfer Conference. 2007. Vancouver, British Columbia, Canada.

7. Franco, W., **H. Vu**, W.C. Jia, J.S. Nelson, and G. Aguilar. Fluid and heat transfer dynamics of cryogen sprays cooling a human skin model. in XI Congreso Latinoamericano de Transferencia de Calor y Materia. 2006. Mexico City, Mexico.

8. Liu, J., W.C. Jia, **H. Vu**, and G. Aguilar. Heat transfer of single cryogen droplet onto epoxy skin phantom. in 10th International Congress on Liquid Atomization and Spray Systems. 2006. Kyoto, Japan.

9. **Vu, H**., W. Franco, W.C. Jia, and G. Aguilar. Hypobaric pressure effects of R134a cooling sprays for laser dermatology. in 10th International Congress on Liquid Atomization and Spray Systems. 2006. Kyoto, Japan.

10. Liu, J., W.C. Jia, **H. Vu**, and G. Aguilar. Heat transfer between single cryogen droplet and epoxy skin phantom. in 19th Annual Conference on Liquid Atomization and Spray Systems. 2006. Toronto, Canada.

11. **Vu, H**., W. Franco, W.C. Jia, and G. Aguilar. Effects of Ambient Pressure on R134a Sprays for Laser Dermatological Applications. in 19th Annual Conference on Liquid Atomization and Spray Systems. 2006. Toronto, Canada.

12. Romero-Mendez, R., K. Chu, **H. Vu**, W. Franco, and G. Aguilar. Confinement of freezing front by laser irradiation during cryosurgery. in ASME Summer Heat Transfer Conference. 2005. San Francisco, CA.

13. Franco, W., **H. Vu**, and G. Aguilar. Effect of micro-meshes on droplet size and velocity distributions of cryogenic sprays. in ASME Summer Heat Transfer Conference. 2005. San Francisco, CA.